EXPERIMENTAL STUDY ON WAVE TRANSFORMATION AND NEARSHORE CIRCULATION ON A VARIABLE BATHYMETRY IN WETLANDS

A Thesis

by

MELANIE KHANH PHUONG TRUONG

Submitted to the Office of Graduate Studies of
Texas A&M University
in partial fulfillment of the requirements for the degree of

MASTER OF SCIENCE

August 2011

Major Subject: Ocean Engineering

EXPERIMENTAL STUDY ON WAVE TRANSFORMATION AND NEARSHORE CIRCULATION ON A VARIABLE BATHYMETRY IN WETLANDS

A Thesis

by

MELANIE KHANH PHUONG TRUONG

Submitted to the Office of Graduate Studies of
Texas A&M University
in partial fulfillment of the requirements for the degree of

MASTER OF SCIENCE

Approved by:

Chair of Committee,	Scott A. Socolofsky
Committee Members,	Jennifer L. Irish
	Achim Stoessel
Head of Department,	John Niedzwecki

August 2011

Major Subject: Ocean Engineering

ABSTRACT

Experimental Study on Wave Transformation and Nearshore Circulation on a Variable Bathymetry in Wetlands. (August 2011)

Melanie Khanh Phuong Truong, B.S., Lycee Chaptal, Paris, France

Chair of Advisory Committee: Dr. Scott A. Socolofsky

Hurricanes are one of the primary threats to the Texas coastal environment and economy. They generate large wave and storm surges that have caused much damage on the Texas coast in the past. Understanding both the hydrodynamic processes that damage coastal habitats and hurricane hazard and risk are critical to preserve coastal vegetation and quantify its benefits to coastal storm protection. The goal of this project is to quantify the impact of wave attenuation and wave refraction as well as the development of coherent structures in marsh fringes and the formation of a rip current system over wetlands on storm protection. The 3D Shallow Water Wave Basin at Texas A&M University hosted a series of large-scale experiments considering an idealized wetland model to pursue this goal.

Study of the marsh geometry of the Texas coast was done in order to scale the experiments to the size of the Haynes Laboratory 3D-Water Wave Basin using a Froude and a Reynolds scalings. Particularly, averaged size and idealized shape of marsh segments in the area of Dalehite Cove in Galveston Bay were considered. Three sets of different wave conditions and water levels were tested to approximate different intensities of storm surge. Identical tests with both vegetated and non-vegetated marshes were run to compare the influence of the vegetation in storm conditions, and three different spacings between marsh segments were tested.

In the basin, normally incident regular waves were generated at three water depths to take into account one near-emergent case and two submergent cases of the vegetation fields. Water surface elevation was measured to analyze wave attenuation as a function of vegetation spatial coverage using wave gauges. The creation of rip current in the marsh channels was measured by 3D point measurements using Acoustic Doppler Velocimeters (ADV) to analyze the wave induced circulation structures. Data analysis allows the determination of the impact of discontinuous marsh segments on wave attenuation and wave refraction. Coherent structures such as rip current and the circulation pattern were analyzed to study the change in the flow field during passage of the waves.

The experimental measurements were able to describe the wave transformations over the marsh segments. The influence of coastal wetlands was identified to affect the hydrodynamic process and reduce the total wave energy which is dissipated and redistributed by vegetation. The presence of the mounds induced an important decrease in the wave height, in addition to the damping of the waves by the vegetation stems. The variation in spatial coverage of the wetland model has been shown to highly affect the flow dynamics by generating offshore directed flow in the channel and onshore directed flow on the marsh mounds. This experimental approach provides a further understanding of flow dynamics by waves and surge in wetlands, at a large scale.

To my parents, Amanda, Huy and Brandon Flowers

ACKNOWLEDGMENTS

I would like to thank my committee chair, Dr.Scott Socolofsky, for giving me the opportunity to work as a graduate research assistant in his group and on such a large scale project. Lots of energy and brainstorming was necessary not only to design these experiments but also to achieve the data analysis. Great and constructive ideas always came up to find solutions to problems. I would also like to thank my committee members: Dr. Jennifer Irish for her creative contributions to this research and for providing me with the opportunity to work on this project; Dr. Achim Stoessel for his guidance and comments throughout the course of my graduate career. I would like to thank Mr.John Reed and Dr.Po-H. Yeh for their technical guidance and the sharing of their experience in the Haynes Coastal Engineering Laboratory. Special thanks are dedicated to David Dailey, and Kristie Drawe, student workers in the research group, and also Paul Ramsey, Christopher Ryan and Eric Sonne, student workers at the Haynes Laboratory, for their great help and input during the laboratory experiments. Finally I would like to express my gratitude to my officemates and friends in Ocean Engineering.

TABLE OF CONTENTS

CHAPTER Page

CHAPTER Page

LIST OF TABLES

TABLE Page

TABLE Page

LIST OF FIGURES

CHAPTER I

INTRODUCTION

A. Motivations and Objectives

On the Texas coast, wetlands are defined as the areas where the water meets the land (Texas Parks and Wildlife Department, 2003). They serve as a transition between dry land areas and deeper water areas. They perform various functions as part of the ecosystem, for example, providing a habitat and feeding ground for fish and other marine organisms in addition to maintaining water quality. The specific morphology of these ecosystems, in most cases, is composed of natural marshes, but human work has been done in the past decades in order to restore and preserve these rich habitats through marsh restoration and creation projects.

In 2009, the National Oceanic and Atmospheric Administration had funded 50 coastal habitat restoration project including one for the state of Texas, to help restore inter tidal wetlands in the West Galveston Bay (HDR 2009). The restoration areas was constructed through placement of sandy material dredged from nearby areas in West Bay. The dredged material was discharged as clusters of mounds that supported marsh complex consisting of inter tidal areas and protected shallow open water. A network of larger channels, bayous, and ponds will separate the mound clusters.

Wetland mounds, indeed, affect the wave hydrodynamic process occurring in these wetlands because of the interaction between the spatial distribution of marsh segments and the flow acceleration around them. The combination of the geometrical properties of the marsh as well as vegetation morphology and the flow field is likely to generate large scale coherent structures. Indeed, the potential formation of flow

---

This thesis follows the style of the *Journal of Hydraulic Engineering.*

structures, such as rip currents, are able to drive the in-flow back offshore preventing an excess of water flux inland that can generate natural disaster such as flood. Hence, wetlands have the potential to play an important role in storm damage reduction on shore. At the current stage of this study, coastal vegetation is known to dissipate wave energy and attenuate the input waves but also to generate more turbulence within the vegetation field as documented in several experimental studies (Nepf 2004, Folkard 2005, White & Nepf 2008).

By definition, a rip current is a strong and narrow current of water seaward-directed from the shore. Its formation is triggered by waves breaking in the breaker zone as they shoal on the nearshore sloped bottom, such as sandbars for example, and increase in wave height. This change in magnitude is balanced by a decrease in the mean water level with respect to the still-water elevation of the sea, a phenomenon known as set-down. The breaking of the waves is accompanied by a reduction in wave height giving rise to an elevation in the mean water surface known as setup. As the waves break, a pressure gradient is created due to the higher mean water level and drives convergent longshore currents called the “feeders”. The narrow channel in between the sandbars, known as the “neck”, forces the flow to jet out offshore. Figure 1 displays the general structures of a rip current.

Multiple parameters have to be accounted for to understand the complex interactions of waves and current in a wetland marsh such as plant morphology, density, flow depth, and speed. However, an understanding of the influence of the spatial distribution of segmented vegetated marshes on wave hydrodynamics is lacking. The goal of this M.S. thesis is to quantify the impact of constructed marshes on wave attenuation and wave refraction as well as the development of coherent structures in marshes fringe in a scaled model of segmented wetland. An experimental study has been conducted to simulate the wetland hydrodynamics in a laboratory as the

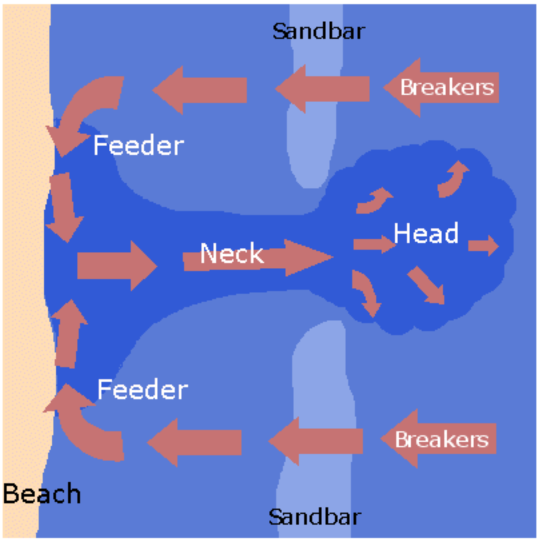

Fig. 1. Rip current (from http://www.ripcurrents.noaa.gov/).

environment is more easily controlled.

Study of the marsh geometry on the Texas coast has been done in order to scale the experiment to the size of the Haynes Coastal Engineering Laboratory 3D-Shallow Water Wave basin using the following scaling parameters: a Froude scaling for dynamic similarity of the flow in the prototype; a Reynolds scaling and a Population density scaling (Nepf 2004) to recreate the drag force produced by the vegetation on the flow field. Details of the design method is provided in Chapter III, Section B. The geometrical similarity of the model and the full scale structures was respected to obtain the same wetland shape in the model and in the prototype. More particularly, averaged size and idealized shape of marsh segments in the area of Dalehite Cove in the Galveston Bay are considered (HDR 2009) (Figure 2). Three sets of different wave conditions and water levels were tested to acknowledge different intensities of storm

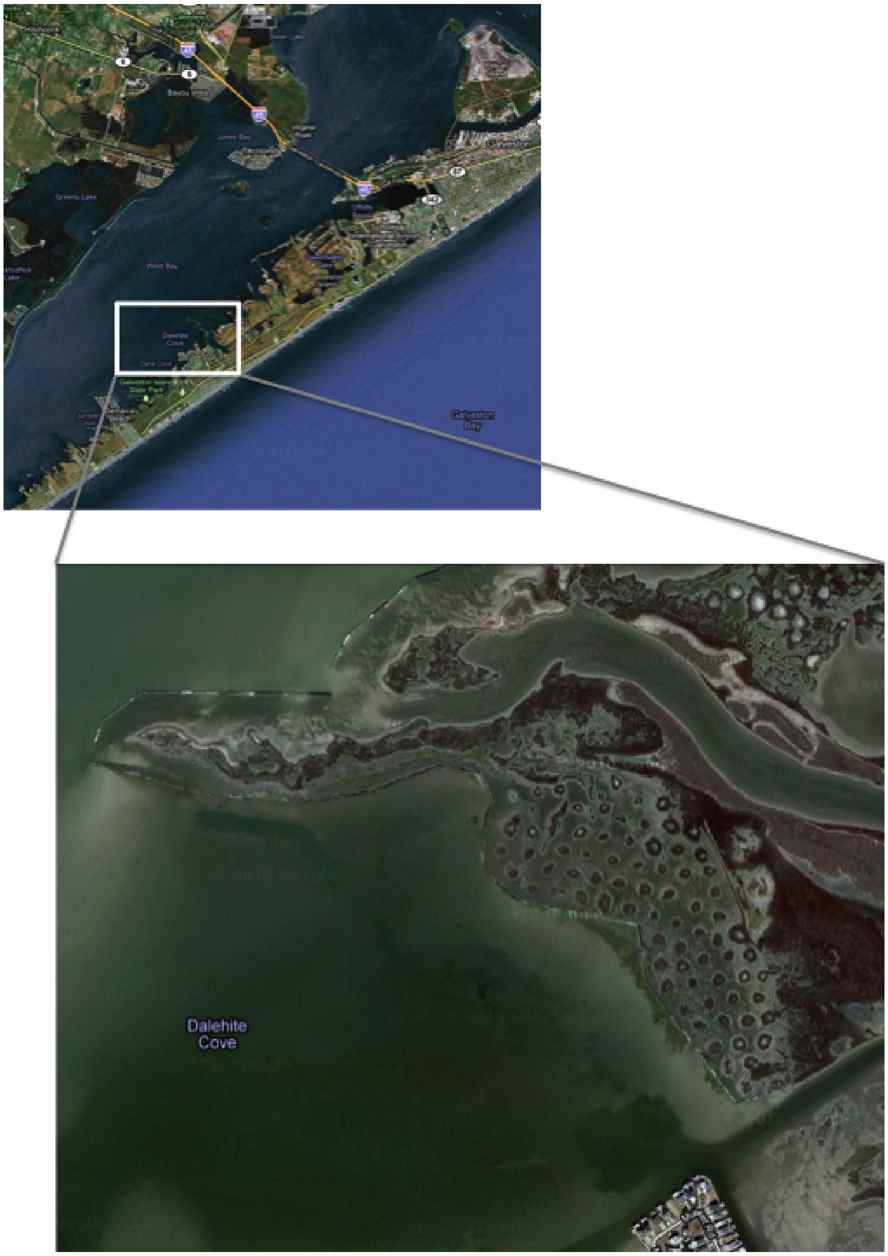

Fig. 2. Dalehite Cove, Galveston Bay, TX (retrieved on May 23rd, 2011 from http://maps.google.com/).

surge. Identical tests with a non-vegetated wetland and a vegetated wetland were run to compare the influence of the vegetation in storm conditions and three different spacings between marsh segments were tested for spatial variability of the wetlands. In the basin, normally incident regular waves were generated in three water depths to take into account one emergent case and two submergent cases of the vegetation stems. Water surface elevations were measured to analyze the wave attenuation as a function of vegetation spatial coverage using wave gauges. The creation of rip currents and the possible development of eddies were measured by 3D point measurements using Acoustic Doppler Velocimeters (ADV) to analyze the wave induced circulation structures at marsh fringes as a function of plant spatial coverage. A wide range of sampling locations were needed to obtain a good resolution and a widespread view of the general fluid circulation. Four main sampling locations were defined and are represented in Figure 3. Data analysis helps in determining the impact of discontinuous marsh segments on wave attenuation and wave refraction. Turbulence spacial variability and circulation patterns created were analyzed to study the change in the flow field at the passage of the waves.

B. Thesis Content

Flow structure in wetland-type bathymetry has the potential to vary with respect to marsh segment geometry, plant morphology, water depth and flow speed. These wetland characteristics are commonly quantified through the drag force they produced on the flow field. These complex interactions in a wave-forcing flow can significantly alter the flow pattern. The scope of the present study focuses on the experimental setup, the data acquisition, the wave transformation, and resulting currents.

For this purpose, 2D contour plots of significant wave height have been generated

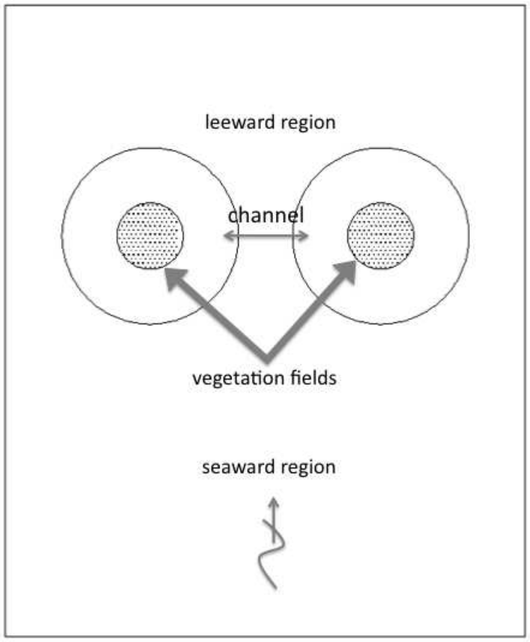

Fig. 3. Sampling locations.

and analyzed to verify and quantify wave attenuation by vegetated marsh segment compared to the unvegetated marsh for three different spacings of the marsh segments to account for the spatial variability. The phase averaging analysis on the wave gauge data provides information on deceleration or acceleration of the waves when propagating in the wetland region. The same analysis has been carried out to compare the phase lag with and without marsh segments using linear wave theory to simulate the wave propagating in the wave basin with no wetland. The terms island, mound and patch will also be used to designate a marsh segment in the rest of this thesis.

Extraction and separation of the mean flow and turbulent fluctuation component have been done using the experimental data measured by the ADVs. The sampling locations of the ADVs were distributed on a regular grid covering the main channel, the seaward region, the leeward region and the vegetated (or non-vegetated) circular patch. A comparison of the turbulent activity in both the vegetation field and the channel has been done computing the turbulent kinetic energy from the ADV data. Horizontal velocity vector (u, v) plots have been generated to detect any 2D-coherent structure formed in the flow field of interest. The variation in intensity of storm surge for the six wave conditions will bring out the effectiveness of the wetlands in re-circulating the flow in the wave basin.

A qualitative knowledge of the nearshore circulation will be provided by a comprehensive dataset of water surface elevation and current under a range of wave conditions. Chapter II identifies and highlights the main publications and investigations that have been done which relate to this thesis and constitutes the literature review. In Chapter III, a complete description of the physical model is provided with the experimental procedures and experimental conditions. In Chapter IV, maps of mean water level, significant wave height, and nearshore circulation are presented and illustrate how the variability of the bathymetry affects current and wave field. Chapter

V relates the conclusions and outlines a scope of future work.

CHAPTER II

BACKGROUND AND LITERATURE REVIEW

A. Introduction

In the past decade, the importance of wetlands and their preservation for environmental purpose has been recognized by the modern society. The natural hydrodynamics of these areas has a significant role in preserving water quality and supporting a great diversity of animal communities living in the soil and on its surface. Human benefits are also important as wetlands contribute to the protection of the coastal habitats against waves and they participate in the stabilization of the seabed. Recreational activities are also found in wetlands: hunting, fishing, and camping are few examples among many more. The use of wetlands have been extended to the protection of hard structures against scouring. To be able to do wetland restoration projects successfully, the understanding of the hydrodynamics of these sites needs to be pursued and completed. Indeed, strong wave motion and large sediment movements constitute a threat against these ecosystems. Being able to increase the lifespan of wetland marshes would necessitate the improvement of the wetland's resistance against dangerous waves. These improvements in wetland properties could then potentially work as a shield for land and human protection against natural disaster such as hurricane storm surge. This resistance can be related to the sediment properties of the dredge material used in restoration work or the addition of metallic structures into the mounds to consolidate it. However, a less artificial method would use the natural geometrical properties spatial distribution of the marsh mounds to control and direct the flow dynamic. A balance would have to be found not to interfere in a dramatic way with the various beneficial functions of wetlands. Three main aspects of wetland hydrodynamics have been identified to be important in the present study:

- wave damping by vegetation
- wave and current hydrodynamics in variable bathymetry
- correlated effects associated with the two previous properties.

The effect of vegetation on water wave fields has been studied in many aspects. Models of wave energy dissipation were developed to account for the presence of vegetation canopy and its influence on wave attenuation and wave diffraction. A measure of wave energy loss by a submerged cluster of rigid cylinders representing the vegetation were derived using the conservation of energy equation and expressed as a function of the drag force on the stems (Dalrymple, Kirby and Hwang 1984). The wave height variation was characterized by a damping factor associated with the geometrical properties of the vegetation field model. Kobayashi et al. (1993) developed another analytical model using the continuity equation and the linearized horizontal and vertical momentum equation adding a term representing the effect of the vegetation, modeled as rigid cylinders. The resulting energy dissipation rate for wave attenuation expressed an exponential decay of the wave height assuming a weak damping. Several other models were developed and improved to be able to comprehend the action of fully vegetated area on wave properties along with experimental laboratory studies illustrating the relevance of the different models. All these models aimed to get a comprehensive modeling of the wave transformation over a vegetation field. Plant elevation with respect to the mean water surface as well as the number of degrees of freedom of the given stems could generate a wide range of variability in the damping of waves. In the particular case of subsurface plants with a strong stiffness in the lower part of the stems (*e.g. Spartina alterniflora*), the common practice has been to consider the plants as rigid vertical cylinders, for which the drag force representation was validated.

Most of these studies strive for the vegetation-wave interaction at the scale of the plant stems supporting the already well admitted theory that the presence of vegetation dissipates wave energy by adding drag force in the water column. The larger scale flow pathways created in vegetated area such as coastal wetlands would have a non negligible effect on the general flow circulation. Therefore spatial variability of marsh segments is expected to have a significant influence on wave-induced circulation, spatial wave patterns and wave transformation. The input wave characteristics undergone in coastal areas such as daily conditions as opposed to storm conditions would influence the generation and the nature of large scale coherent structures in segmented wetlands as well. The marsh-scale, which has to be distinguished from the stem-scale, is characterized by a branching network of channels separated by dense vegetated zones (Nepf 2004). Within the vegetated region, the added drag force induces flow speed reduction compared to the channel flow speed and thus, spatial variation in vegetation density plays an important role in the definition of circulation patterns and the mean flow. The total drag coefficient created by the vegetation field has been defined as the sum of each individual drag induced by each stem, hence the drag force is evaluated as a function of stem density. Evidences of the formation of coherent structures such as vortices at the vegetation-channel interface has been found experimentally and the lateral velocity profile entering a partially vegetated channel showed a decrease in the mean velocity on the vegetated side (White and Nepf 2008). The knowledge of how water moves around vegetated regions is important to determine how geometrical characteristics such as size and shape of a marsh mound will impact wetland restoration work on the Texas Coast.

An overview on vegetation-induced wave attenuation with theoretical, experimental approach and results is presented in Section B using the cylinder-based model to simulate the vegetation field with a glance at a studies including flexible stems. A background on wave and current induced circulation over a vegetation field with an emphasis on experimental results and coherent structures characteristics is described in Section C and Section D respectively, followed by a summary of the literature review and how it relates to the objectives of this study.

B. Overview on Wave Attenuation by Vegetation

Wave attenuation by vegetation is from far the most studied physical process in the scope of this thesis in an experimental and analytical point of view. Several parameters play an important role and have to be considered to have the ability to predict the wave transformation over a vegetation field. Multiple analytical models and laboratory experiments have been developed to reproduce this complex process (Kobayashi et al. 1993, Dubi and Torum 1995, Mendez and Losada 1999, Mendez and Losada 2003, Asano 2006, Lovstedt 2010). Wetland vegetation is known to accentuate wave energy dissipation through the work applied on the vegetation stems and results in a decrease in wave height (Dalrymple, Kirby and Hwang 1984). Typically, coastal wetland plants, such as *Spartina alterniflora* (smooth cordgrass) are experimentally represented as an array of circular cylinders of diameter d for correspondence in shape and in rigidity at the base.

Dalrymple, Kirby & Hwang (1984) have derived an analytical solution that has been used broadly as a foundation to apply and enhance the wave height reduction by vegetation theory. This solution has been derived using the conservation of energy equation in its general form for monochromatic waves:

$$\frac{d(EC_g)}{dx} = -\Big\langle \epsilon_v \Big\rangle \tag{2.1}$$

C_g is the group velocity of the wave train and $-\Big\langle \epsilon_v \Big\rangle$ is the energy dissipation term. The quantity E represents the wave energy per unit area and is defined for waves of height H using linear wave theory (Dean and Dalrymple 1984) by:

$$E = \frac{1}{8}\rho g H^2 \tag{2.2}$$

This solution has been derived based on some assumptions to simplify the initial setup of the equations. The model neglected the non-linear effect using linear wave theory for unidirectional waves and using rigid vertical cylinders to discard any vegetation motion effect. Wave reflection induced by the plant was neglected and the waves were traveling on a flat bottom at an arbitrary water depth. Hence, to substitute the expression of the energy dissipation, Dalrymple et al. (1984) formulated a dissipation equation model where ϵ_v was only due to the drag force F_D generated by the vegetation (subscript v) such that: $\epsilon_v = F_D u$. The Morison type equation was used to express the horizontal force per unit volume of the rigid vegetation stems on the fluid, discarding the inertia force component:

$$F_D = \frac{1}{2}\rho C_D N b u|u| \tag{2.3}$$

In Equation 2.3, N represents the number of vegetation stands per unit horizontal area, b area per unit height of each vegetation stand normal to u which is the horizontal particle velocity given by linear wave theory. The dissipated energy was formulated for waves of amplitude a propagating over an array of rigid cylinders of length s and was given by:

$$\left\langle \epsilon_v \right\rangle = 2\rho \frac{C_D}{3\pi} \frac{d}{k} \frac{\sinh^3 ks + 3\sinh(ks)}{3\cosh^3 kh} \left(\frac{gk}{\sigma}\right)^3 \frac{a^3}{b^2} \tag{2.4}$$

The geometric properties of the cylinders are given by s which is the average height of the stems and b which is the average spacing between the stems. Solving equation 2.1 for a, given the input waves of amplitude a_0, the expression of the amplitude varied as a function of x and a wave damping factor α as follows:

$$\frac{a}{a_0} = \frac{1}{1 + \alpha x} \tag{2.5}$$

$$\alpha = \frac{2C_D}{3\pi} \left(\frac{D}{b}\right) \left(\frac{a_0}{b}\right) [\sinh^3 ks + 2\sinh ks] \left[\frac{4k}{3\sinh kh(\sinh 2kh + 2kh)}\right] \tag{2.6}$$

Using the same formula to express the drag force induced by the vegetation field, Kobayashi, Raichle & Asano (1993) have introduced an analytical model for wave propagating over submergent vegetation. Considering two sets of equations, the first for the region within the vegetation (subscript 2) and the second above the vegetation (subscript 1), the two dimensional time averaged continuity and momentum equations have been used to find a converging solution satisfying the boundary conditions at the interface. The two dimensional continuity equations for the velocity in both media was given as follows, for z taken vertically upward and x is in the wave direction of propagation:

$$\frac{\partial u_i}{\partial x} + \frac{\partial w_i}{\partial z} = 0 \qquad \text{where } i = (1, 2) \tag{2.7}$$

The effect of the vegetation was considered by allowing a dissipation term in the linearized momentum equations as shown in Equation 2.8 and 2.9.

$$\frac{\partial u_2}{\partial x} = \frac{\partial p_2}{\partial x} - F_x \tag{2.8}$$

$$\frac{\partial w_2}{\partial x} = \frac{\partial p_2}{\partial z} - F_z \tag{2.9}$$

Using the force equation model chosen by Dalrymple et al. (1984), the vertical component of the drag force F_z was approximated to be negligible and F_x verified the equation given by 2.3 such that $F_x = F_D$. The matching conditions at the interface between the fluid and the vegetated porous medium stated that the respective vertical component of the velocity had to be equal, and the same condition applied to the dynamic pressure such that:

$$\left.\begin{aligned} w_1 &= w_2 \\ p_1 &= p_2 \end{aligned}\right\} \quad \text{at the interface.}$$

The conservation of energy equation was derived from the momentum equation and led to an analytical solution for the wave height decay expressing an exponential decrease of the input wave height, H_0, as the wave propagates over the submerged cylinder array:

$$H = H_0 \exp(-k_i x) \tag{2.10}$$

This wave energy dissipation was modulated by the imaginary part of the complex wave number $\tilde{k} = k_r + k_i$ where k verified the dispersion relationship given by Equation 2.11 for a given water depth h.

$$\omega^2 = kg \frac{\tanh(kh) + \alpha \tanh(\alpha d)}{k + \alpha \tanh(\alpha d) \tanh(kh)} \tag{2.11}$$

Corresponding laboratory experiments using artificial kelp have been carried by Asano (2006) (Figure 4) and the results have been compared to this analytical model. This laboratory setup used flexible artificial kelp and has been commonly used as the basic setup to test wave damping by vegetation for the cylinder based model as well. Experimental data were plotted against the theoretical curve (Equation 2.10) expressing the exponential decay of the wave height and showed a good agreement in following the trend measured in the experiment, falling within ±10% of the theoretical

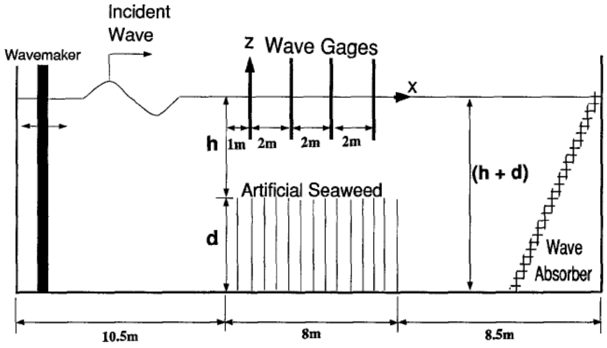

Fig. 4. Experimental setup (from Asano et al. 2006).

curve as shown in Figure 5.

Mendez & Losada (2003) have accounted for the influence of the breaking force on the vegetation induced by random waves breaking over the vegetation field in addition to the drag force, at a miultiple water depths. Indeed, most of the previous models considered flat bottom. Extending the study to sloped bottom and considering the breaking of the waves in the vegetation field was more likely to represent a closer model to real wave transformation as in nature. The expression of the wave energy dissipation became (Mendez & Losada 2003):

$$\frac{\partial(EC_g)}{\partial x} = -\left\langle \epsilon_b \right\rangle - \left\langle \epsilon_v \right\rangle \tag{2.12}$$

The major assumption in this model compared to equation 2.1 was to consider valid the linear summation of the energy dissipated by the vegetation $\left\langle \epsilon_v \right\rangle$ given by Equation 2.4 and the energy dissipated by the breaking of the waves $\left\langle \epsilon_b \right\rangle$. Assuming straight and parallel contours of sloped bottom where the waves propagate normally toward the vegetation field, the expression of the energy dissipation per unit area due

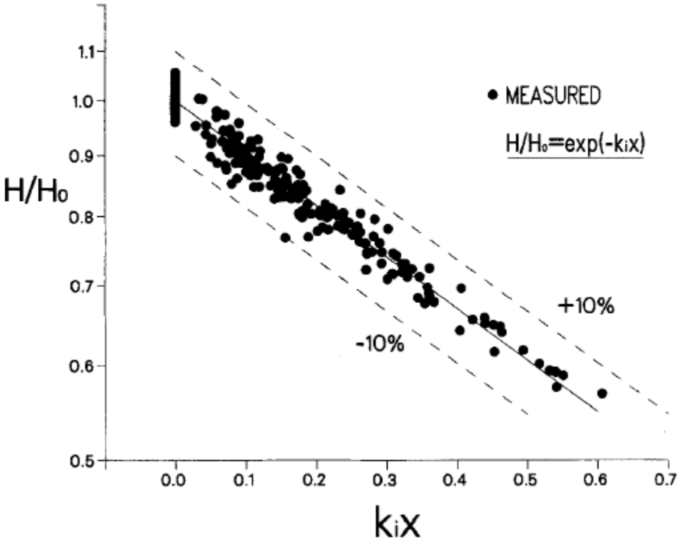

Fig. 5. Model waveheight fitted to exponential decay model (modified from Kobayashi et al. 1993).

to breaking was given by:

$$-\left\langle \epsilon_b \right\rangle = \frac{3\sqrt{\pi}}{16}\rho g \frac{B^3 f_p}{{\gamma_b}^4 h^5} H_{rms}^7 \tag{2.13}$$

In this model, B and γ_b were constants that were used to adjust the equation to experimental data and $f_p = 1/T_p$ was the average peak frequency. This linear model of wave energy dissipation has been shown to be valid when comparing this numerical model to experimental data, however, no investigation on the wave shape transformation was included in this study. Solving Equation 2.12 in the shallow water case (i.e. $kh << 1$) lead to the following approximation of the energy dissipation equation for random waves:

$$\frac{\partial(H_{rms}^2 h^{1/2})}{\partial x} = -C_1 \frac{H_{rms}^7}{h^5} - A_1 \frac{H_{rms}^3}{h^{1/2}} \tag{2.14}$$

For a given root-mean-square wave height, H_{rms}, the constant A_1 has been obtained analytically for monochromatic waves propagating normally through a vegetation field on a plane sloping beach. The term associated with A_1 characterized the presence of the vegetation in the wave damping. By the same process, C_1 was associated with the breaking of the waves. Hence, both terms on the right hand side of Equation 2.14 contributed to the energy dissipation as shown in Figure 6. As can be seen, the results showed that the association of the contribution of the damping by breaking and by the vegetation to the system created a greater damping than each contribution taken separately. Focusing on the damping caused by shoaling and vegetation only, the ratio tendency of the nondimensional root-mean-square wave height evolution as a function of the water depth to increase slowly compared to the shoaling restricted case ($A_1 = 0, C_1 = 0$), demonstrated that the vegetation ratio of H_{rms}/h was reduced by the presence of the vegetation, inducing the waves to break further offshore. The experiment by Lovas et al. (2001), used a 30 m×5 m×0.6 m wave tank where a

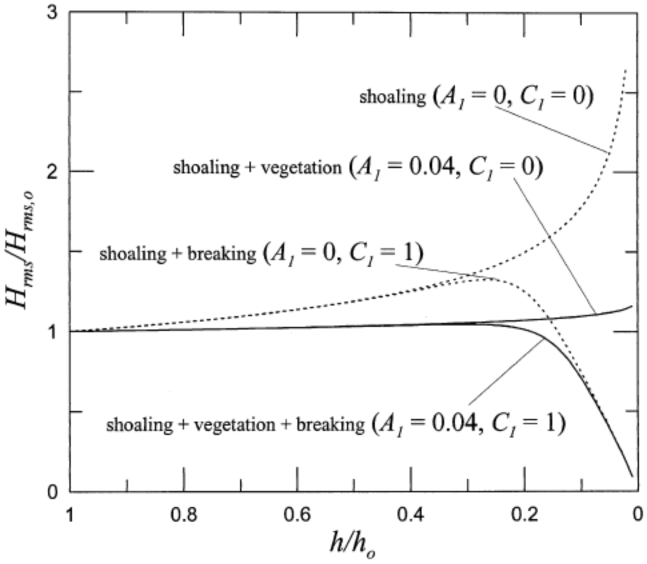

Fig. 6. Nondimensional root-mean-square wave height evolution of H_{rms} using on a plane sloping beach for different case (from Mendez and Losada 2003).

synthetic vegetation simulating *L. hyperborea* were embedded on a sandy slopped bed with a density $N = 1200\ \mathrm{m}^{-2}$. Therefore, this experiment included the dissipation of energy by breaking and by vegetation of random waves. Thirteen test cases were run for varying water depth, peak period and significant wave height. Using 10 wave gauges including one in the offshore part of the wave tank to measure the input wave conditions, nine wave gauges were used to measure the water level evolution on the sloping bed, over the vegetation field. Comparison between the measured data and the numerical model simulation is shown is Figure 7 and shows good agreement.

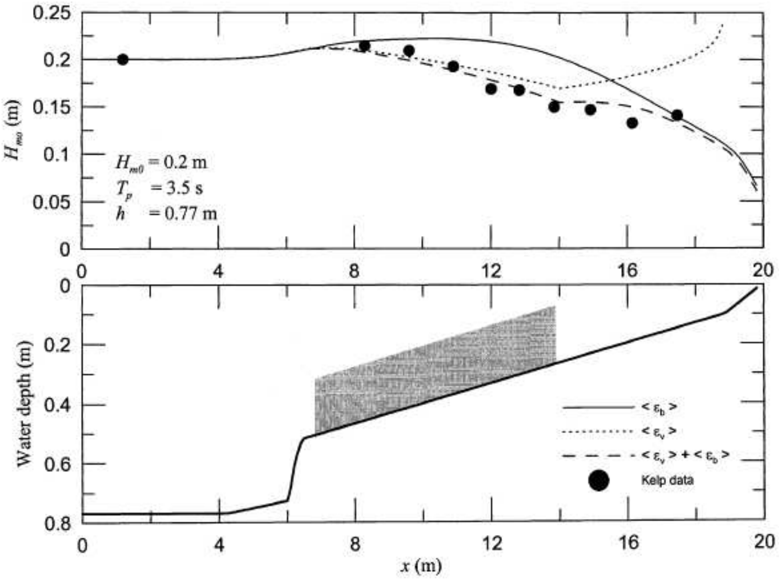

Fig. 7. Measured and calculated significant wave height H_{m0} for the different energy dissipation models (from Mendez and Losada 2003).

C. Hydrodynamic Flow in Vegetated Channel and Variable Bathymetry under Wave Forcing

Additional interaction of waves in the system were likely to make the hydrodynamic process more complex but the understanding of its features was of great importance to evaluate the benefits and the losses due to wave induced flow in severe hydrodynamic conditions. Kobayashi et al. (1993) have demonstrated that the local flow field is affected by the presence of the vegetation and the latter has the potential to interfere with the phenomena related to sediment transport, even in the case of small wave damping. Indeed, the horizontal velocity of the fluid relative to the horizontal velocity of the vegetation increased as the drag coefficient decreased. Hence, the flow velocity was directly related to the height, the width and the number of vegetation stands. The use of the linear conservation of momentum equations and the continuity equation lead to the following complex expression for the velocity above (subscript 1) and within the vegetation field (subscript 2):

$$u_1 = \frac{k}{\rho\omega} p_1 \qquad w_1 = -\frac{i}{\rho\omega}\frac{\partial p_1}{\partial z} \tag{2.15}$$

$$u_2 = \frac{k}{\rho(\omega + iD)} p_2 \qquad w_2 = -\frac{i}{\rho\omega}\frac{\partial p_2}{\partial z} \tag{2.16}$$

In the case of small damping, Kobayashi et al. (1993) have derived the equations of the total pressure in the two media using the free surface boundary conditions and the boundary condition at the interface as shown in the following equation in complex form:

$$p_1 \approx \rho g \frac{H}{2}\Big(\frac{\cosh(k_r(h+d+z))}{\cosh(k_r(h+d))} + i\delta c_1\Big)\exp[i(k_r x - \omega t)] \tag{2.17}$$

$$p_2 \approx \rho g \frac{H}{2}\frac{\cosh(k_r(h+d+z))}{\cosh(k_r(h+d))}[1 + i\delta c_1 + i(\delta - \epsilon)c_3]exp[i(k_r x - \omega t)] \tag{2.18}$$

Here, ϵ was defined as a nondimensional damping coefficient which verified $\epsilon << 1$ for very small damping, hence, the equation for the total pressure have been approximated to the order ϵ, neglecting any higher order. The additional terms in the expression of p_2 were related to the vegetation contribution to the total pressure, implying its contribution to the flow velocity as well, according to equations 2.15 and 2.16. It has also been shown that the presence of the vegetation slightly increased the wavenumber, shortening the wavelength and decreasing the phase velocity of the waves over the vegetation field.

Mendez et al. (1999) have developed a linear model of monochromatic wave interaction with a submerged flexible vegetation field assuming inviscid fluid and irrotational flow outside of the vegetated region. Hence, velocity potentials have been defined for the total wave field considering a four regions system. The four velocity potentials were defined in Figure 8 as follows: a region seaward of the vegetation field (Φ_1), above the vegetation field (Φ_2), leeward of the vegetation field (Φ_3) but also within the vegetation field (Φ_4) using an anisotropic flow assumption. In region 4, a horizontal force per unit volume acted on the vegetation field following the Morison's equation model for the total force per unit length on slender cylindrical members, discarding any vertical component (Mendez and Losada 1999):

$$F_x = \frac{1}{2}\rho C_D N d u_r |u_r| + \rho N d t_v \left[C_M \frac{\partial u}{\partial t} - (C_M - 1)\frac{\partial^2 \zeta}{\partial t^2} \right] \tag{2.19}$$

In this equation, u_r was defined as the relative horizontal velocity between the fluid and vegetation stand. The Morison-type equation model has been used by several authors (Dalrymple et al. 1984, Kobayashi et al. 1993) which considered no swaying motion of the plant and neglected the inertia force induced by the plant on the fluid. As the drag force was expressed with respect to the relative velocity between the fluid and the stems, it has been shown to be valid for flexible plants as well. Solving for each velocity potential by applying the boundary conditions in each region, Mendez et al. (1999) validated the analytical solution obtained with previous models and experimental results. Besides the good agreement of the model, no influence of possible boundary layer effect appeared in the model, which would contradict results obtained for current flow (Ghisalberti and Nepf 2009). The present solution takes into account reflection and transmission of waves at the front end and back end of the vegetation field and a convergent solution was found for the interaction between the fluid equation of motion and the vegetation motion equation using an iterative process. The analytical solution for regular waves was compared to experimental results and a previous solution introduced by Kobayashi et al. (1993) based on an exponential decay. The Figure 8 below shows a very good agreement between experimental data and analytical solution including the modulation of the wave height H:

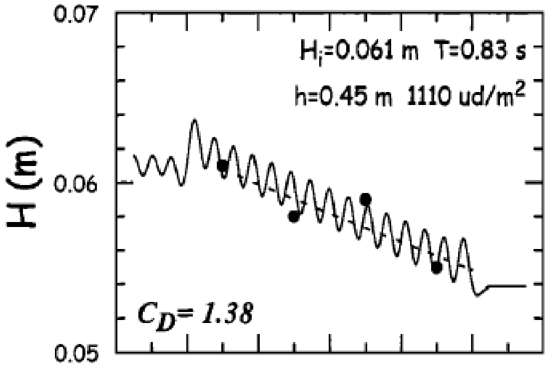

Fig. 8. Comparison between numerical (solid line) and experimental (dots) results of the evolution of the wave height over a submerged vegetation field. The dash line represents the wave height evolution for an exponential decay (from Mendez and Losada 1999).

Extension from a one-dimensional model where the waves propagate normally into the vegetated area to a quasi-two dimensional model has been developed by Asano (2006) for a sinusoidal wave train normally propagating in the vegetation field. An analytical model has been developed to account for the momentum exchange in a vegetation fringed channel where still water mass interacted with fast flowing water mass in the central area in a uniform shallow water depth and described by equation 2.20, 2.21 and 2.22.

$$\frac{\partial \eta}{\partial t} + \frac{1}{n}\frac{\partial (nQ_x)}{\partial x} + \frac{1}{n}\frac{\partial (nQ_y)}{\partial y} = 0 \tag{2.20}$$

$$\frac{\partial Q_x}{\partial t} + c^2 \frac{\partial \eta}{\partial x} = -\frac{1}{2}(f_b + f_v)|Q|\frac{M}{h^2} + A_h\left(\frac{\partial^2 Q_x}{\partial x^2} + \frac{\partial^2 Q_x}{\partial y^2}\right) \tag{2.21}$$

$$\frac{\partial Q_y}{\partial t} + c^2 \frac{\partial \eta}{\partial x} = -\frac{1}{2}(f_b + f_v)|Q|\frac{Q_y}{h^2} + A_h\left(\frac{\partial^2 Q_y}{\partial x^2} + \frac{\partial^2 Q_y}{\partial y^2}\right) \tag{2.22}$$

c and n were the phase velocity and the group velocity respectively. $Q = \sqrt{Q_x^2 + Q_y^2}$ was the total volume flux, A_h was a horizontal mixing coefficient and f_b and f_v described the bottom friction factor and the vegetation drag coefficient respectively. The model setup is given in Figure 9. In the analytical solution derived by Asano, Matsumoto & Kikuchu (2005), wave attenuation was found to be proportional to the bottom friction factor f_b, the drag coefficient C_D, the vegetation stem diameter, the vegetation density and inversely proportional to the square root of the water depth. Also, in a hypothesis of long wave theory, invariance with respect to the wave period implies that the angular frequency of the waves did not affect the rate of attenuation. The numerical solution has been used to evaluate the effect of the vegetated area width with respect to the width of the channel on the wave transformation as shown in Figure 10. Wave attenuation increases as the width of the vegetation B_v increases and affects the wave attenuation in the main channel due to the exchange of momentum

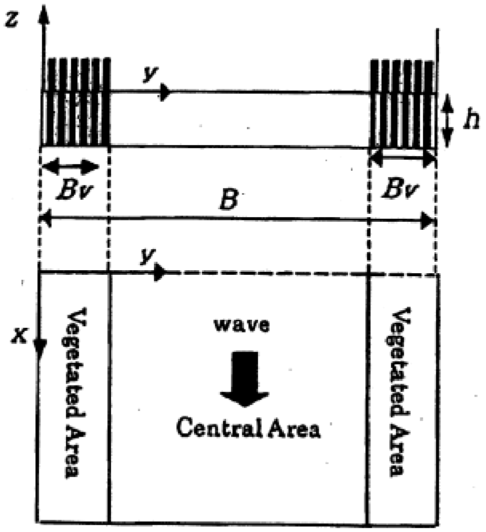

Fig. 9. Model of vegetation fringe channel (from Asano et al. 2006).

between the two media. Wave attenuation in composite channel has been shown to be the results of the interaction and momentum exchange within the vegetation fringe, leading to wave damping in the main channel as the vegetation density increases.

Haller, Dalrymple & Svendsen (1997) have conducted a large experimental study in order to generate and understand the complex structure and formation of a rip current system. Rip currents are driven by longshore variation in wave height. The experimental setup included three longshore directed sandbars which separated two rip channels as shown in Figure 11. This investigation was directed toward the change of nearshore wave height by variable bottom bathymetry. A cross-sectional view of the experimental setup is given Figure 12. The plane beach had a slope of 1:30 attached to a steeper toe structure of slope 1:5. This platform was made of concrete. The bars were 6 cm in height, 1.8 m in width and molded into a parabolic shape at their ends.

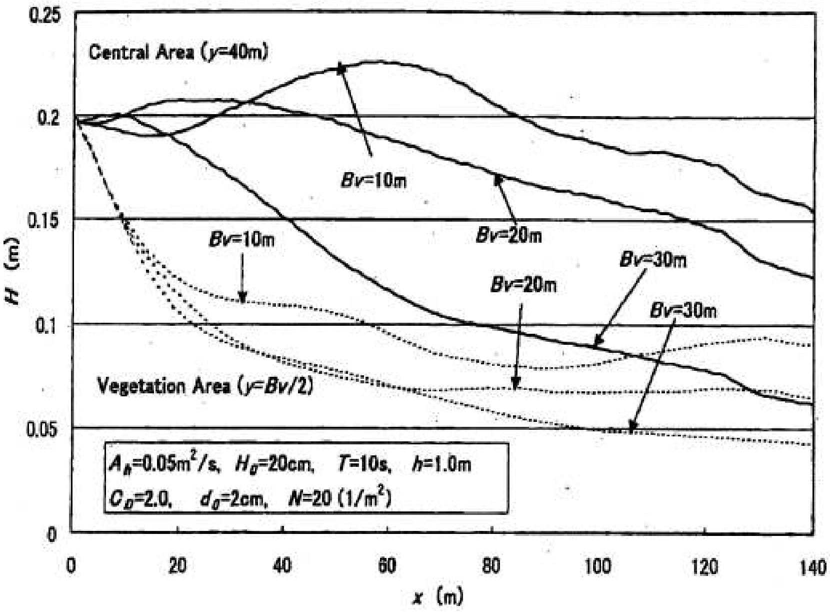

Fig. 10. Effect of the ratio of the vegetation width and the channel width on wave attenuation (from Asano et al. 2006).

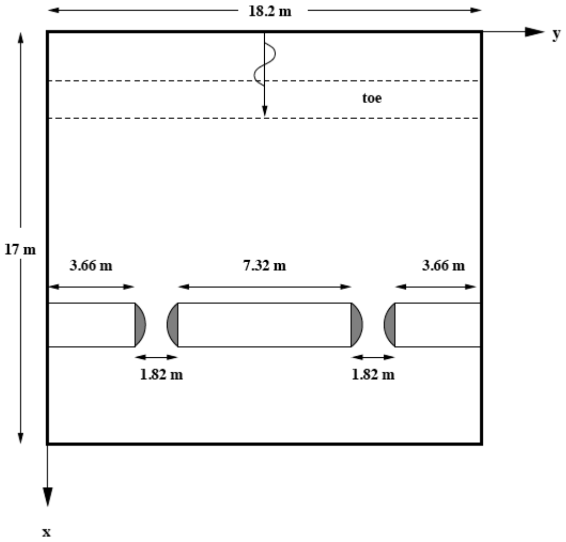

Fig. 11. Plan view of the experimental basin (modified from Haller et al. 2000).

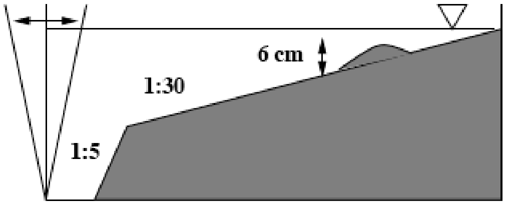

Fig. 12. Cross-section of the experimental basin (modified from Haller et al. 2000).

To acertain the symmetry of the system, the experimental setup included a long bar placed in the middle of the basin of length 7.3 m and two shorter bars of length 3.6 m placed on both sides at the same distance from the central bar. Using capacitance wave gauges and a set of three ADVs, measurements were taken shoreward, offshore, and on the bar but mostly concentrated in the rip channel as shown in Figure C.

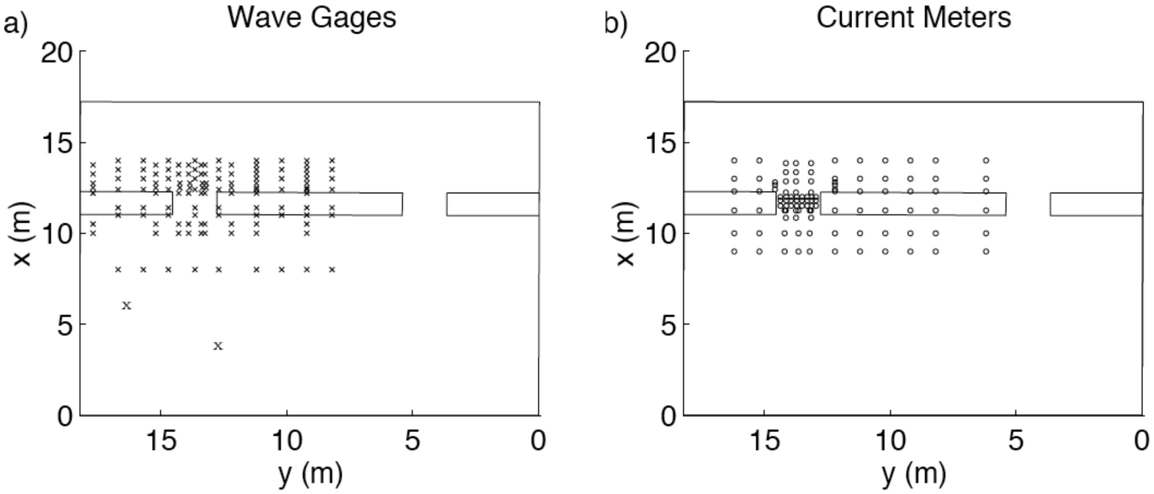

Fig. 13. Sampling locations (from Haller et al. 1997

).

Normally incident waves of height 4.8 cm were generated and the resulted root-mean-square wave height, H_{rms} and mean water level $\bar{\eta}$ are plotted in Figure 14(a) and (b) respectively. In the offshore part of the basin, the variations of both quantities are small. In contrary, in the breaker region on the top of the bar, an increase in the mean water level along with higher mean wave height were considerable. An important feature of a rip channel was detectable as the waves break after the breaker zone and hence, produced higher wave height and a slight wave setdown nearshore, in the

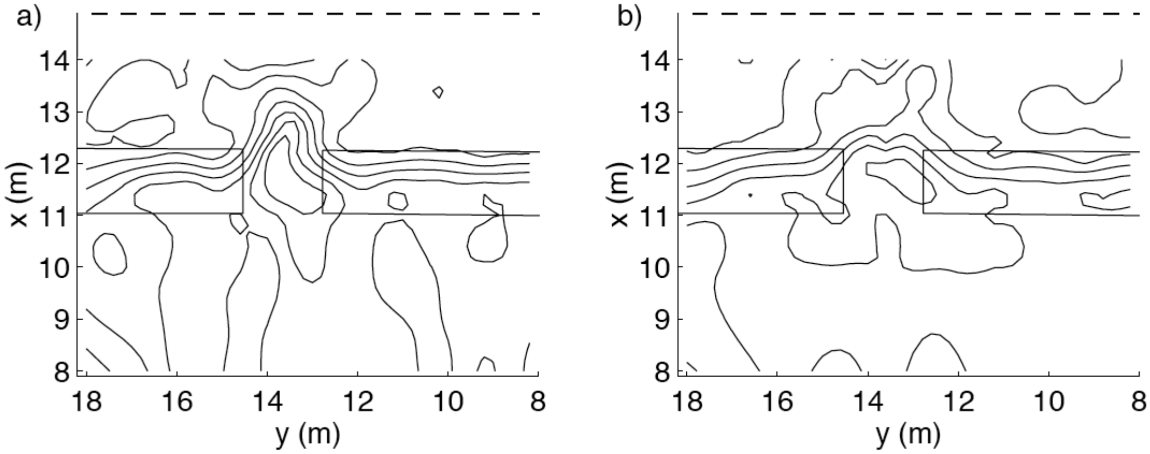

Fig. 14. Contour plots of H_{rms} and $\bar{\eta}$ (from Haller et al. 1997).

channel. The steep variation in the mean water level were identified to be directly related to the formation of the rip current.The velocity vectors generated by the ADV measurements shows a strong and narrow current in the rip neck. Longshore current directed toward the ripneck were measurable directly behind the bar from the strong wave breaking and directed toward the ripneck. However, the late wave breaking in the channel created wave setup at the shoreline, and a longshore gradient created currents directed away from the channel as shown in Figure 15. Experimental observations have shown migration of the rip current in the rip channel. Indeed, video records during the experiment showed that the point of breaking in the channel move back and forth attesting of the periodic migration of the rip current. This experiment was the most comprehensive dataset obtained in the study of rip current dynamics in varying bathymetry under wave forcing and it helped in verifying previous theories about the generation of rip currents.

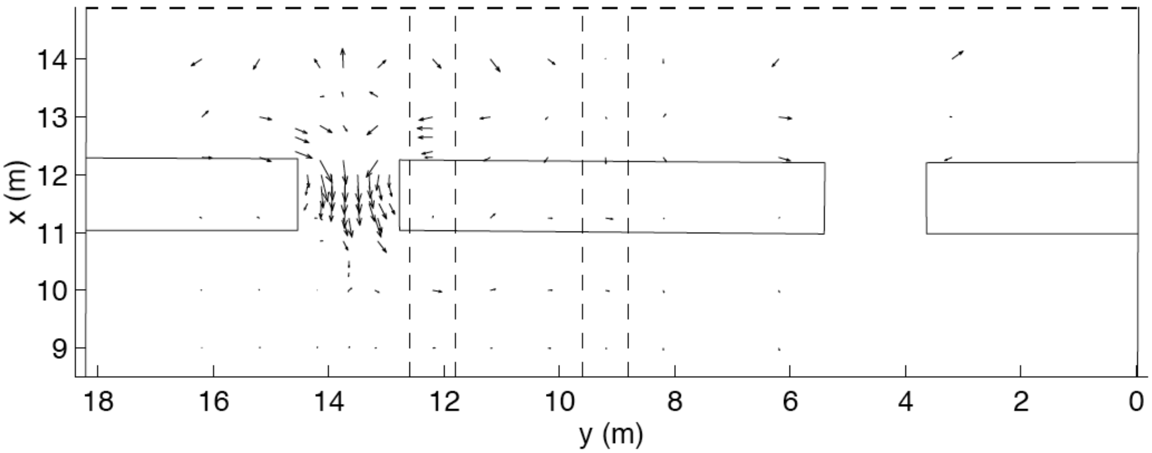

Fig. 15. Time averaged current velocities vector field (modified from Haller et al. 1997).

D. Hydrodynamic Flow in Vegetated Channel and Variable Bathymetry under Current Forcing

A shallow water depth and variation in bathymetry due to mounds of soil as well as submerged or emergent vegetation are some of the features that differentiate wetlands from other ecosystems. Flow structures in this unique morphology have been investigated broadly starting from basic models to recreate and understand vegetated flow dynamics. It has been shown that the drag force induced by the vegetation field increases as a function of the vegetation density, hence providing a greater reduction in flow speed compared to the flow speed within the marsh fringe. The introduction of vegetated area also impacts on the turbulence structures by generating small scale eddies to the scale of the stem-diameter and stem-spacing. Wetland marsh are however composed of multiple length scales and the large scale structures are going to be at most interest in this study.

The study of composite channel flow with fringing vegetation have been investigated mostly in laboratory experiments simplified to one-dimensional and two-dimensional setup. However, a lack in describing lateral flow and turbulence structure in one-dimension emphasized the need to design two-dimensional experiments to be able to describe the features of the interface between the channel and the vegetation edge. Nepf et al. (2004) has experimentally demonstrated that the shear layer split into two distinct regions in a shallow water depth. The first region was a region of transition at the fringe of an emergent vegetation field where the velocity is subject to an inflection point with high shear as opposed to a second region where the velocity undergoes a smooth transition in the main channel to a region of uniform flow. This configuration was the result of the balance between the bottom friction of the channel and the pressure gradient induced by the cylinder array drag. The experimental setup is given in Figure 16. White and Nepf (2008) have demonstrated that the vegetation field can be considered as a porous media. The significant shear at the interface due to the discontinuity of the drag of the array of cylinders participates to the generation of coherent vortices at the fringe. The dissipation of energy due to the drag acting on the side of the vortex that penetrates into the array was counter-balanced by the sweeps of the uniform flow in the channel maintaining the kinetic energy balanced with the dissipation due to the drag.

Comparison between vegetated and unvegetated channel have been studied experimentally considering an identical uniform flow rate for both cases. The mean kinetic energy was converted into turbulent kinetic energy as vegetation stems were introduced as an obstruction to the flow. For a steady flow, U, Nepf et al. (1999) has developed a scaled equation model for the depth-averaged turbulent kinetic energy accounting for the turbulent production from the bed shear and the wake production.

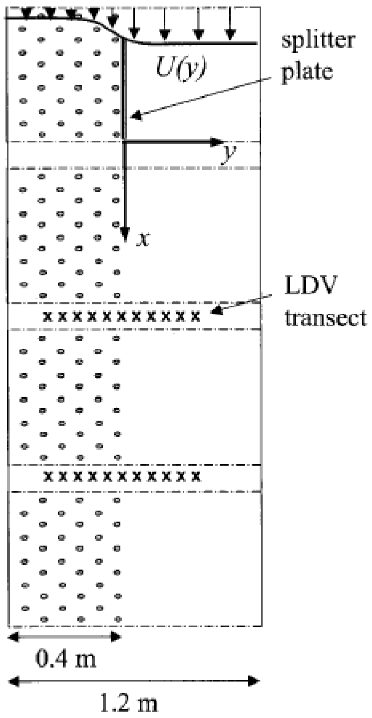

Fig. 16. Top view of the laboratory flume setup and mean velocity profile (modified from Nepf et al. 2004).

The summation of those two terms gave rise to the following equation:

$$k = (1 - ad)C_B U^2 + [\bar{C_D} ad]^{2/3} U^2 \qquad \text{(for } ad \text{ close to 0 or 1)}, \tag{2.23}$$

where C_B was defined as the bed drag coefficient and C_D represented the bulk drag coefficient from the array of cylinders. This turbulent kinetic energy operated at the stem scale affecting the turbulence intensity at large scale. The ratio of the turbulent kinetic energy in unvegetated flow, k_0, has been shown to be greater than the turbulent kinetic energy in vegetated flow, k, as shown in the Figure 17. The dashed line plots the turbulence ratio $k/k0$ for a value of $C_B = 0.001$ and the solid line plots the turbulence ratio $k/k0$ for a greater value of $C_B = 0.005$. Change in stem population, ad, induced an increase in the turbulent kinetic energy ratio up to $O(10)$ as the vegetation field gets denser attesting an increase in turbulence production generated by the stem wakes. The effect of the vegetation field on the mean velocity has been studied under a given forcing. Hence, imposing a given surface slope, comparison in the mean flow velocity ratio between vegetated and unvegetated channel has been shown to be less than 1 and as the array of cylinders generate

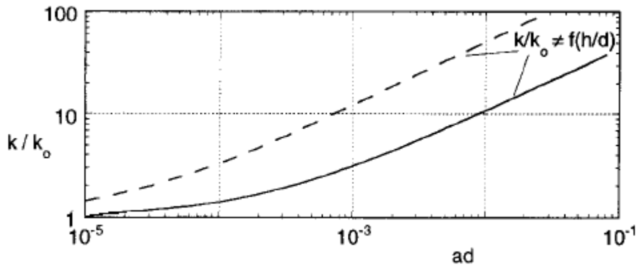

Fig. 17. Comparison of turbulent kinetic energy for vegetated and unvegetated channel at steady flow (modified from Nepf et al. 1999).

additional resistance to the flow, the mean velocity decreased as a function of *ad*. In addition, for a given stem density, an increase in water depth to stem-diameter ratio contributed to a greater reduction in the mean velocity as shown in Figure 18(a). For a given stem diameter, the deeper the water depth, the less effective the vegetation is in decelerating the flow. As a result, the turbulent kinetic energy is then balanced by the mean velocity variation as well as the turbulence production in the vegetation field. As the stem population *ad* increased, the mean velocity ratio U/U_0 decreased. For *ad* ranging from 0 to 10^{-2}, the production term was dominant over the velocity fluctuation resulting in an increase in the turbulent kinetic energy ratio. A lower bed drag coefficient C_B generated less turbulence in that region as expected. Whereas, at larger value, $ad \geq 3 \times 10^{-4}$, the mean velocity decrease became dominant resulting

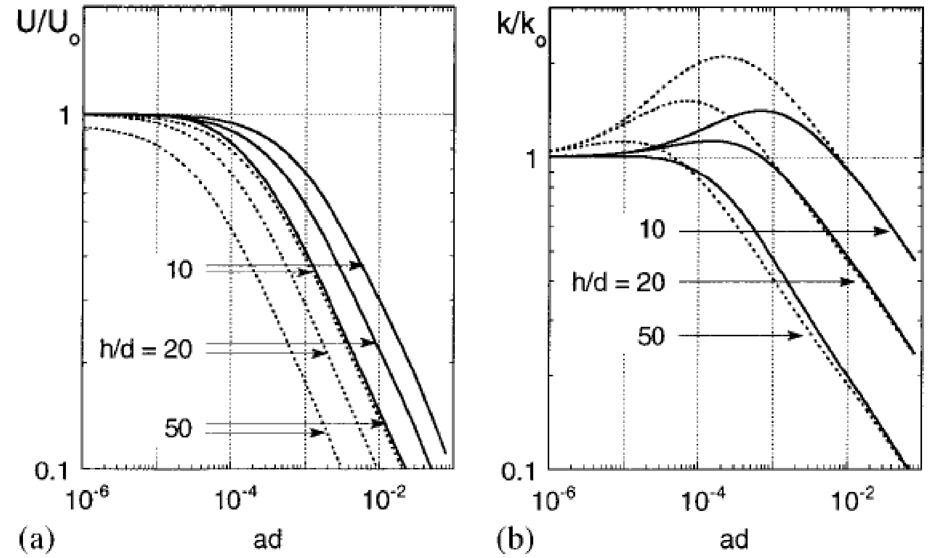

Fig. 18. Comparison of mean velocity and turbulent kinetic energy for vegetated and unvegetated channel at a given forcing. Bed drag coefficient $C_B = 0.001$ (dashed line) and $C_B = 0.005$ (solid line) (modified from Nepf et al. 1999).

in a decrease in turbulent kinetic energy ratio along with the decrease in the mean flow rate as shown in Figure 18(b).

Further investigation on the effect of vegetated patches in shallow water have been carried out experimentally to try to understand the interaction of current flow and seagrass patches. The spacial distribution of the vegetated patches has been of great interest since the effect on the flow field surrounding the patches were expected to be significant at the macro scale. Folkard et al. (2005) have identified and quantified the mean flow characteristics as well as the turbulence pattern in simulated patched of *Posidonia oceanica*, a common seagrass found in the Mediterranean Sea. Three different configurations of the patches were considered: the first only included one patch; the second included two patches spaced such that the second patch was placed downstream to the first and at a distance considered to be one wake length-scale; the last configuration was similar to the second except that the patch was placed in a “further wake” region as shown in Figure 19. The use of flexible material (polyethylene sheeting) to simulate the seagrass allowed to account for similarity in motions of that particular vegetation as found in nature. Each stem was about 50 cm long and the depth in the flume was held constant for all runs to 70% of the stem length (= 35 cm) in shallow water. The three tested flow speeds were referred to as a fast flow case of average speed 0.24 ms^{-1}, a medium flow of 0.16 ms^{-1} and a slower flow of 0.08 ms^{-1}. Preliminary observations suggested that the increase in flow discharge increased with the degree of bending of the vegetation field. The top of the canopy was measured to be at an elevation z = 30 cm, 22 cm and 17.5 cm from the fast, medium and slow flow rate, respectively. Sampling of ADV measurements on a horizontal and vertical grid in the flume, downstream of the patch has shown similar circulation patterns for each configuration. A recirculation cell formed leeward of the vegetation field in the single patch case whereas a weak

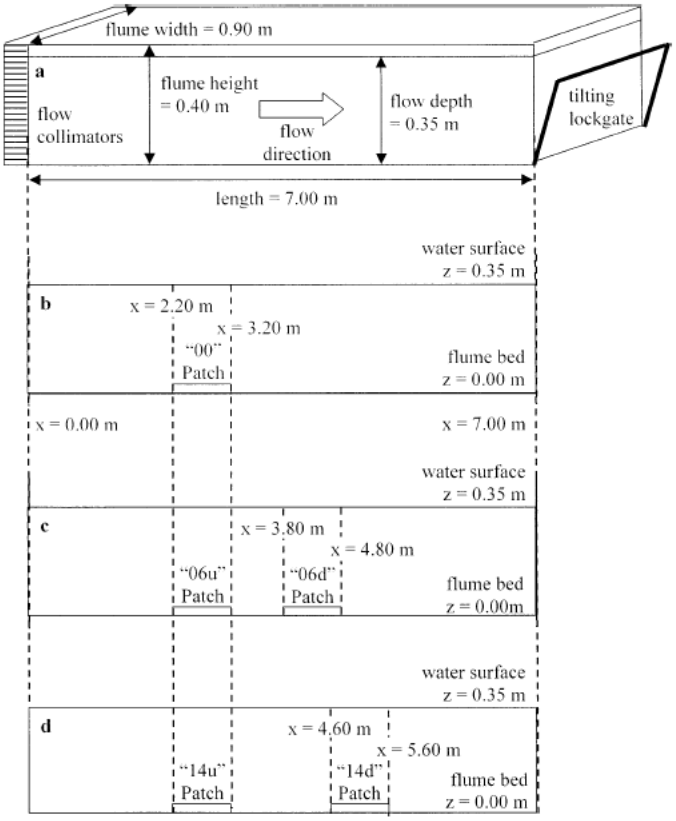

Fig. 19. Experimental setup (from Folkard et al. 2005).

upwelling was detected for the double patches case. For the three cases, a similar wake was formed behind the upstream patch but weakened when interacting with the front end of the second patch. In addition, the stronger the flow discharge, the more significantly the wake was generated. Computation of the maximum vertical and horizontal turbulent kinetic energy (TKE) showed a common trend behind the canopy. Three hydrodynamics states have been identified relating the patch-wake relationship with respect to the patches spacing and the wake length. The first showed that if the distance between the patches was greater than the length scale of the wake, then the patches were hydrodynamically isolated from each other (Figure 20(a) and (c)). A second state showed that as the distance decreased, a strong patch-wake interaction occured preventing the wake from fully developing because of the lack of space (Figure 20(b)). The critical distance was reached when the two patches formed a single homogeneous patch that defined the third state in a more obvious way. In the case of storm-driven currents which generated strong currents, a prevailing of the unidirectional flow through the patch would then occur creating more turbulence downstream of the patch. However, further work is required to overcome a lack of study about these effects.

Additional experiments extend the study of vegetation hydrodynamics to submerged vegetation canopy and analyzed the effect in the flow at the top of the porous medium and at the upper interface. The added flow depth above the canopy increased the porosity through the water column allowing more vertical transport. The exchange of momentum and mass between the canopy and the surrounding open water regulated the hydrodynamic process in that region. Ghisalberti and Nepf (2006) have demonstrated the formation of large coherent vortices within the shear layer at the top of the canopy due to a street of coherent Kelvin-Helmholtz instability, for both rigid and flexible vegetation model. Figure 21 shows the vortex street generated

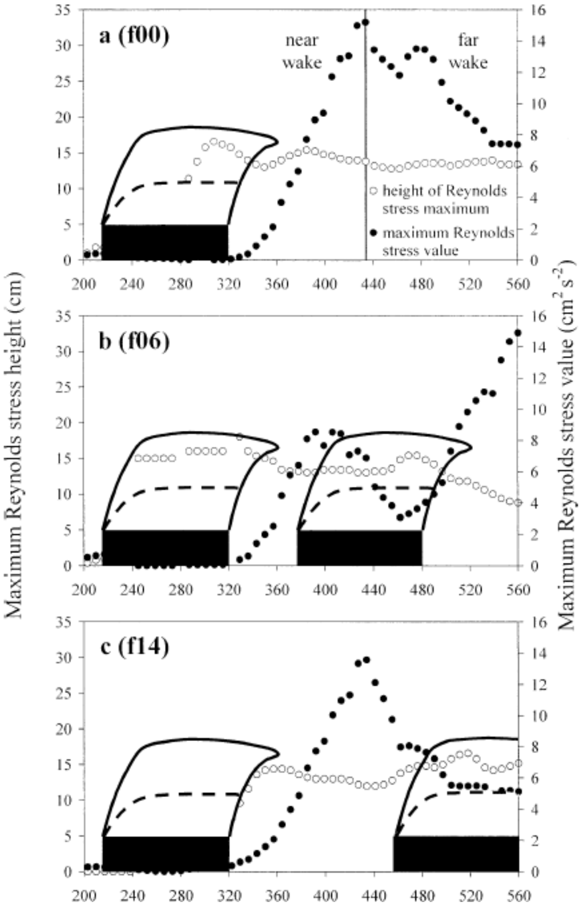

Fig. 20. Positions and values of maximum Reynolds stress vertical profile (from Folkard et al. 2005).

for submerged rigid canopy. As the Kelvin-Helmholtz vortices grew in the transition section as the shear layer grew downstream, an equilibrium was reached at a distance L_T from the front of the canopy as illustrated in Figure 22. In the case of flexible canopies, the vortex structure induced highly correlated coherent waving of the flexible synthetic vegetation, a phenomenon known as "monami" (Japanese for "waving water weed"). The amplitude of this phenomenon was approximately

Fig. 21. Dye visualization of vortex above rigid canopy (from Ghisalberti et al. 2009).

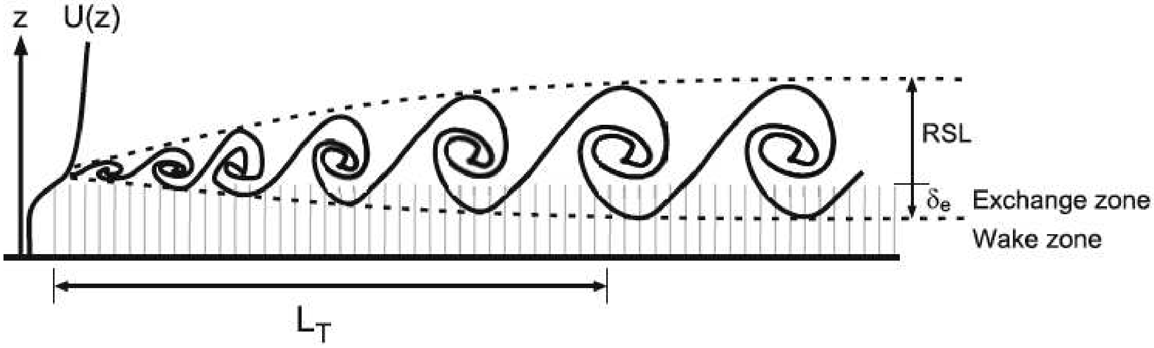

Fig. 22. Growth of a vortex street upstream of the canopy in the transition region of length L_T (from Ghisalberti et al. 2009).

30% of the maximum plant height. Significant analogy with an ideal mixing layer of the mean velocity and the Reynolds stress profiles, as shown in Figure 23, suggested that rigid canopies were more likely to generate larger vortices compared to flexible canopies. A first hypothesis about this effect implied that the rigidity of the stems induces a more constant drag on the flow due to unvarying geometry whereas a waving canopy produced spacial and temporal variability in drag due to change in height of the stems, creating more turbulent stress. The resultant drag has been shown to be 40% less for flexible stems than for rigid stems, generating an increase in the mean

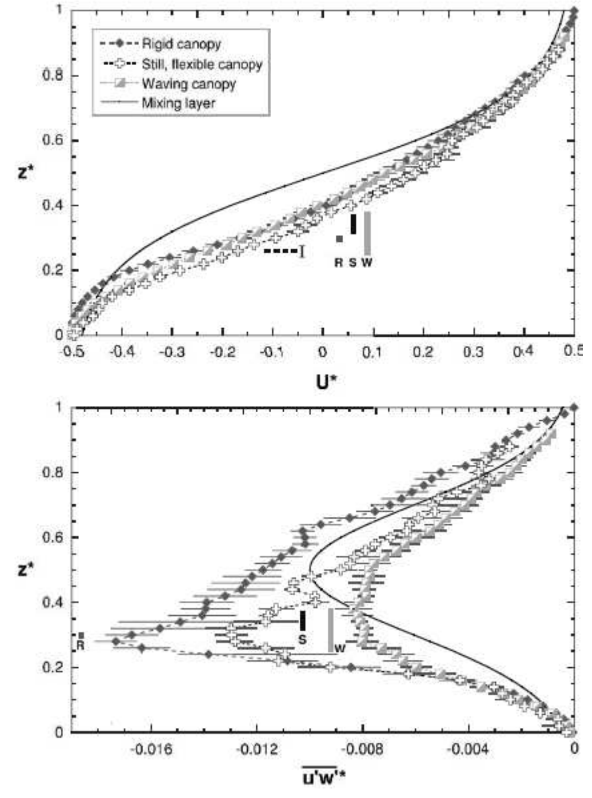

Fig. 23. Profiles of mean velocity and Reynolds stress compared to the mixing layer profiles (solid line)(from Ghisalberti et al. 2006).

velocity through the waving canopy. This mixing-layer type flow has been found to dominate the hydrodynamic process over the deceleration of the flow. The velocity profile as well as the vertical transport, i.e. the size of the vortices, did not vary beyond the length L_T characterizing the fully-developed flow region. Ghisalberti et al. 2009 had carried experimental tests to predict the location of L_T. The physical model was constructed on a 24 m long recirculating flume of width 38 cm with a flat bottom. The rigid model canopies consisted of cylindrical wooden dowels with random distribution, whereas the flexible canopies were constructed using polyethylene films to mimic eelgrass (*Zostera marina*). Experimental results indicated that the fluid deceleration partially governed the transition to equilibrium in canopy flow, in addition to the growth of the vortex street and the development of the mixing layer type region. The limited growth of the shear layer hence defined the transition to fully developed flow and implied the following approximation for the parameter L_T for flexible, waving canopies:

$$L_T \approx 3\left(\frac{U_h}{u_*}\right)(C_D a)^{-1} \tag{2.24}$$

U_h was defined as the characteristic mean advective velocity and u_* was the friction velocity in the fully-developed flow. $(C_D a)^{-1}$ representing a normalizing coefficient known as the drag length scale, was a measure of the fully-developed vortex size. The constant a is known as the frontal area per unit volume and therefore, has the units of m^2/m^3. The constant of proportionality could differ slightly for rigid canopies.

E. Summary of Literature Review

The information provided in the previous sections is directly related to the work done throughout this thesis and its research. The theory of wave damping over a vegetation field has been investigated from several angles as well as the interaction with flow field nearby. The hydrodynamic process occurring in these systems has shown to be highly variable and dependent on the plant characteristics such as geometry, buoyancy, density, stiffness and spatial configuration. The input wave parameters also play an important role in transforming the flow field and generating coherent structures. The cylinder-based model used to experimentally simulate the wetland type vegetation field such as smooth cordgrass *Spartina alterniflora* has shown its validity in various related research allowing the development of numerical models to simulate the wave transformation.

Vegetation patches are identified as localized areas of energy dissipation (Dalrymple et al. 1984, Asano 2006). The drag force added into the water column due to the presence of such porous media takes energy out of the waves resulting in a decrease in the wave magnitude. The intensity of magnitude change is related to the stem density as well as the rigidity of the stem. The more rigid the stems are, the more wave damping they generate. The large variability of vegetation types makes the study of wave attenuation by vegetation more complex. However, in this thesis, priority is given to the focus on the wetland type of vegetation known as *Spartina alterniflora*. Therefore, the cylinder-based model is used to simulate the vegetation field. The variable and particular bathymetry encountered in natural and restored wetlands located in shallow water coastal regions is likely to display specific flow pattern in addition to the wave damping induced by the great quantity of vegetated areas. Open wetland area becomes expose to waves and wave shoaling. Hence a breaker zone takes place and breaking generates marsh loss, more particularly through erosion. In general, marshes are characterized by broad and gently sloping features as shown by a topographic survey of marsh mound settlement in Figure 24. Covered in approximately 70% of the wetland area, clusters of mounds are scattered creating apparent

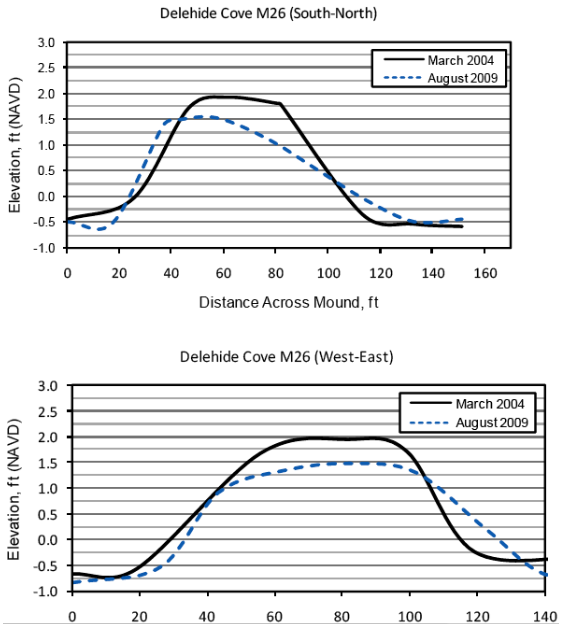

Fig. 24. Mound settlement rates and placement slopes (from HDR 2009).

channel delimited by patches of *Spartina alterniflora*. The mild bathymetry composed of mound has the potential to generated flow structures such as rip current where the rip channel would be located in the gap in between two marshes. The random location of marsh mounds in nature may generate more complex patterns. The present study is based upon previous research about wave and bottom bathymetry variation induced coherent structures combined with wave attenuation by vegetation and uses a simplified model of wetland to investigate the potential of a marsh mounds system in reducing storm damages on the coast. The combined effects of vegetation and variable bathymetry in wave hydrodynamics has not been investigated in previous research. An experimental study will be conducted to verify if the results and separated effects of the bathymetry and the vegetation obtained by previous studies are confirmed. Additional features such as the correlated effects of the bottom bathymetry variations with the vegetation is examined.

Fig. 25. Typical wetland landscape (http://www.fws.gov/coastal/contactInfo2.html).

The investigation of the coastal hydrodynamic process in wetlands at large scale and in storm conditions is a significant step toward the development of standardized criteria to improve the efficiency of marsh restoration work. This thesis focuses on the identification of coherent structures as a function of marsh segments spacing and geometry by collecting data through experimental laboratory work and follows previous research in studying the wave transformation over vegetated and unvegetated marsh segments with variable bathymetry. Therefore, the study of the wave energy dissipation is correlated to the turbulent energy created. The transfer of this energy from one system to another has the potential to generate structures in the flow field and the quantification of this potentiality is needed.

CHAPTER III

EXPERIMENTAL METHODS

The intent of the present chapter is to provide a complete description of the laboratory experiments, including the experimental procedures, the waves conditions and the detail of the data collection and processing. In addition, the present chapter will provide the necessary information to access the archived row data collection. This chapter is divided into six sections. Section A, and B provides the theoretical approach and the experimental design with the prototype used. Section C gives the information about the instrumentation and the data acquisition system and Section D describes the instrumental setup. The catalogue of measuring locations is given in Appendix A, and C with the coordinate system used in Figure 86. Section E details the numeric codes used to identify each test. Section F provides the necessary information for accessing the archived data set. Section G summarizes the pre-processing procedures.

A. Experimental Approach

A broad study of the marsh geometry on the Texas Coast has been done focusing on the wetlands located in the West Galveston Bay (HDR 2009).. Gathered information was used to get an overview of the marshes shape considering restored marshes. Indeed, Relative Sea Level rise (RSLR), including subsidence and Sea Level Rise, causes marsh main losses in this area, in addition to the erosion due to waves. Hence, the company HDR Engineering, Inc. (Corpus Christi, TX), had conducted between August and September 2009 a geotechnical investigation to determine the appropriate design for their restoration project, for three main locations: Dalehite Cove, Starvation Cove and Jumbile Cove. The main characteristics taken into account included the settlement and the slopes of the discharges dredged material, the characteristics of the sediments and the suitability of the borrowed material. Hence, marsh mound settlement rates and placement slopes resulting from previous restoration in 2004 were determined. The given topographic survey for mounds showed the “as-built” conditions in March 2004 compared to the post settlement conditions in August 2009.

B. Experimental Design

Marshes consist of soil formed into a cone-shaped mound with a broad flat top where the vegetation field stands. In this project, only marsh geometry from the Delehide Cove are considered for consistency. Five reference marsh mounds dimensions were reported in the survey with South-North and West-East top and base diameters, as shows Figure 26 as an example. In order to have a perfectly circular model in the experiment, only the South-North diameters were considered and averaged over the five mounds to have a consistent dimension in both directions. For the purpose of this project, the average top and base diameters over all the mounds were computed and hence, define the prototype dimensions considering an idealized conical mound

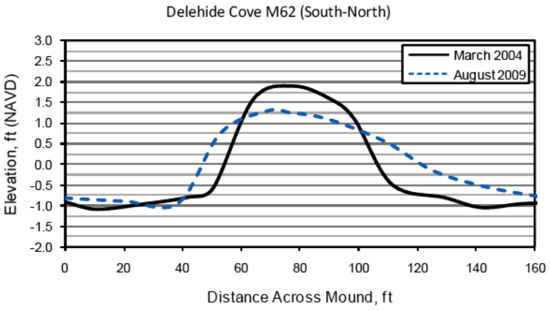

Fig. 26. Surveying results comparison from a selected marsh mound (M62) in the Dalehite Cove.

shape with circular base and top. Table 1 summarizes the dimensions of the selected marsh mounds along with the averaged dimensions.

Table 1. Summary of selected marsh mounds S-N dimensions and averaged values.

Selected mound	Base diameter(m)	Top diameter(m)	Elevation(m)
M26	34.7	13.1	0.62
M40	25.9	12.8	0.47
M49	39.6	16.5	0.38
M50	35.9	11.0	0.34
M62	48.8	12.2	0.69
Averaged dimensions	**35.0**	**13.1**	**0.52**

One of the dominant salt marsh vegetation species in the Galveston Bay shoreline as illustrated in Figure 27, is the *Spartina alterniflora* (smooth cordgrass). The natural density of stems is about 300 stems/m^2 and the average stem height and diameter are 1 m and 0.64 m respectively from a study by Minello et al. (2000). The vegetation field in the experimental model was represented by staggered cylinder arrays secured on the flat top disks of the marsh mounds.

Hence, the physical model was represented by three identical circular marsh segments representing restored marsh from the Dalehite Cove. These three segments were constructed in the three-dimensional wave basin at the Haynes Coastal Engineering Laboratory, aligned in the alongshore direction, i.e. parallel to the wave maker. This particular setup allows to have a periodic arrangement of the marsh segments with evenly spaced channel.

Fig. 27. Salt marsh composed of *Spartina alterniflora* plant in the Galveston Bay (http://www.tamug.edu/marb/armitage/photos.htm).

1. Scaling Parameters

Three criteria were used to determine a compromise between the real field dimensions of marsh mounds, the hydrodynamic process involved, the facilities used for the experiment, and to generate the desired model. These three parameters are: the Froude number, Fr, the Reynold number, Re, and the Population Density coefficient, ad.

For geometric similarity of the flow, an undistorted model (subscript m) has been chosen to maintain the geometric similitude of the prototype (subscript p). Therefore, the scale ratio of lateral dimensions L_i and the one of the vertical dimensions V_i in the model and in the prototype are equal to the constant length scale N_L as shown in equation 3.1:

$$N_L = \frac{L_m}{L_p} = \frac{V_m}{V_p} \tag{3.1}$$

For dynamic similarity, the Froude number defined as the ratio of the speed of the flow to the speed of the waves, is expressed as follows:

$$Fr = \frac{U}{\sqrt{gh}} \tag{3.2}$$

U is defined as the fluid velocity, g is the acceleration due to gravity and h is the water depth. Matching the Froude number in the prototype and in the model, the time scale N_T is obtained as follows:

$$N_T = \sqrt{N_L} \tag{3.3}$$

For this model, the experimental setup is an undistorted Froude model with a length scale ratio of approximately $N_L = 1/6.50$, which correspond to a base mound diameter of 35 m, a top mound diameter of 13.1 m and a mound elevation of 52 cm. The time scale ratio is equal to $N_T = 1/2.55$ and was computed given the capability of the wavemaker, and giving prototype waves of periods 5 s and 8 s.

The artificial vegetation was constructed using rigid wooden dowels. These cylindrical rods were chosen for their shape and rigidity similarity with *Spartina alterniflora* and the impractical use of real plants. To recreate the drag force generated by the circular cylinders of the vegetation field, a Reynolds scaling was used to compute the appropriate dowel diameter, d, using the following formula of the Reynolds number:

$$Re = \frac{Ud}{\nu} \tag{3.4}$$

Knowing the fluid velocity $U = C = \sqrt{gh}$ and the kinematic viscosity of water ν, the diameter of the rods d was computed.

The presence of this vegetation is known to reduce the flow speed thanks to the added drag force generated by this denser but porous region. To reproduce this force on the flow field in the experiment, the stem density n defined by Nepf et al. (2004) was computed matching the Population Density coefficient ad in the prototype and in the model. The latest non-dimensional parameter is related to the following equation of the stems density:

$$n = \frac{a}{d} \tag{3.5}$$

The total frontal area per volume a is defined as the ratio of the frontal area of the plant canopy over the volume occupied by the canopy where d is the diameter of the stems. After calculation, a stem density of 48 stems/m^2 was determined and a staggered arrangement of the dowels was decided implying a constant stem spacing of 14.40 cm. Table 2 shows the model dimension used in the laboratory compared to the prototype dimensions.

To construct the circular vegetation fields, twelve 0.02 m-thick plywood sheets were cut into a half disk shape of 1.01 m radius and put together in pairs to make a full disk. Half of these disks were drilled using hand drills and a lab-scale template of the vegetation field printed by a plotter and providing the location of each dowel on the plywood disk. Figure 28 shows the final configuration of the vegetation for each marsh segment. Cut wooden dowels were then embedded and secured in the drilled holes using Liquid Nails^{TM} to guarantee a constant length of the resulting stems over the whole experiment. The other half of the disks were used to first get a control datasets of the experiment with non vegetated marsh segments. Photos of the vegetated and control model are shown in Figure 29.

2. Haynes Coastal Engineering Laboratory

The laboratory experiments were performed in the three dimensional shallow-water wave basin at the Haynes Coastal Engineering Laboratory at Texas A&M University.

Table 2. Summary of scaled dimension of the model for emergent vegetation case. $N_L = 1/6.50$ and $N_T = 1/2.55$

Parameters	**Experimental Model**	**Prototype (Dalehite Cove)**
Water Depth h	1.54×10^-1 m	1.00 m
Marsh Segment Elevation	8.00×10^-2 m	5.18×10^-1 m
Stem Length	7.51×10^-2 m	4.88×10^-1 m
Marsh Top Diameter	2.02 m	13.10 m
Marsh Bottom Diameter	5.38 m	35.00 m
Wave Period T_1	2.00 s	5.10 s
Wave Period T_2	3.00 s	7.70 s
Phase Velocity $C = \sqrt{gh}$	1.22 m/s	3.13 m/s
Stem diameter d	1.60×10^-2 m	$6.35 \times 10^-3 m$
Stem density n	48 stems/m^2	300 stems/m^2
Kinematic viscosity ν	1.54×10^-1	1.54×10^-1
Reynolds Number Re	19876	19876
Void Fraction ad	1.22×10^-2	1.22×10^-2

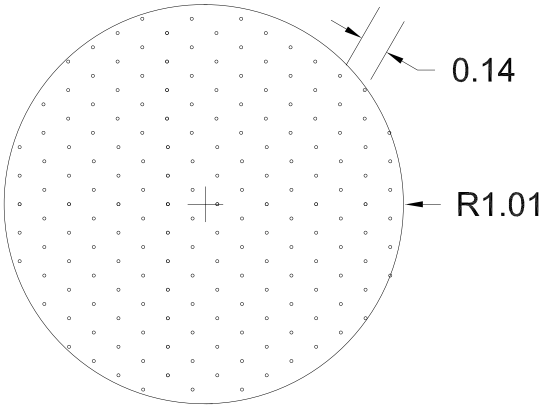

Fig. 28. Vegetation staggered array pattern.

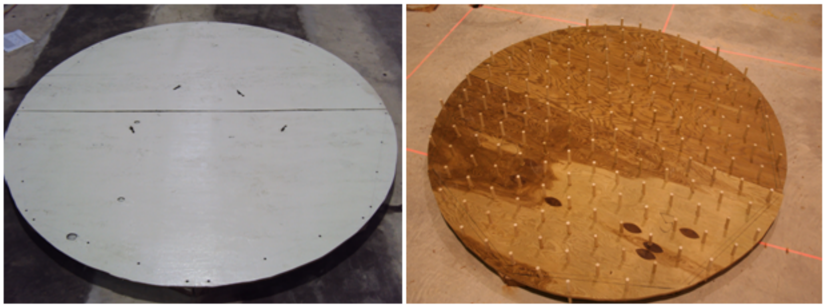

Fig. 29. Non vegetated and vegetated marsh segment models.

The internal dimensions of the wave basin are 22.9 m in width, 36.6 m in length and 1.5 m in height. It is equipped with a wave generator composed of 42 segmented piston type wave maker with directional capabilities able to produce wave periods between 0.5 s and 5.0 s. In order to have a fixed reference coordinate system to locate all the sensors and the model characteristics from the same origin, an arbitrary coordinate system has been defined and is given in Figure 30 where the wavemaker is located at $x = 0$ m. A steep (1:5) rock beach is located on the opposite side of

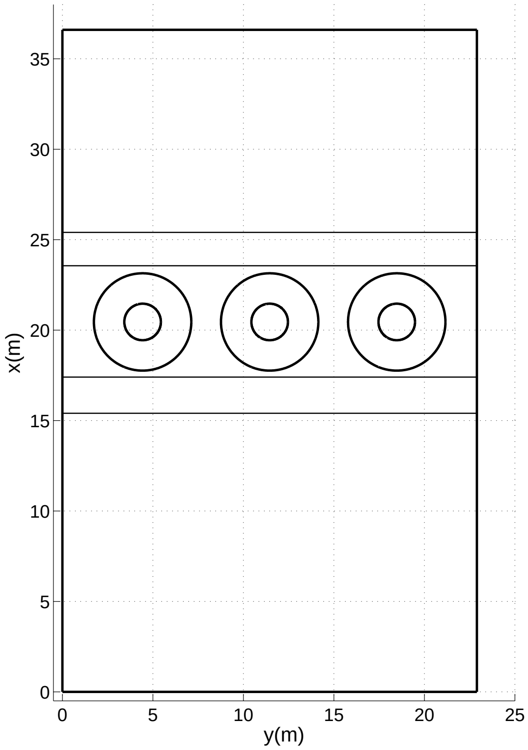

Fig. 30. Experimental basin and coordinate system.

the basin, at approximately 25 m from the wave maker to absorb wave energy. The wave basin is overtopped by a motorized bridge used as an instrumentation platform (Texas A&M University, 2004). The instrumentation setup consists of 19 capacitance wave gauges to measure free surface elevations and 5 five three-dimensional Acoustic Doppler Velocimeters to measure flow particle velocity; the data acquisition system will be described in more details in Section C.

Three identical artificial marsh mounds were constructed inside the basin using sand overlaid by a relatively thick layer of concrete to mold the conical shape of the marsh segment as shown in Figure 31. The base disk diameter of the mounds was

Fig. 31. Molding of the artificial mound.

5.38 m, the top disk diameter was 2.02 m and the height of the marsh segment was 0.08 m. A top view and side view of the mound model is sketched in Figure 32. The horizontal dimensions of the mounds are set to scale but the vertical, especially the height of the mounds, is exaggerated in the figure due to the flatness of the model compared to the diameter of the mound.

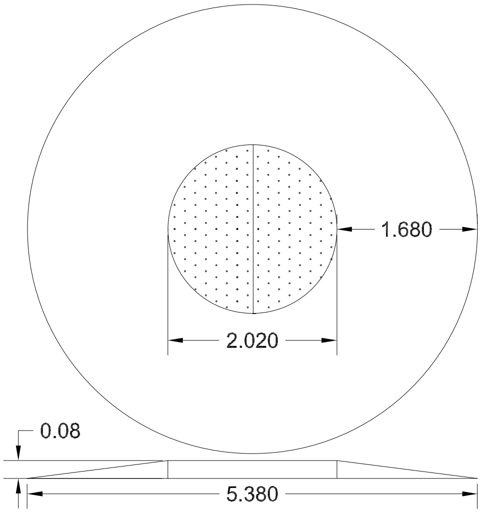

Fig. 32. Top view and side view of the artificial marsh mound.

The three structures were lying on an artificial platform with horizontal dimensions of 6.1 m cross-shore and 22.9 m alongshore made of 20.3 cm height concrete blocks to overcome the minimum water depth limitation of the wave basin. Indeed, the marsh segment model being only 8 cm in height, the water depth would have had to be very shallow and the experimental design required the wave to break on the seaward side of the mound, which would not have been realizable in such shallow water depth. The finalized experimental setup is shown in Figure 33. When control measurements for all the wave conditions with the unvegetated mounds were finished, the circular plywood plates were removed and replaced by the vegetated plates keeping the concrete structure in shape. For the waves to transit from the deep water part

Fig. 33. Finalized experimental setup.

of the basin to the platform, a 2 m long ramp with a slope of 1:10 was constructed in the front part of the platform using sand and concrete. The space between the end of the solid platform and the rock beach was filled with clay and sand to the same level as the platform. A side view of the physical model setup is shown below in Figure 34. To offset the uplift force created on the mounds while immersed in the water, each structure was secured to the concrete platform using rebars, screw hooks, and black annealed rebar tie wire.

Taking into account the maximum capability of the wave basin, three spacings between the marsh mounds were selected to assess the influence of the spacial variability in wetlands on wave hydrodynamics. The different edge-to-edge spacings between two vegetation fields were: 3.46 m, 5.00 m and 6.64 m. Figure 35 shows these different configurations. In each setup, the middle marsh mound was centered in the along-

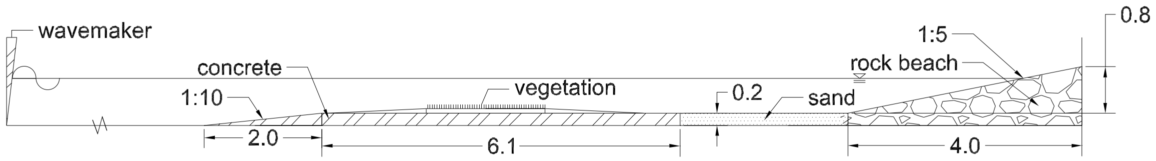

Fig. 34. Side view of the Haynes Coastal Engineering Laboratory physical model setup.

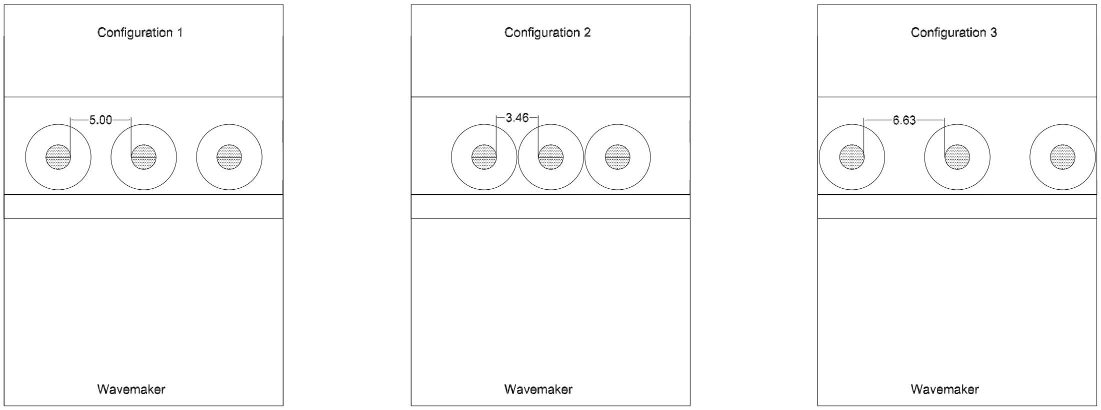

Fig. 35. Top view of the three marsh segments spacings tested in the three-dimensional basin.

shore direction of the tank in order to insure that the sidewalls were located along lines of symmetry. This particular marsh segment lasted for the whole experiment, in contrast to the left and right mounds that were broken down and rebuilt from one configuration to another. Considering the wavemaker located at $x = 0$ m as in Figure 30, the centers of the vegetation field disks were located at $x = 26.3$ m.

3. Wave Conditions

In the laboratory, normally incident waves were generated in six different wave conditions including three different water depths with selected wave periods T of 2.0 s and 3.0 s characteristic of swells. Water depth h was determined to have one near-emergent vegetation condition and two submergent vegetation conditions. The selected water depths at the wavemaker, H_{wm}, were 35.7 cm and 50.3 cm which correspond to 7.4 cm and 22.0 cm in the vegetation field. A deeper water depth of 65.3 cm at the wavemaker was tested only for the intermediate marsh spacing configuration (5.00 m) corresponding to 37.0 cm in the vegetation field.

To allow the waves to shoal on the ramp and break halfway on the front conical part of the marsh before entering the vegetation field, the conservation of energy equation (3.6) from linear wave theory was used along with the McCowan criteria ($H_b = 0.78h_b$, where the index "b" stands for breaking) to compute the input wave heights at the wavemaker for each wave conditions (Dean and Dalrymple 1984):

$$H_2 = H_1\sqrt{\frac{C_{g1}}{C_{g2}}}\sqrt{\frac{b_1}{b_2}} \tag{3.6}$$

In this case, the wave heights correspond to $H_2 = H_{wm}$ and $H_1 = H_b$. C_{gi} is the group velocity and the refraction coefficient $K_r = (b_1/b_2)^{1/2}$ is assumed to be equal to 1 for simplification. A summary of wave conditions is provided below in Table 3. Unfortunately, the failure of the wavemaker as well as multiple gauges during this

Table 3. Summary of the different wave conditions used at the Haynes Coastal Engineering Laboratory.

T (s)	h (cm)	H_{wm} (cm)
2.0	35.7	6.2
	50.3	17.0
	65.3	28.5
3.0	35.7	7.2
	50.3	20.2
	65.3	28.5

extreme case prevented the continuation of the experiment using this wave condition case. Therefore, a total of 28 experimental cases were tested and are summarized in Table 4.

Table 4.: Summary of the 28 wave conditions.

Param. / Test	L_{seg} (m)	T (s)	h_{wm} (cm)	$\mathbf{H}_{wm}$ (cm)	(w/) or (w/o) veg.
01	5.00	2.0	65.3	28.5	w/o
02	5.00	2.0	65.3	28.5	w/
03	5.00	2.0	50.3	17.0	w/o
04	5.00	2.0	50.3	17.0	w/
05	5.00	2.0	35.7	6.2	w/o
06	5.00	2.0	35.7	6.2	w/
07	5.00	3.0	65.3	28.5	w/o
08	5.00	3.0	65.3	28.5	w/

Table 4 – Continued

Param. Test	L_{seg} (m)	T (s)	h_{wm} (cm)	$\mathbf{H}_{wm}$ (cm)	(w/) or (w/o) veg.
09	5.00	3.0	50.3	20.2	w/o
10	5.00	3.0	50.3	20.2	w/
11	5.00	3.0	35.7	7.2	w/o
12	5.00	3.0	35.7	7.2	w/
13	3.46	2.0	50.3	17.0	w/o
14	3.46	2.0	50.3	17.0	w/
15	3.46	2.0	35.7	6.2	w/o
16	3.46	2.0	35.7	6.2	w/
17	3.46	3.0	50.3	20.2	w/o
18	3.46	3.0	50.3	20.2	w/
19	3.46	3.0	35.7	7.2	w/o
20	3.46	3.0	35.7	7.2	w/
21	6.64	2.0	50.3	17.0	w/o
22	6.64	2.0	50.3	17.0	w/
23	6.64	2.0	35.7	6.2	w/o
24	6.64	2.0	35.7	6.2	w/
25	6.64	3.0	50.3	20.2	w/o
26	6.64	3.0	50.3	20.2	w/
27	6.64	3.0	35.7	7.2	w/o
28	6.64	3.0	35.7	7.2	w/

C. Instruments and Data Acquisition

Nineteen capacitance wave gauges were used to measure time series of water surface elevation for each wetland configuration. Within those 19 capacitance wave gauges, eight wireless gauges were provided by the Haynes Coastal Engineering Laboratory and 11 wired gauges were borrowed from the Offshore Technology Research Center (OTRC). The sensor of the capacitance wave gauge consisted of a white wire held tight by a metallic supporting rod. A coaxial cable connects the gauge to a transducer box. These gauges were calibrated to have a linear response output voltage to the water level at the gauge wire. They were calibrated at every change of wave conditions and wetland configuration, whenever the gauges were rearranged. The eight wireless gauges were mounted on a vertically mobile horizontal bar and were calibrated using the LabVIEW Multiple Channel Data Acquisition System, and the same procedure was applied to the 11 wired gauges. The wave gauges were vertically raised and lowered in known incremental distances relative to the still water level recording automatically the gauges output at each position to fit a linear curve between the water elevation and the voltage. For the wireless gauges, prior charging of the batteries was necessary for full efficiency during each test, whereas the OTRC gauges were wired into a data acquisition board on the bridge.

Five three-dimensional Acoustic Doppler Velocimeters (ADV) were used to obtain time series of horizontal and vertical flow motion. Of these five ADVs, four Nortek Vectrino ADVs were used including three down-looking and one side-looking. The fifth sensor was a down-looking Sontek 10-MHz ADV. For each set of measurements, the ADVs were placed at depth of about 60% of the water depth at the ADV location. No calibration is needed for the ADVs. A mounting system was designed to allow them to be mounted and secured on a steel bar and the orientation of the x-axis in the cross-shore direction was determined and adjusted by “eye”. The 19 gauges and the 5 ADVs were recording data at the same time. The mounting system will be described in Section D. Three-axis velocity time series were collected using Nortek’s Vectrino Plus program converting the data to ASCII for the Nortek ADVs and for the Sontek ADV, the time series issued by the acquisition program Horizon were processed by the Win-ADV program converting the binary file to an ASCII file. All the instruments were wired so that data acquisition begins at the same time, triggered by the wavemaker. For all experimental runs, sampling frequency was set to 25 Hz for 600 s for all sensors, to ensure reaching and recording of the steady state part for each test.

Every test case was recorded once using two video cameras, the first one located on the bridge and the second one on the side of the basin. The videos were then converted to MPG files. A sketch of the layout of the wave basin and the video camera positions is displayed in Figure 36. During the experiment, the setting of the zero-mean water level was done before each run. The wired wave gauges offset was adjusted to be “0.00” volt. However, the precision of the procedure was arduous to control due to the mechanical sensitivity of the switch. The zero voltage of the wireless wave gauges was adjusted using LabVIEW. During wave generation, 15000 data points were collected by each sensor. A typical experimental run consisted of the following:

- Move the mechanical bridge holding the steel structure with the instrumentation to its target position.
- Check that the sensors do not touch the ground while moving the bridge. Adjust the elevation of the instrumentation if necessary.
- Make sure they are properly oriented.

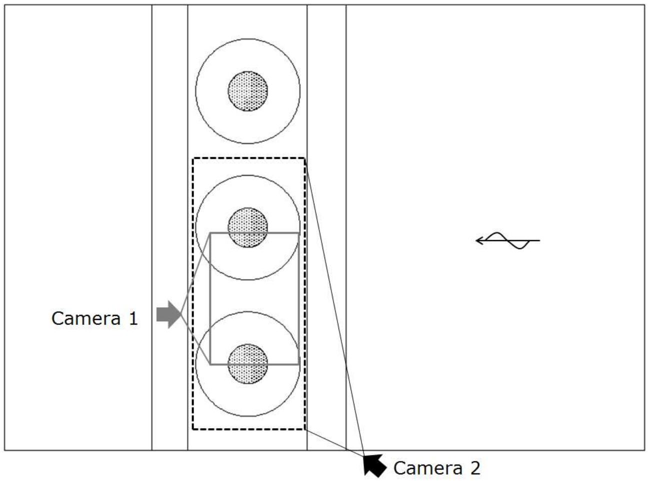

Fig. 36. Camera configuration and fields of view.

- Check and change the batteries of the wireless wave gauges if needed.
- Adjust the zero-offset for the wave gauges.
- Wait for the basin oscillations to settle down.
- Start wave generation and data acquisition for all sensors.
- After each run (10 minutes, 600 s), wait for the waves to dissipate.
- Return to step 1.

D. Instrumentation Setup

As the experimental work proceeded, the measuring location map has been tested and modified few times for all the sensors, before getting an adequate plan to highlight the interesting features of the nearshore circulation system. All the tests contain the same number of sensors and the spacing between them follows a rule of proportionality with respect to the spacing between the islands.

1. Experimental Procedure

All tests contain a extensive map of the wave heights and three-axis velocity for good resolution. A steel structure was built and attached to the motorized bridge using C-clamps. The mobility of the bridge allowed cross-shore translation of the steel structure along the wave basin and above the designed wetland model. The elevation of the structure to the water level was adjustable and changed for each water depth tested. A different elevation was defined for each water depth. Elevation or lowering of the whole structure was completed before each raise or reduction of the water depth respectively. Each dataset was collected by translating the bridge through 11 different positions covering the area of interest, along the marsh fringe. A photo of the resulting overall holding structure is shown below in Figure 37. The elevation of each instrument was adjusted with respect to change in water depth and according to the bathymetry profile of the basin. For each test, a reference gauge was taking measurement in the offshore part of the basin, in front of the ramp, while the other 18 gauges and 5 ADVs were mounted on the 4 steel bars following the layout described below in Figure 38. Among those 4 steel bars, 3 of them held the 18 wave gauges and the last bar held the 5 ADVs, resulting in 3 rows of wave gauges and 1 individual row of ADVs. Figure 39 shows the resulting model setup for the instrumentation.

2. Measurement Locations

In order to generate a map of water surface elevation and 3-D point velocity with a dense spacial resolution, the tests had to be repeated numerous times for a given set of experimental conditions. Repeatability of the experimental conditions were tested

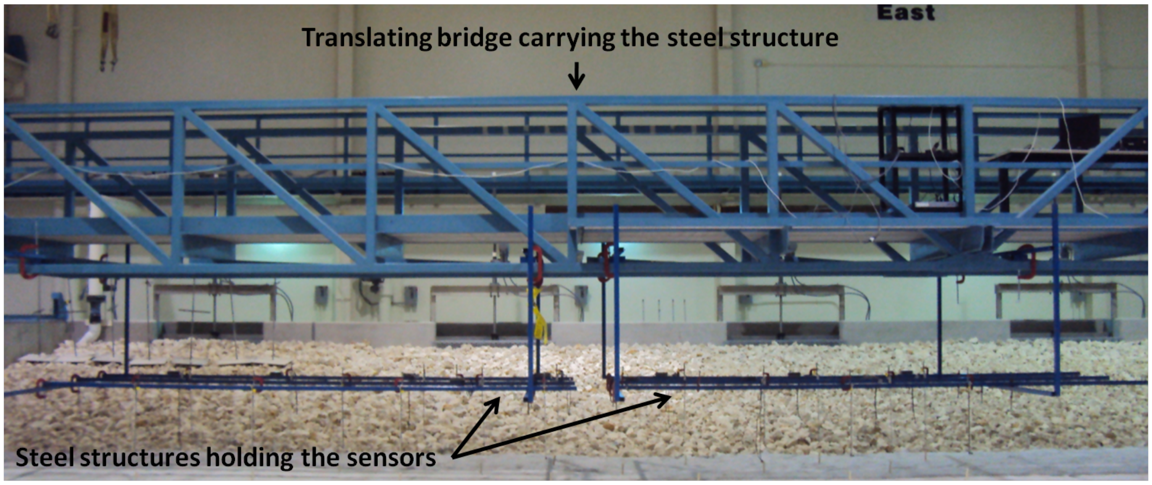

Fig. 37. Front view of the steel structure holding the instrumentation and carried by the bridge.

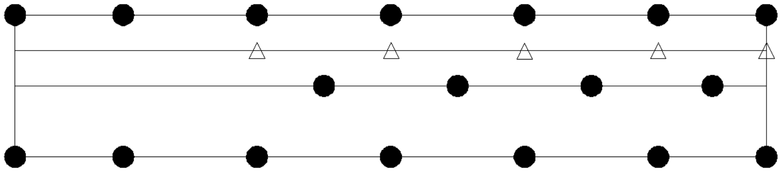

Fig. 38. Top view of the general layout of the wave gauges (•) and ADVs (△) on the steel structure (—).

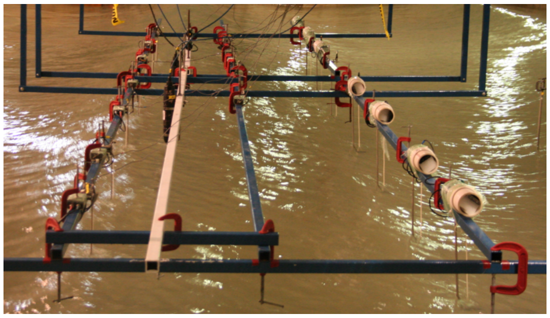

Fig. 39. Final instrumentation setup.

before starting any data acquisition by running given sets of wave conditions several times and a statistical analysis of the repeated measurements is provided in Section 3. The total number of wave gauges being much more important than the number of ADVs, it was possible to repeat some wave measurements at the same location in the basin under the same wave forcing, providing a reproduction of the given wave gauges time series. Spatial errors due to the inexact positioning of the different sensors was assumed to be a systematic error and that may have had the most significant effect on the repeatability of the measurements. Each test case was established to last 10 minutes accounting for a 2 to 3 minute time for the waves to get settled resulting in a 7-8 minute dataset of the steady state to get a minimum of 100 wavelengths per experiment. Data were only collected in half of the total width of the basin, accounting for the symmetry of the wetland configurations. The locations of the wave gauges and the ADVs for the different marsh segment spacings, L_{seg}, are shown in Figure 40, 41, and 42. These instrumentation arrangements allowed to collect wave surface elevation at 170 different locations as well as 3-D point velocity measurement at 55 different locations for each wetland configuration. The wave gauge measurements are spatially distributed on a non-uniform grid whereas the ADV sampling locations are distributed on a regular grid. Moving the instrumentation structure from one bridge location to another could result in an overlap of one row of gauges with the prior location of another row. This occurred four separate times, producing repeated measured dataset for 28 wave gauges. However, it is important to notice that with these it was always a row of wireless wave gauge that overlapped with a row of wireless wave gauges. Indeed, possible differences in measurements may occur due to the difference in type of the wave gauges. This instrumentation planning allowed verification of similarity and coherence of the data for the repeated measurements and to replace bad datasets. A greater resolution in the middle part of the instrumentation arrays allowed the emphasis of the the hydrodynamic process occurring in the marsh fringe and in the vegetation field.

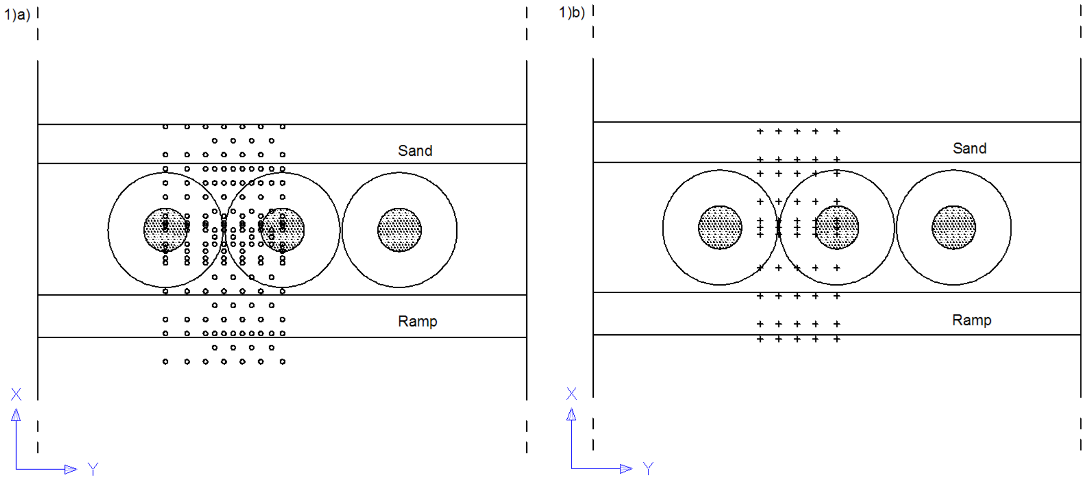

Fig. 40. Sampling locations of (○) wave gauges and (+) ADVs for $L_{seg} = 3.46$ m in the experimental setup.

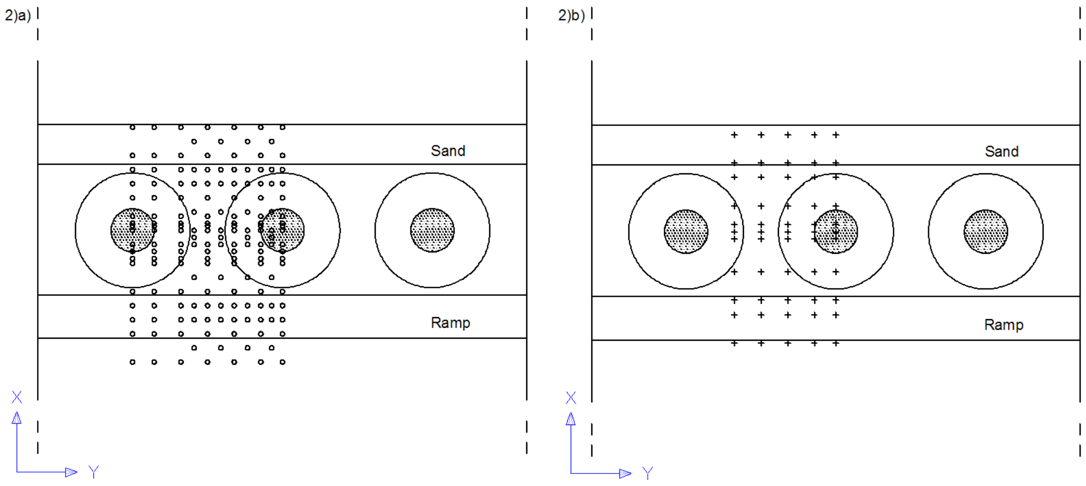

Fig. 41. Sampling locations of (○) wave gauges and (+) ADVs for $L_{seg} = 5.00$ m in the experimental setup.

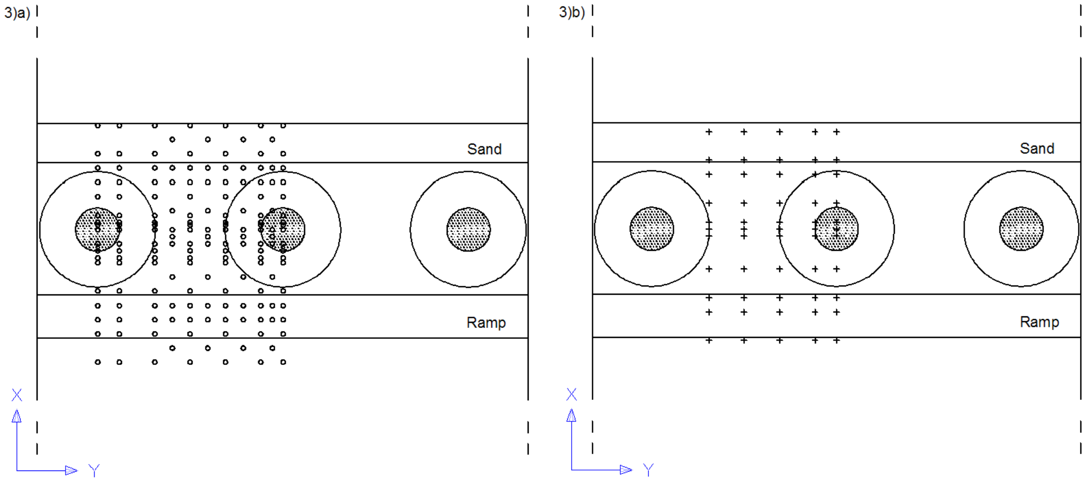

Fig. 42. Sampling locations of (○) wave gauges and (+) ADVs for $L_{seg} = 6.64$ m in the experimental setup.

E. Test Name Codes and Data Format

Accounting for the large amount of tests run for this project as well as the complex instrumentation setup, categorization, labeling and numbering of wave condition, wetland configuration and instrumentation is needed. List of code names is referenced in the following sections.

1. List of Tests Run

A simple 3-digits code name has been created to designate a particular wetland configuration, vegetated or unvegetated marshes, wave period and wave conditions characterizing one given test case. The first digit corresponds to the wetland configuration and it is numbered from 1 to 3. The second digit describes the vegetated or unvegetated state of the marshes and takes the value 0 or 5. Finally, for the last digit, two characteristics of the number is to take into account: the parity of the number and its value. The parity gives the corresponding wave period whereas the number gives the wave conditions including waveheight and water depth at the wavemaker for this test case. The value of the last digit ranges from 1 to 6. The following Table 5 summarizes the code name with their caption and the list of all the experimental conditions tested is given in Table 6:

Table 5. Summary of test case numbering code.

1^{st} digit			2^{nd} digit		3^{rd} digit					
1	2	3	0	5	1	3	5	2	4	6
5.00 m	3.46 m	6.64 m	U	V	2-D	2-I	2-S	3-D	3-I	3-S

where:

U	Unvegetated
V	Vegetated
D	Deep
I	Intermediate
S	Shallow
2	T = 2.0 s
3	T = 3.0 s

Table 6. Summary of tests run.

100 Series		200 Series		300 Series	
101	151	X	X	X	X
102	152	X	X	X	X
103	153	203	253	303	353
104	154	204	254	304	354
105	155	205	255	305	355
106	156	206	256	306	356

For simplicity, configurations 1, 2 and 3, in Figure 35, corresponding to 5.00 m, 3.46 m and 6.64 m spacings will be denoted 100 Series, 200 Series and 300 Series respectively and test case will be recall by their numerical denomination in the following chapters of this thesis.

2. Instrumentation Numbering

During the whole experiment, each wave gauge and each ADV was given a number and this number was the identity of the instrument for the entire project. The reference wave gauge in the offshore part of the basin was numbered gauge 19. The numbering of the other instrument is described in the sketch given in Figure 43 where the wave gauges are listed from 1 to 18 and the ADVs are listed from A to E. The instrumentation was carried by a bridge in the wave basin where each instrument had a fixed position with respect to the bridge and according to the wetland configuration. Translation of the structure enabled eleven bridge positions creating an irregular grid covering the marsh fringe area of interest. Each position will be known as a station, numbered in ascending order from 1 to 11 starting at the beach side of the basin to the offshore part as displayed in Figure 44. A complete set of stations for each wetland configuration is given in the Appendix E. A proportionality rule was applied to change the spacing between the sensors in accordance with the spacing between the islands. Therefore, a cross-shore raw of wage gauges and ADVs was always aligned with the

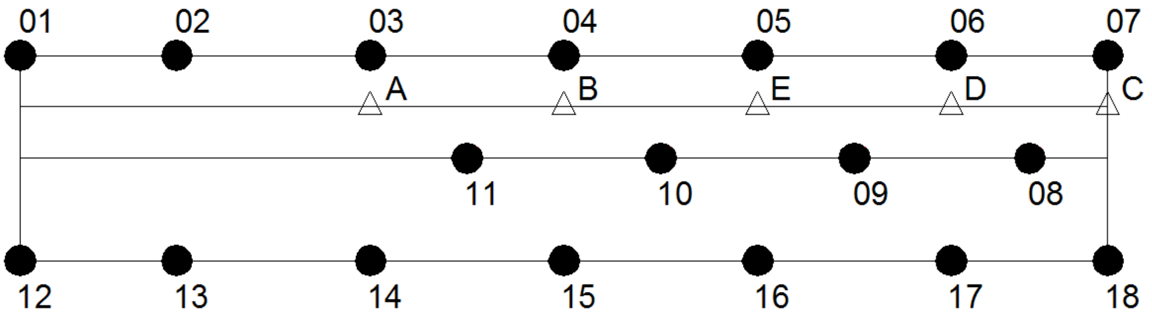

Fig. 43. Numbering of the instrumentation: wave gauge (●) and ADVs (△).

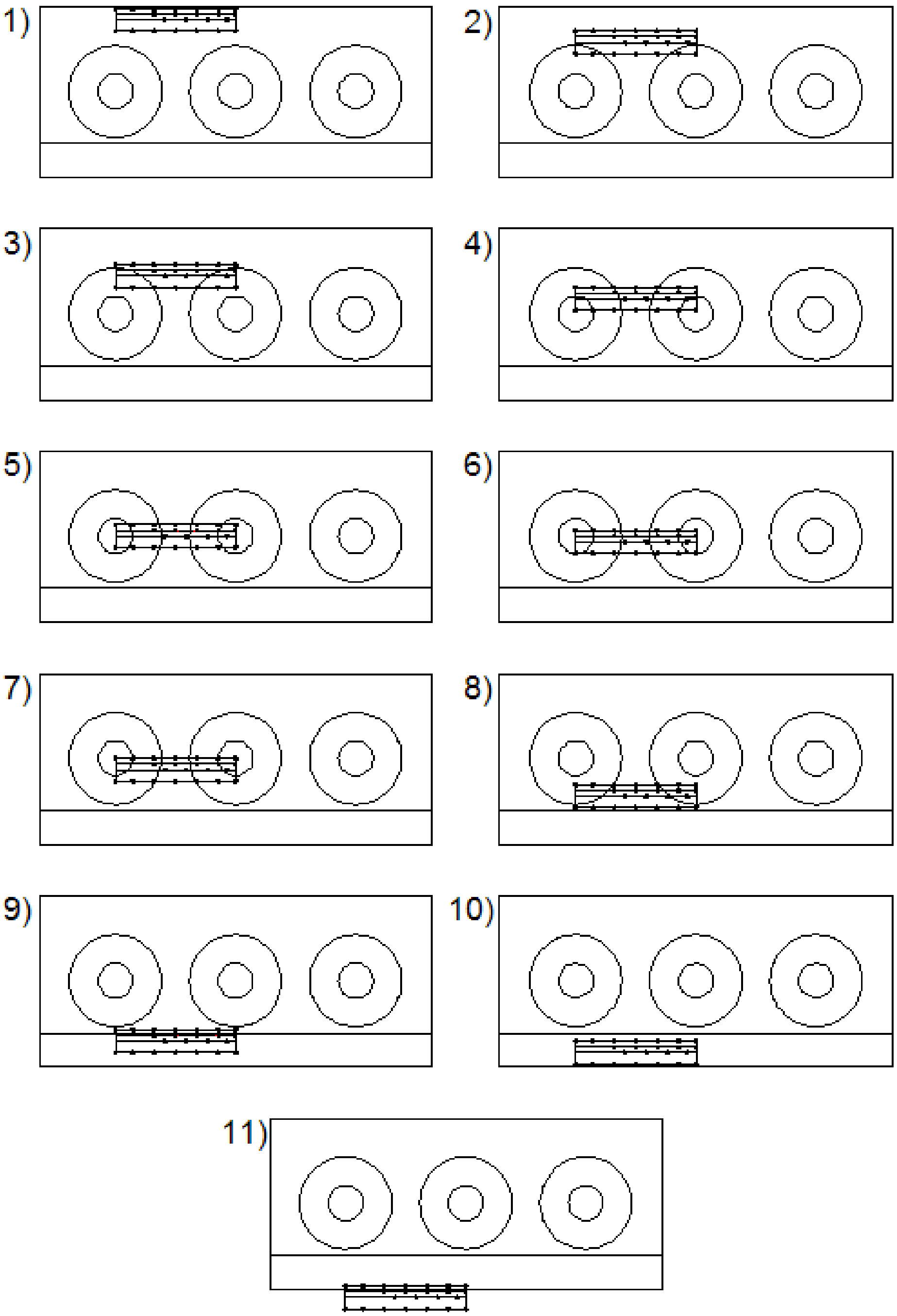

Fig. 44. Layout of the different bridge positions from station 1 to 11 for a 5.00 m spacing between the vegetation fields.

centerline of the basin and the other end of the instrumentation grid was composed of only wave gauges aligned with the cross-shore centerline of the left island. Indeed, ADV measurements were concentrated in the channel.

F. Digital Archives

The present section will provide the necessary information regarding the formats used for data archiving. The raw data from each of the 28 experiments has been sorted into separated folders and stored into a compact disc. Six folders separates the six series: 100, 150, 200, 250, 300 and 350. Within each of these folders, the files are then sorted by water depth. Therefore, series 100 contains three folders for the three water depth tested. 101 and 102 correspond to the same deep water depth. 103 and 104 correspond to the intermediate water depth. 105 and 106 correspond to the shallow water depth, and so forth. Inside this last folder, two folder have been created to separate the wave gauges and the ADVs data. Within the wave gauges folder, the naming convention for the individual data files is given by the following:

- **WG_H[n]T[n][V or no V]_[st].dat**
- **ADV1_H[n]T[n][V or no V]_[st].[datatype].txt**
- **adv2_h[n]h[n]_[st]0001.Vu**

Here, "**WG**" stands for wave gauge. "**ADV1**" refers to the Nortek ADVs and "**adv2**" refers to the Sontek ADV. It is to remember that four Nortek ADVs were used along with only one Sontek ADV. For example, the velocity data from test 103 for the Nortek ADVs at station 5 are found in **ADV1_H3T3_05.vel.txt**. The corresponding Sontek ADV data are in **adv2_h3t3_050001.Vu**, and the wave gauges data are in **WG_H3T3_05.dat**. Notice that the "**n**" corresponds to the last digit in the test name code. To differentiate case 103 to 153 where the vegetation patches are added in the experimental setup, the letter "**V**" is added in the name as for example **WG_H3T3V_05.dat**.

The file **WG_H3T3_05.dat** contains a 15000 rows by 20 columns matrix. These are the time series of the water surface elevation from each of the 19 wave gauges, measured in meters. The first column corresponds to the time t and starts at $t = 0$ s. The second column is the gauge 1, the second is gauge 2, and so forth, as numbered in Figure 43. The measuring locations for these wave gauges are referenced in Appendix A. The twentieth column is gauge 19 which corresponds to the offshore wave gauge.

The file **ADV1_H3T3_05.vel.txt** contains 8 column of data, each of which are 60000 rows long. Indeed, ADV A, B, C and D are stored within these rows and identified by their probe number as listed in Table 7.

Table 7. Lists of ADVs and corresponding probes.

ADV	Probe
A	0
B	1
C	2
D	3

The format of the file is [Probe Sample Time Event_Counter X Y Z W], and the matrix is sorted with respect to the the "Sample" column. Therefore, a sorted routine written in MATLAB was used to separate the ADV data for each probe. The three coordinates of the velocity vectors are given by X, Y and Z and W is a redundant of

Z. For the Nortek ADV, velocity [**vel**], amplitude [**amp**], signal-to-noise ratio [**snr**] and correlation coefficients [**cor**] are separated into 4 files and define the [**datatype**] in the file name. Whereas for the Sontek ADV, all these parameters are contained in one single file. All velocities are recorded in cm/s.

Attention is required as for the labeling X, Y and Z of the column in the matrix which do not necessary correspond to the velocity components U, V and W. Table 8 summarizes the correspondence between the column label and the velocity coordinate it corresponds to.

Table 8. Lists of ADVs and corresponding velocity component.

ADV	X	Y	Z
A	U	-V	-W
B	U	-V	-W
E	V	-U	W
D	U	W	V
C	U	-V	-W

G. Data Processing

1. Pre-processing

Prior truncating of all datasets was performed deleting between 250 s and 310 s of the raw time series, which result in ranges from the first 6250 to the first 7750 points to remove the startup effects. These ranges were determined using the datasets for each test case of the gauges located in the very shoreward end of the basin where the steady state was reached at last. The list of truncated section is given in Appendix B. The stabilized trend was defined using both plot of time series of water surface elevation and estimation done while running the experiment. The amount of cell deletion was then applied to the 19 wave gauges and the 5 ADVs belonging to the given test case for every bridge location so that each time series outputted was of the same length.

The truncated datasets of both capacitance wave gauges and ADVs were filtered using the despiking MATLAB subroutine written by Nobuhito Mori. The MATLAB code applies the phase-space thresholding method that Goring and Nikora (2002) developed and allows the detection of spikes and their replacement. The subroutine is available in the free MACE toolbox for coastal engineers (http://www.oceanwave.jp/). Data points identified as spikes are then replaced using a cubic interpolation. Most time series were despiked only once to remove the major spikes but also to prevent the removing and replacement of natural fluctuation in the velocity and water elevation measurements by interpolated points. However, additional despiking were performed for a selected datasets where significant spike noise remained. All time series were detrended by removing the mean value over the truncated datasets. A comparison between raw and pre-processed time series is shown below in Figure 45. The mean value has been reevaluated due to the lack of accuracy in setting the zero voltage value at the beginning of each run and is explained in Chapter IV, Section 1.

2. Data Filtering and Quality

A total of approximately 700 time series were collected by the end of the experiments. In order to remove bad quality time series to ensure no distortion of the results in the data analysis, three categories of damaged time series have been identified for the wave gauges time series:

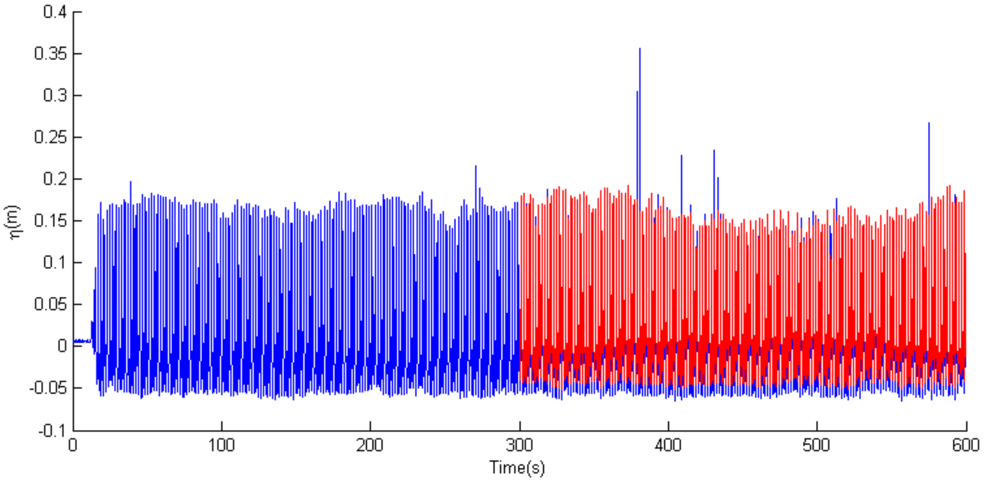

Fig. 45. Raw data (blue) and resulting pre-processed portion (red) of measured time series.

- shifted: large dispersion of the mean from its expected value.
- lost data: no record of the data.
- over-spiked data.
- inconsistent measurements: the measured value are of the order of millimeters.

An example of categorized shifted measurement is shown in Figure 46. Those data have been decomposed into regular interval of 10 s realizations following one another. For each realization the mean of the interval was computed and plot against the same decomposition for neighboring wave gauges as shown in Figure 47. Shifted data where the large dispersion from the mean occurs within the 100 wave cycles were discarded whereas shifted data where the large dispersion from the mean occurs after the 100^{th} wave cycles were cut and kept for the analysis. Due to malfunctioning of a few of the

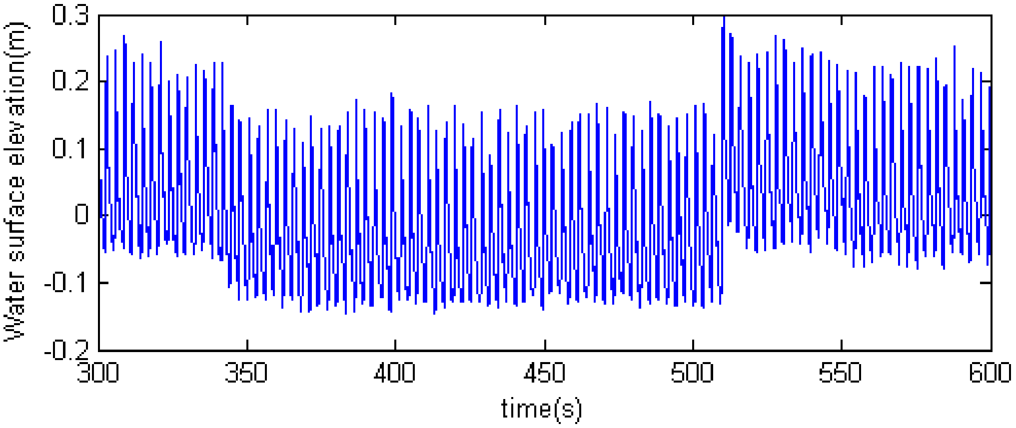

Fig. 46. Shifted measurement.

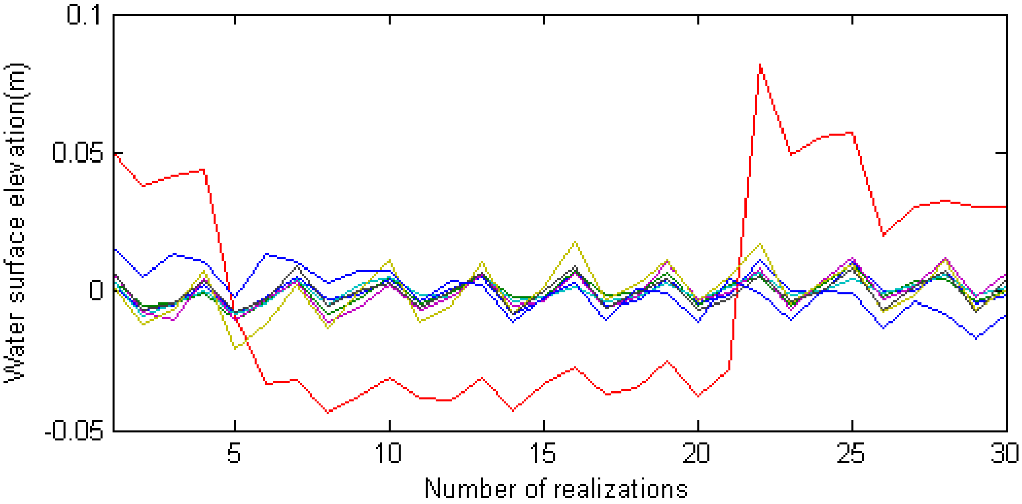

Fig. 47. Comparison between mean water surface elevation per realization of shifted data and neighboring measurements.

instruments during some test runs, no data have been recorded for 16 wave gauges on the overall set of the acquired data. The failure of the wave gauge 17 occurred while running the highest wave for the deepest water depth which led to over-spiked time series where no despiking is possible as displayed in Figure 48. The same issue occurred for the wave gauge 14, 15 and 16, however the frequency of concerned cases was much less compared to gauge 17. A summary of the amount of truncation and the list of discarded data are provided in Appendix B. Overall, 2.5% of the time series have been removed from before starting the analysis.

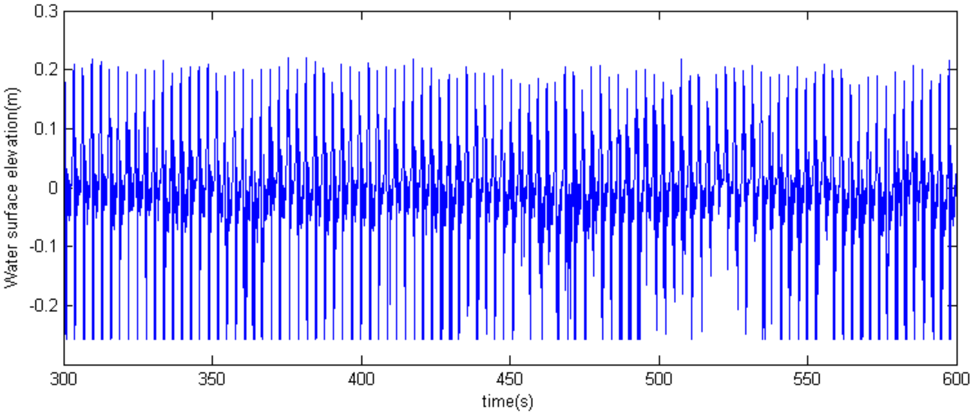

Fig. 48. Example of over-spiked time series.

3. Repeatability of Measurements and Error Evaluation

Given the relatively high value of the spatial resolution provided by the limited number of sensors used in this experiment, each test had to be repeated multiple times for a given wave condition. Therefore, it is important to determine how repeatable the experimental conditions were. For that purpose, a quantitative evaluation of the variability within the same dataset is needed. The offshore wave gauge, gauge 19, is used for this estimation as it remained stationary for a given experimental conditions. Although, in theory, each case 1, 2, 3, 4, 5, and 6 (third digit in the name code) represents a unique wave conditions, series 100, 150, 200, 250, 300, and 250 cannot be used together for a given wave condition to examine the repeatability. Indeed, during the laboratory experiment, given a spacing between the marsh, all the runs for every wave condition and series were completed before switching the next marsh spacing where the same tests were ran and so forth. Also, the transition from vegetated islands to non vegetated islands obligates to drain the wave basin in order to replace the circular plywood sheets on the top of the mound and secure them tightly to prevent the waves from sweeping them away and damaging the instrumentation. For these reasons, the water level in the basin had to be changed at least six times from the deep water case to the shallow water case before changing the wetland configuration. The water level was verified before any data recording using a fixed ruler located behind the wavemaker machinery. The ruler was graduated every 1 mm. Thus, errors in water level measurements might have been made from one test to another. Other sources of experimental error include the spatial errors due to the inexact positioning of the sensors. These errors are estimated to be less than 1 cm.

Tables 9 and 10 list all the repeated measurements made by gauge 19 offshore for $T = 2$ s and $T = 3$ s respectively. The number of realizations is given by n. Included also are the mean wave height, $\bar{H}$, standard deviation of the mean wave height, $\sigma_{\bar{H}}$, the percent variability $\%\ var$, and the standard deviation of the mean water level, σ_{η}. The percent variability is defined by the ratio of the percent variation $\sigma_{\bar{H}}$ and the average value and is a measure of the relative dispersion as shown in Equation 3.7.

$$\%\ var = 100 \times \frac{\sigma_{\bar{H}}}{\bar{H}} \tag{3.7}$$

Table 9. Estimation of the repeatability of the measurements based on the offshore wave gauge for 2 s-waves. n = number of realizations, $\bar{H}$(cm) = mean wave height, $\sigma_{\bar{H}}$(cm) = standard deviation of the mean wave height, % var = percent variability, and σ_η(cm) = standard deviation of the MWL.

n	2 s-wave	$\bar{H}$ (cm)	$\sigma_{\bar{H}=}$ (cm)	% var	σ_η (cm)
11	101	27.24	0.40	1.48	0.15
11	151	28.94	0.44	1.52	0.12
11	103	15.55	0.26	1.70	0.23
11	153	17.48	0.40	2.26	0.11
11	203	16.14	0.20	1.20	0.00
11	253	17.00	0.18	1.06	0.25
11	303	15.61	0.19	1.24	0.11
11	353	17.47	0.21	1.20	0.00
11	105	5.79	0.12	2.02	0.19
11	155	6.06	0.73	12.03	0.00
11	205	6.25	0.21	3.35	0.00
11	255	6.41	0.18	2.81	0.11
10	305	5.58	0.27	4.83	0.59
11	355	6.13	0.28	4.59	0.11
11	106	4.67	0.28	2.95	0.00

Table 10. Estimation of the repeatability of the measurements based on the offshore wave gauge for 3 s-waves. n = number of realizations, $\bar{H}$(cm) = mean wave height, $\sigma_{\bar{H}}$(cm) = standard deviation of the mean wave height, % var = percent variability, and σ_η(cm) = standard deviation of the MWL.

n	3 s-waves	$\bar{H}$ (cm)	$\sigma_{\bar{H}=}$ (cm)	% var	σ_η (cm)
11	102	24.44	0.14	0.56	0.00
11	152	24.66	0.34	13.92	0.00
11	104	13.23	0.06	0.43	0.20
11	154	19.78	0.17	0.85	0.68
11	204	17.44	0.25	1.44	0.16
11	254	18.33	0.32	1.73	0.43
11	304	20.49	0.20	0.97	0.00
11	354	19.22	0.11	0.60	0.19
11	106	4.67	0.28	2.95	0.00
11	156	8.81	0.21	2.37	0.00
11	206	8.50	0.08	0.94	0.11
11	256	8.42	0.10	1.24	0.23
11	306	9.21	0.15	1.63	0.00
11	356	9.96	0.25	2.54	0.14

After the startup effect was removed from all the data (Section 1), the zero-upcrossing method was used on the detrended data to compute the mean wave heights. To compute the mean water surface elevation, the time average over the length of the un-detrended time series were computed. For 3 s-waves, the data shows a relatively small variability during the laboratory experiments. Indeed, the percentage of variability is less than 3% for all the cases except Test 152. However, examination in more detail of the values of the mean wave height of gauge 19 for every station in Test 152 shows good consistency except at station 1. Figure 49 shows that the generated waves at the wavemaker may not have been set up correctly at that station as no deficiency of the wave gauge detectable in the mistaken time series. Regarding the 2 s-waves, the

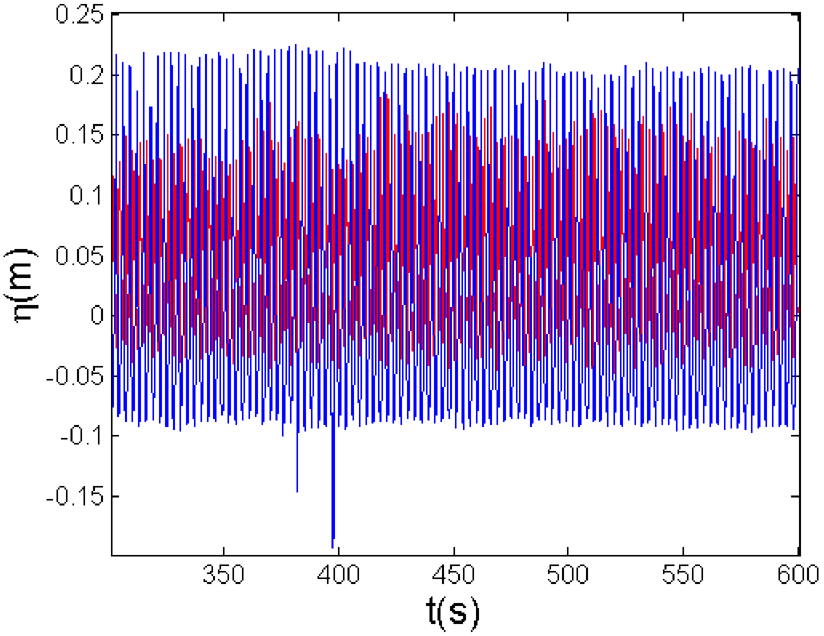

Fig. 49. Time series for gauge 19 of Test 152 at station 1 (red) compared to station 4 (blue).

percentage of variability is under 5% except for Test 155. A close look at the mean wave heights for each station shows good consistency except for station 1 and station 2 where a difference of about 1 to 2 cm inferior than the expected value is noticeable. Overall, the variability of the data remains less than 5% for all the cases but most of these are less than 2%. The standard deviation of the mean water elevation remains very small at the offshore wave gauge with an approximate value of less than 0.7 cm. The variability of these measurements remains small in a reasonable good manner for gauge 19, for both wave height and mean water elevation.

4. Missing Data Interpolation and Extrapolation

Due to the failure of some sensors during the experiments an interpolation method had to be chosen in order to fill up blank spots in contour maps. In order to replace the unrepresentable value denoted as “NaN” (Not-a-Number) appearing in a given contour plot matrix, and overwrite these cells with interpolated values obtained from neighboring entries, a subroutine written by D’Errico (2004) has been used to interpolate and extrapolate NaN elements in a 2D array. The interpolation technique used is based on sparse linear algebra and PDE discretizations, so that the numbers computed to replace the NaNs are approximated from the surrounding values. Different interpolation options are provided. The interpolation method used in this study is a least square approach which does not modify the known values. A before/after interpolation example is given in Figure 50. Regarding the extrapolation, a linear fit has been used. In the following section of this thesis, on all contour plots specifically, a circular marker will refer to interpolated (or extrapolated) data whereas an asterisk marker will refer to experimentally measured data.

There were particular cases where missing data were not interpolated because a complete row of sensors was missing. Three test cases are concerned. The first

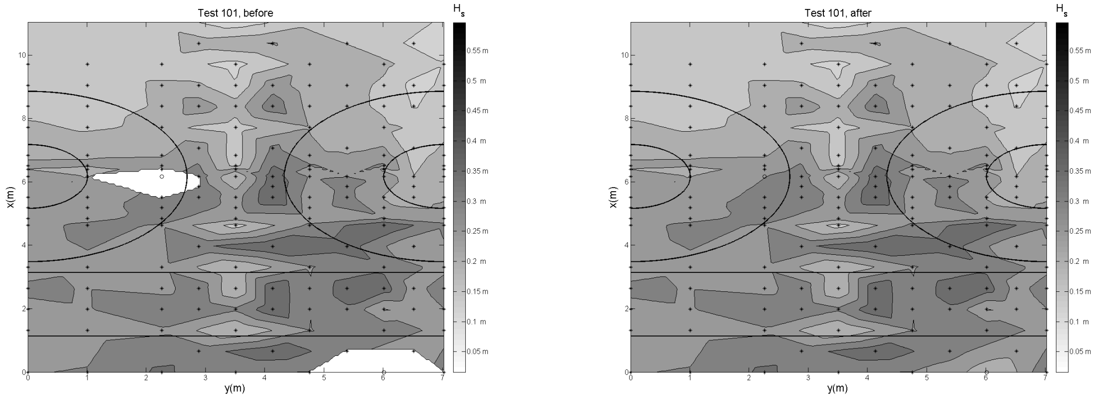

Fig. 50. Before and after interpolation using the subroutine from D'Errico (2004). Interpolated data (○). Measured data ($*$).

one is case 305 where the wave gauges and ADV time series were lost for station 3. Starting case 355 and 356, the Sontek ADV (ADV E) failed in recording any data at the very last stage of the experiment. Hence, no data were collected in the concerned region for all the stations. No interpolation was made due to the significant amount of data point missing and the concentration in a particular region. No analysis of the generated contour plots may be possible as shown in Figure 51.

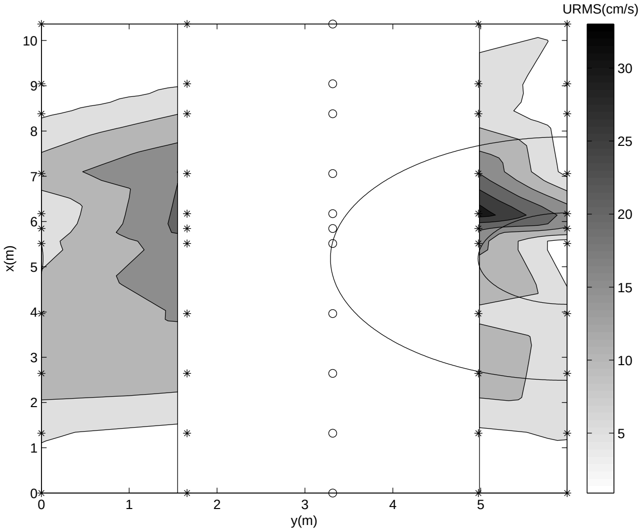

Fig. 51. Example of a resulting contour plot from the velocity data collected during Test 356.

CHAPTER IV

DATA ANALYSIS AND EXPERIMENTAL RESULTS

All tests contain an extensive map of the time-resolved wave heights and three-axis velocity, therefore, it is expected that these measurements will help in determining the characteristics of the nearshore circulation system and in quantifying the driving forces of nearshore circulations (Haller et al. 1997, Haller et al. 2000, Haller and Dalrymple 2001, Haller, Dalrymple and Svendsen 2002).

A. Preliminary Comments

1. Observations during the Experiments

A higher number of data sensors were concentrated in the main channel and on the half left side of the middle island. The fixed coordinate system used is given in Figure 30. This could result in a lack of symmetry with the data sampled on the right half side of the left island.

The normally incident waves propagated along the wave basin, shoaling up on the ramp, and forming a steep plunging breaker as they shoaled again on the sloped marsh mound. Only the wave conditions given by case 6, for the three island configurations, encountered an early slight breaking of the waves while shoaling at the top of the ramp and a second breaking while shoaling on the marsh mounds. Indeed, case 6 corresponds to the smallest waves with the shortest wave frequency generated as described in Table 3. As the waves propagate on the ramp, they shoal while entering the shallow water region. Thus, the ratio of the wave height to the water depth increased rapidly steepening the wave crest and causing the wave to break a first time on the ramp. For all the other cases, the breaking region was restricted within a narrow area (19.5 m $< x <$ 18.5 m). Table 11 summarizes the experimental conditions with their associated test name codes.

Table 11. Experimental conditions. Wave height H_{wm} and water depth h_{wm} measured at the wavemaker. Water depth h_{bed} measured at the toe of the islands.

Test	H_{wm} (cm)	T (s)	h_{wm} (cm)	h_{bed} (cm)
101 and 151	28.5	2.0	65.3	45.0
102 and 152	28.5	3.0	65.3	45.0
103, 153, 203, 253, 303, and 353	17.0	2.0	50.3	30.0
104, 154, 204, 254, 303, and 354	20.2	3.0	50.3	30.0
105, 155, 205, 255, 305, and 355	6.2	2.0	35.7	15.0
106, 156, 206, 253, 306, and 356	7.2	3.0	35.7	15.0

For all tests, as the wave approached the wetland region, a slight phase lag of the crest of the wave in the channel compared to the crest on the mound was noticeable during the experiment allowing the wave to steepen earlier on the mound and break sooner than the part of the waves propagating in the channel as shown in Figure 52. As the waves propagate through the vegetation field, the parts of the wave crest going through this denser region are decelerated by the drag force induced by the stems. Therefore, a positive lag in the propagation of the crest in the vegetation fields was noticeable compared to the parts of the wave crest propagating in the channels.

2. Coordinate System Used for Data Analysis

To analyze contour plots of a given parameter, a local coordinate system is defined with its origin located at the position of the bottom left sensor (wave gauge or ADV)

Fig. 52. Illustration of the lag in the breaking of the waves in the wetland channel during the experiment.

of the instrumentation grid. The input waves are coming from the bottom of the contour map and the rock beach is located at its top. The vertical axis remains the same for all tests whereas the horizontal axis varies from 5.5 m to 8.5 m depending on the spacing between the islands as illustrated in Figures 53, 54, and 55. For the wave gauges, the origin of the reference system is fixed for any wetland configuration. For the ADVs, the origin changes position due to the rule of proportionality used to define the ADV grid.

B. Wave Statistics Analysis

For an adequate description of the water surface in the field of interest, statistical parameters of the water surface have been computed and analyzed to get the characteristics of the water surface under the influence of the variation in bathymetry, the presence or lack of the vegetation stems and the wetlands configuration. Among

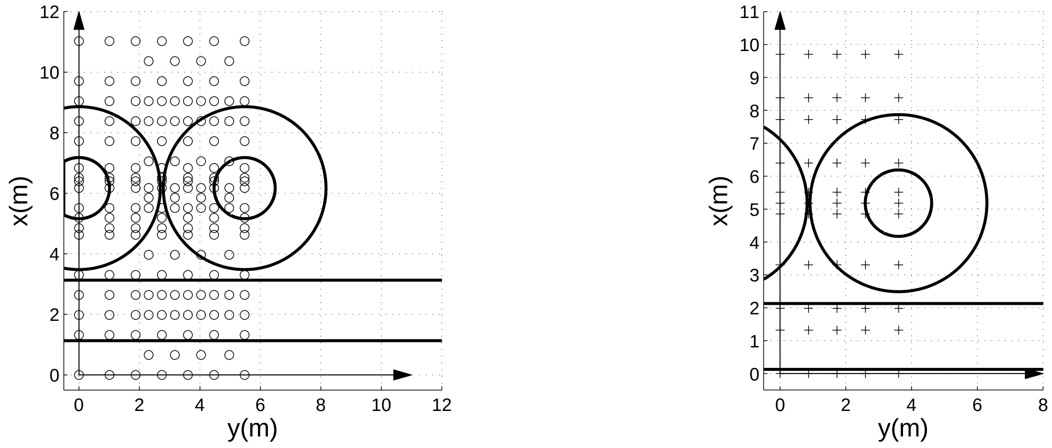

Fig. 53. Local coordinate systems for the (○) wave gauges and (+) ADVs for $L_{seg} = 3.46$ m.

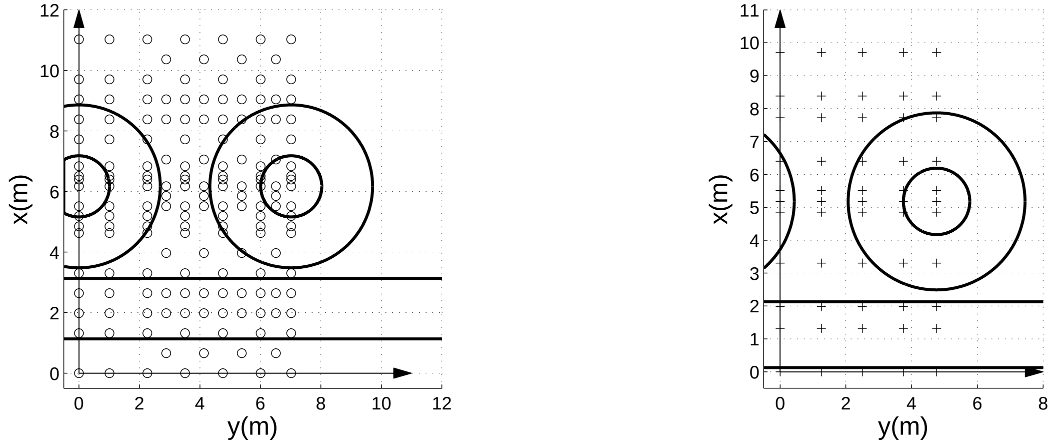

Fig. 54. Local coordinate systems for the (○) wave gauges and (+) ADVs for $L_{seg} = 5.00$ m.

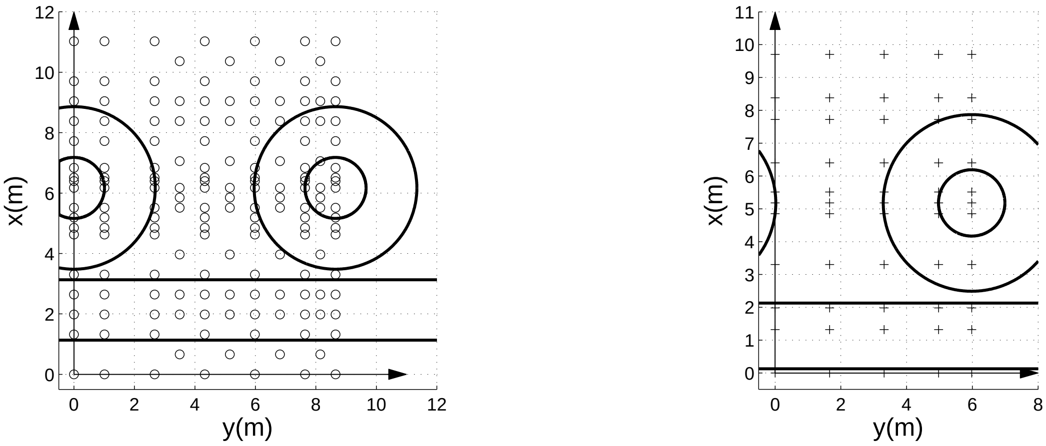

Fig. 55. Local coordinate systems for the ($\circ$) wave gauges and (+) ADVs for $L_{seg} = 6.64$ m.

those, the significant wave height distribution along the marsh fringe was determined as well as the mean water surface elevation.

1. Mean Water Surface Elevation

The grid map of wave gauges contained a total of twenty-eight rows of sensors starting from the offshore region up to the nearshore area, and ending at the toe or the rock beach. This setup allowed the capture of the evolution of both the generated wave fields and mean water levels (MWL) ($\bar{\eta}$). The instrumental setup is described in Chapter III, Section D.

a. Methods

When waves break on a beach, they produce a wave setup, an increase in the MWL above the still-water elevation of the sea. In order to analyze the influence of the presence of wetlands in wave setup and setdown, the mean water surface elevation was computed using the following equation:

$$\bar{\eta} = \frac{1}{N} \sum_{n=0}^{N} \eta(x, y, t + n\tau) \tag{4.1}$$

In equation 4.1, η denotes the truncated and despiked discrete time series at a wave gauge having for coordinates (x, y) in the local coordinate system and τ is the sampling period ($f = 1/\tau = 25$ Hz).

During the experiment, the adjustment of the zero-offset of the wave gauges before each run was precise up to ~ 2 cm. The variation in MWL being very sensitive to small changes, the zero offset had to be readjusted in the time series, prior making any calculation, to obtain a zero water level before the waves arrive. To complete this task, the mean water level offset was computed using the beginning of the acquired data until the first signature of the wave arrived, which represent 175 data points, equivalent to seven seconds in the time series. This range was evaluated using the wave gauge closest to the wavemaker as it is the first sensor to encounter the generated waves. This sensor corresponds to gauge 19 for each station. The mean value of this portion of the signal was computed and subtracted from the whole data series. An example of the correction is given in Figure 56. Series 100 and 150 were the most affected by this offset. In each test, the respective contour maps of mean water surface elevation show good quality of the data after adjustment. In the following sections, the relative variations of the MWL will be analyzed with respect to the still water level thus defined.

b. Results

It is important to recall that under certain conditions of nearshore slope and wave activity, the longshore variation of a rip current system is characterized by broad

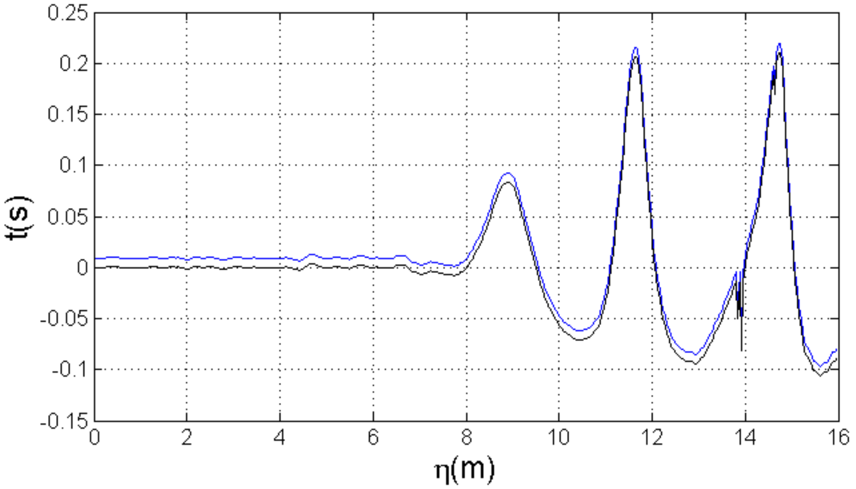

Fig. 56. Original (blue) and corrected (black) time series of gauge 19 for Test 102 at station 11.

regions of wave setup separated by a narrow region of wave setdown. If the offshore directed flow is strong enough in the narrow region, it is then called a rip current. Indeed, the majority of the plots seem to agree on the fact that a wave setdown occurs offshore, upstream of the breaker zone, and wave setup occurs downstream.

In fact, case 4 summarizes adequately the features of cases 3 and 6 with the greatest wave setup nearshore with a value as high as 4 cm in test 154. Figure 57 presents the evolution of the MWL for the three island spacings in case 4, with and without vegetation. The change in spacing between the islands seems to induce this increase in the MWL. The longshore uniformity of the MWL variation after the breaker zone, for $x > 5$ m for a 3.46 m and 6.64 m spacing is distinguishable compared to a 5.00 m spacing (100 and 150 series). However, a greater variability appears in the channel of test 304 and 354, at the breaker zone. Closer islands make the waves

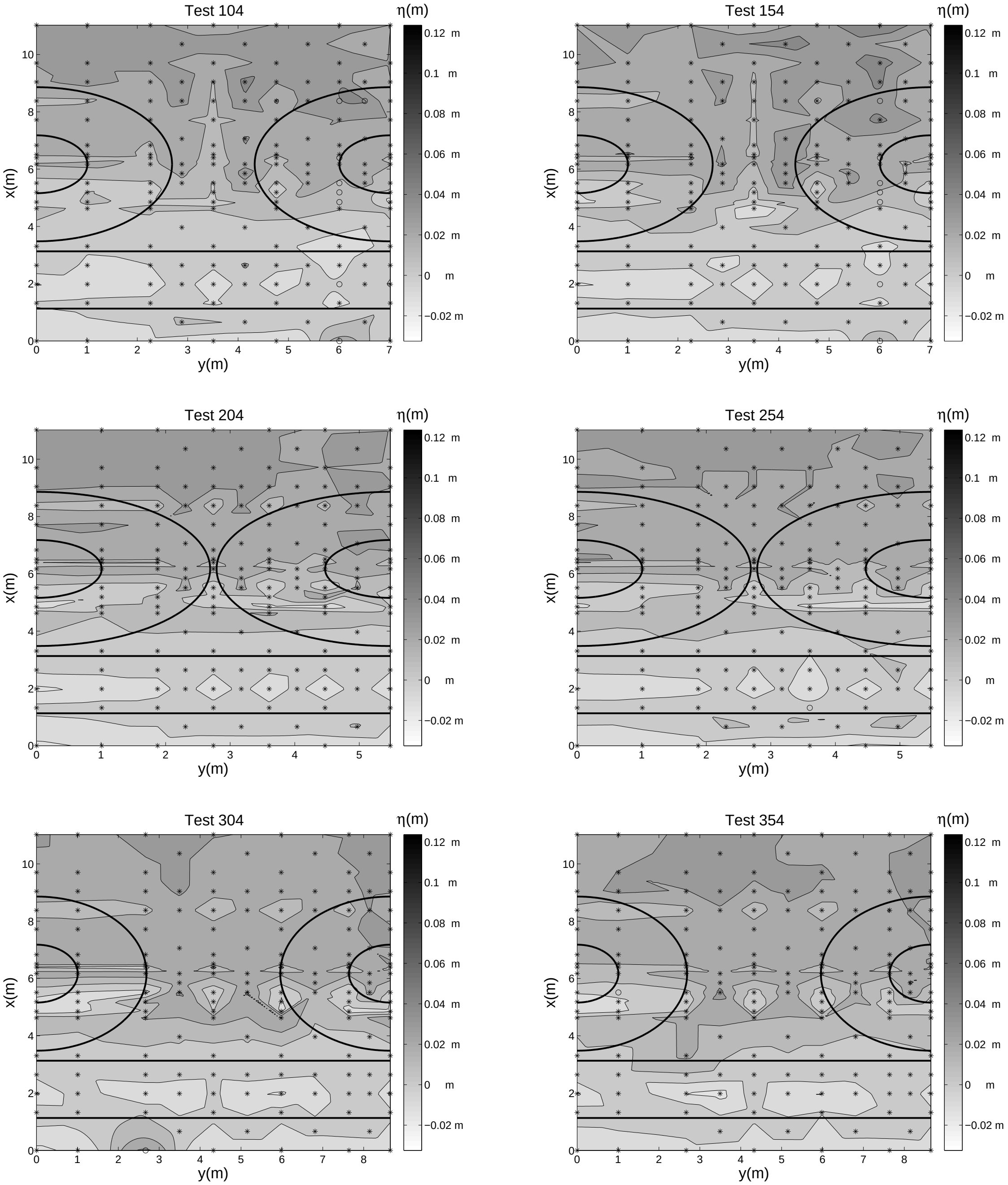

Test 104

Test 154

Test 204

Test 254

Test 304

Test 354

Fig. 57. Contour of MWL (contour interval 0.01 m) from case 4. Interpolated data (○). Measured data (∗).

encounter greater variability in the bathymetry compared to tests 304 and 354. The setup occurs sooner for the largest spacing at about $x = 5$ m, in the channel. Whereas, for the shortest spacing, the wave setup starts at about $x = 6$ m, all along the region of study. In general, a distinct separation at about $x = 5$ m is noticeable on the six contour plots in Figure 57. The plots of vegetated tests are fairly similar to the plots of the non-vegetated tests. For an intermediate spacing between the islands, illustrated by Test 104 and 154, a low MWL seems to extend in the cross-shore direction, in the middle of the channel. This interesting feature attests to a lower MWL in that region surrounded by wave setup. This depression in the MWL attest of the formation of a rip current directed offshore through the channel as the flow mass aims to counteract the difference in MWL.

Accordingly, in case 3 where the wave frequency is higher, and the water depth is the same as case 4, similar features occurs. However, the wave setup downstream of the islands is less with about $\sim$0.2 cm difference. Along with the comparison with case 4, decreasing the water depth and keeping the same wave frequency as in case 6, give rise to a wave setup twice as low as for case 3, with a value of about $\sim$0.5 cm. The offshore MWL are equivalent in magnitudes for the three cases 3, 4, and 6. On the contrary, in case 5, the mean water level spatial distribution is the most homogeneous and displays the weakest wave setup nearshore. To illustrate this observation, Figure 58 exposes the different contour plots of the MWL variation over the sampled region for the three wetland configurations, without (on the left side) and with vegetation (on the right side). Tests 205 and 255 display a very slight increase in MWL nearshore, with respect to the zero water level. Also, an augmentation of the MWL appears uniformly in the longshore direction, for $4 \text{ m} < x < 5 \text{ m}$, which is the location of the breaker region. After breaking, $5 \text{ m} < x < 5.5 \text{ m}$, the MWL decreases due to the increase of the wave height requiring a greater volume of water

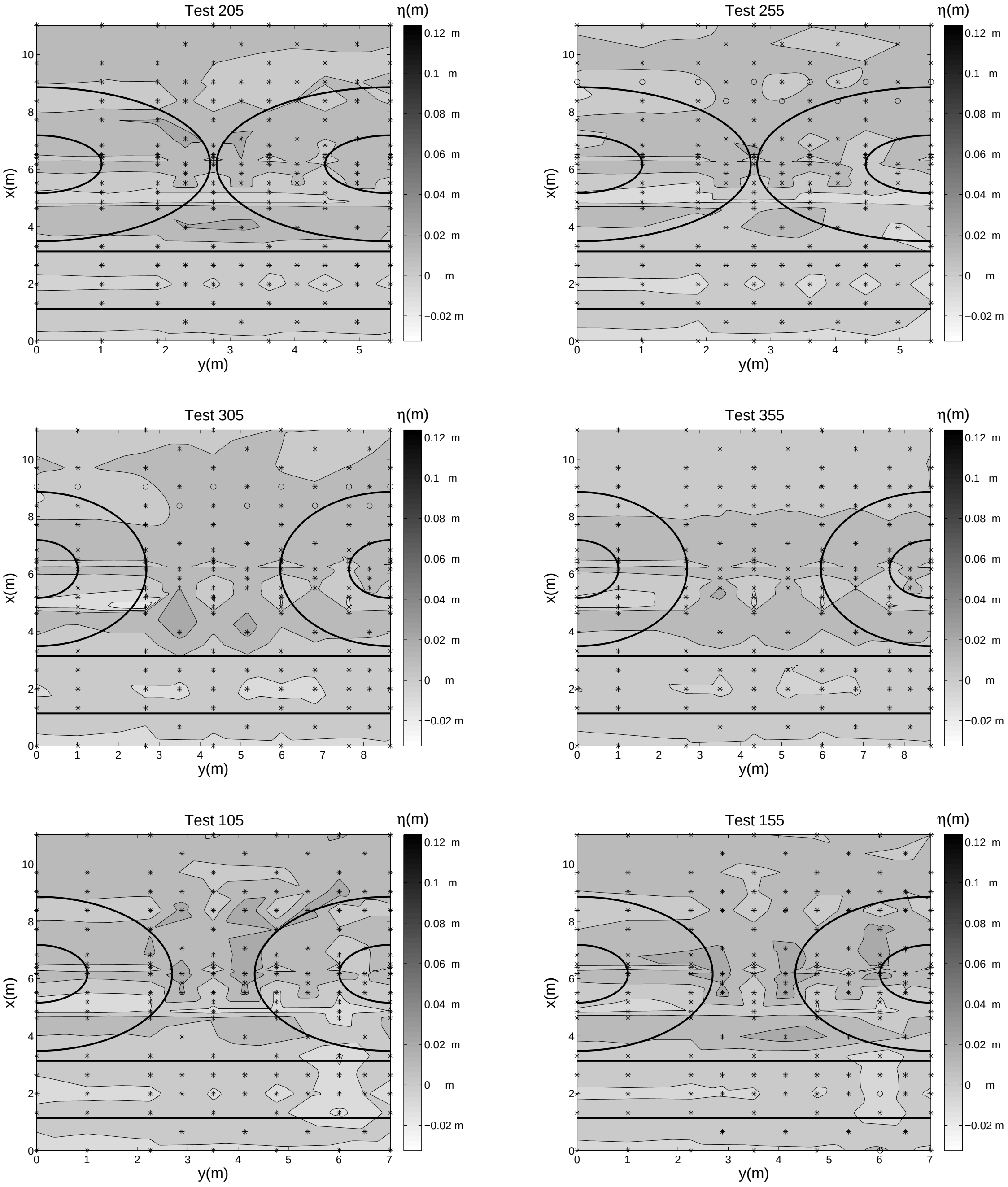

Fig. 58. Contour of MWL (contour interval 0.01 m) from case 5. Interpolated data (∘). Measured data (∗).

supplemented to the plunging breaker. On the top of the mound, the MWL increases slightly as the waves propagate on a flat bottom due to the mass of water supplied by the breaking of the wave. A dissipation of the mass downstream of the mound reduces the MWL. Overall, the contour map seems homogeneous in the longshore direction and no particular difference in the MWL variation is noticeable between test 205 and 255, when adding the vegetation patches. It is important to notice the number of interpolated data on the contour plot of Test 255, nearshore. A more interesting feature is displayed in test 305 and 355. The plots are for the most parts, identical, except nearshore. A maximum MWL extends in the range 3.5 m $< x <$ 8 m, which almost spread all along the total diameter of the islands. Lower spots of MWL, with respect to the still water level, are isolated and concentrated in the breaker zone. Upstream and downstream of the mounds, the MWL seems uniformly distributed on both sides of the mounds as if they balanced each other out exchanging flow rate through a region of higher MWL. This characteristic is particularly more obvious in Test 355 with the vegetation fields included. In test 105 and 155, a region of higher MWL, with respect to the still water level, is concentrated in the middle of the channel and may have resulted from the phase lag in the breaking of the waves relative to the breaker zone. For instance, using the sampled data in the nearshore region defined for $x >$ 6.0 m, the averaged value of the measured MWL has been computed and summarized in Table 12. The same operation has been done in the offshore region and given in Table 13.

The values of the average MWL nearshore and offshore remain fairly constant within a case as shown by the very small values of the standard deviations. In the offshore region, a zero average MWL is true in all tests.

As wave conditions 1 and 2 were tested only for one wetland configuration out of three, no comparision is possible within the different series. A larger wave setup

Table 12. Averaged MWL (in meter) in the nearshore region for $x > 6.0$ m . X = not tested in the experiment.

Case / Series	1	2	3	4	5	6
100	0.0281	0.0294	0.0227	0.0261	0.0131	0.0175
150	0.0331	0.0360	0.0233	0.0271	0.0133	0.0193
200	X	X	0.0214	0.0258	0.0117	0.0182
250	X	X	0.0205	0.0254	0.0109	0.0159
300	X	X	0.0190	0.0247	0.0107	0.0171
350	X	X	0.0191	0.0250	0.0099	0.0158
Standard deviation	0.0035	0.0047	0.0018	0.0008	0.0014	0.0013

Table 13. Averaged MWL (in meter) in the offshore region for $x < 6.0$ m (unit: meter). X = not tested in the experiment.

Case / Series	1	2	3	4	5	6
100	0.0124	0.0102	0.0098	0.0059	0.0031	0.0030
150	0.0185	0.0109	0.0087	0.0056	0.0051	0.0040
200	X	X	0.0081	0.0054	0.0050	0.0029
250	X	X	0.0088	0.0059	0.0030	0.0030
300	X	X	0.0060	0.0053	0.0047	0.0040
350	X	X	0.0088	0.0065	0.0049	0.0050
Standard deviation	0.0043	0.0005	0.0013	0.0004	0.0010	0.0008

occurs nearshore and in the channel because of the larger input wave compared to the other cases. The wave setup is maximized by the presence of the vegetation and increases the wave setup by approximately 5 cm in both case 1 and 2. Some spots of very high values of the MWL appear on these contour plots and require a verification of the concerned time series. The contour plot of test 102 is given in Figure 59 as a reference. Times series of cases 1 and 2 require further work to figure out incoherent values of MWL. However, general similarity in the spacial variability of the MWL with the shallower wave conditions tested for the same spacing between the islands could suggest similarities also for the other island spacings.

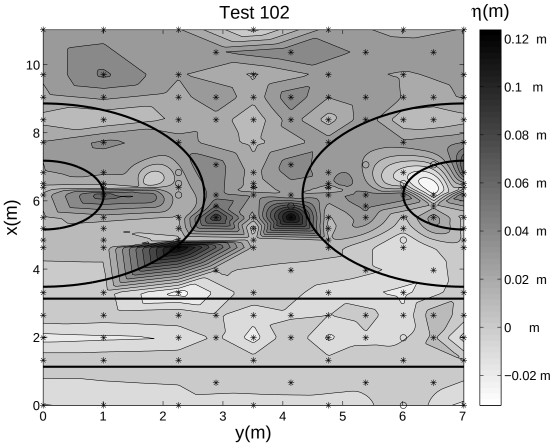

Fig. 59. Contour of MWL (contour interval 0.01 m) for Test 152. Interpolated data (○). Measured data (∗).

A general overview attests that the change in bathymetry influences the variation in MWL for all the tests. For the shortest spacing between the islands corresponding to $L_{seg} = 3.46$ m, the islands are very close to each other at the toes of the mounds as one joint structure. On the other hand, when the islands are the farthest from each other with $L_{seg} = 6.64$ m, most of the sampled region is flat. Consequently, for these two wetland configurations, the change in topography does not significantly affect the longshore variability of the wave field. Hence, the spacing between the islands interacts with the hydrodynamic process, and more precisely with the longshore variations of the flow dynamic. As a result, as the marsh segments get closer to each other (series 200 and 250), the MWL remains mostly constant in the longshore direction and shows the same pattern in setup and setdown in the crosshore direction as shown in Figure 57. Test 304 displays the same characteristics as the marsh segments are placed further apart from one another. This characteristic is the evidence of the existence of an island-flow relationship which is a function of the islands spacing.

c. Summary

Evidence of wide regions of wave setup in the surfzone have been found in all the tests. The weakest wave setup occurred in case 3 and the strongest in case 4, ignoring cases 1 and 2 as these two wave conditions were abandoned for $L_{seg} = \{3.46,\ 6.64\}$ m. The nearshore average MWL remained constant for a given wave condition, as the bathymetry of the wetland changed. For $L_{seg} = 5.00$ m, a local elevation of the MWL in the nearshore part of the channel is characteristic of the formation of a rip current system, characteristic that does not appear for other island spacings.

In other words, the longshore variability of the flow field is confined in a narrow region ($L_{min} < L_{seg} < L_{max}$) which can be identified as a first hydrodynamic state. The outer region ($L_{seg} \in [0, L_{min}[\ \cup \ ]L_{max}, +\infty[$) can be divided into two other hydrodynamic states. Hence, a second region is defined corresponding to $L_{seg} \in [0, L_{min}]$, where L_{min} is the minimum length at which the marsh segments do not interact with the longshore flow field. The critical distance $L_{seg} = 0$ corresponds to the point where two islands combine and form a single island. In this interval, the gap between the islands gets too narrow, preventing the evolution of a more complex flow structure due to an insufficient space. The third region corresponds to $L_{seg} \in \,]L_{max}, +\infty[$ where L_{max} is the distance where the marsh segments are far enough apart to be considered hydrodynamically isolated from each other. The design setup at the Haynes Coastal Engineering Laboratory was well designed to capture this important feature of the flow, and further analysis is needed to confirm this hypothesis.

2. Significant Wave Height

a. Method

In order to analyze the wave activity in the modeled wetland and evaluate the wave attenuation by vegetation, the significant wave height H_{m0} has been computed using the following equation from wave spectral analysis:

$$H_{m0} = 4.004\sqrt{m_0} = 4.004\sigma \tag{4.2}$$

where m_0 is the zeroth-moment of the variance spectrum and σ is the standard deviation of the detrended surface elevation sampled over a period of 420 s.

b. Results

As a connection to the contour plots displayed in Section B, the maps of spacial variations of the significant wave height with and without vegetation for case 4 are shown in Figure 60. The measurements show slight variations of H_s offshore whereas close to $x = 5$ m the wave height decays significantly due to the strong breaking induced by the slope of the marsh segments. All these maps show a good symmetry with the centerline of the islands which is in accordance with the symmetry of the experimental model. Also, comparing the vegetated and the non-vegetated tests, similar contours are distinguishable but differ from each other by their magnitudes.

A greater longshore variability in H_s is noticeable in Test 104 and 154 on both sides of the marsh segments, offshore and in the surf zone. More generally, for series 100 and 150, the map of H_s can be split into three distinct regions. First region (I), covers the whole channel and is characterized by greater values of significant wave heights all along the marsh fringes compared to the respective value obtained outside of the channel, at the same x-coordinate. The two other regions (II.a and II.b) are mirror symmetric to each other and are characterized by a lower wave height offshore compared to the channel. In those two mirror symmetric regions, the mean wave heights are smaller than the corresponding wave height at the same cross-shore distance in the main channel, illustrating the wave damping by the presence of the unvegetated mounds. A sketch of this division is given in Figure 61. The significant wave height is clearly diminished in the surfzone by the presence of the mounds. However, in Test 154 with vegetation, the overall values of H_s are greater than the corresponding test without vegetation, 104. This particular feature also occurred in Test 101. This increase in the mean wave height may be due to the reflection of the waves when encountering the vegetation fields. Indeed, the input and reflected wave heights add up resulting in a greater measured wave height at the wave gauges. The corresponding wave height in the middle of the channel and on the centerline of the two islands is given in Figure 62 for Tests 104 and 154 to compare the cross-shore variation of H_s and $\bar{\eta}$ measured through the rip channel to that on the centerline of the two mounds. The variation in the mean wave height shows similar trend in both vegetated and non-vegetated test but the magnitudes are relatively higher in Test 154. Whereas, in the variation of $\bar{\eta}$, the trend seem to be identical in magnitude in both tests.

On the contrary, for Test 204, 304, and their respective vegetated tests, the

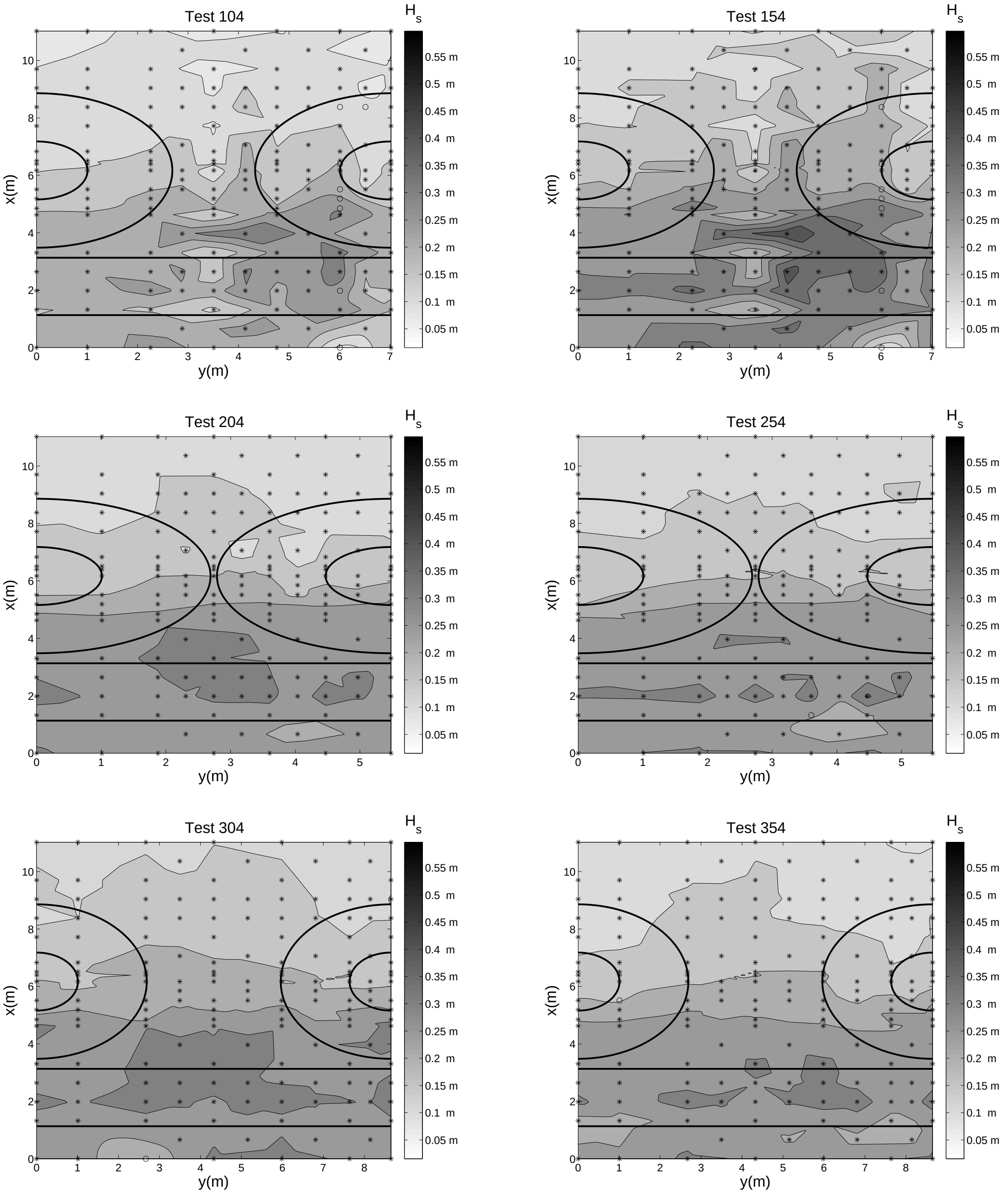

Fig. 60. Contour maps of H_s (contour interval 0.05 m) for case 4. Interpolated data ($\circ$). Measured data ($*$).

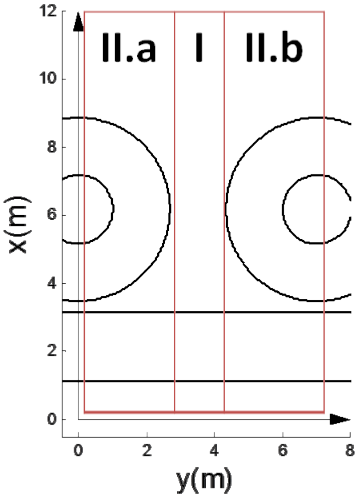

Fig. 61. Contour map division for Series 100 and 150.

longshore variability of the wave height is much less significant, displaying a more homogeneous distribution of the wave height in the longshore direction. The decrease in wave height is still located at the breaker line, however, remnants of higher H_s inside the narrow channel are still noticeable but dissipate rapidly shoreward. The wider the channel, the wider the H_s elevation is downstream of the channel, as shown by the relatively smooth hill in the H_s contours.

In the same way as for the MWL, using the sampled data in the nearshore region defined for $x > 6.0$ m, the averaged value of the measured H_s has been computed and summarized in Table 14 and compared to the values obtain offshore for $x < 6.0$ m, given by Table 15, in order to evaluate the wave attenuation by the marsh segment. Similarly, the values of the average H_s nearshore and offshore remain fairly constant within a case as shown by the very small values of the standard deviations. The wave

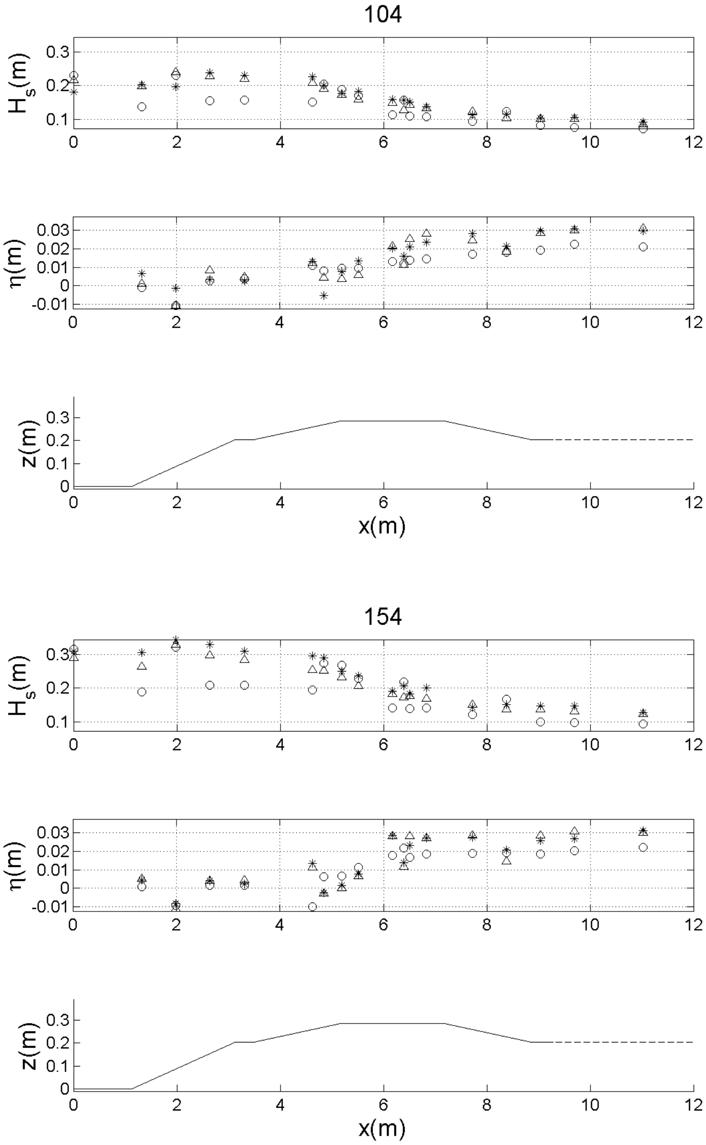

Fig. 62. Comparison between the variation of H_s in the right mound ($*$), the left mound ($\triangle$) and on the channel ($\circ$) for Tests 104 and 154.

is attenuated by ~10 cm in the surfzone compared to offshore in cases 1 to 4. In the shallower water depth, case 5 and 6, the averaged wave height is diminished by half with respect to the offshore region. Comparing the vegetated and the non-vegetated tests, excluding Tests 101/151 and 104/154, all the values of the mean H_s attest to a damping of the wave nearshore when the vegetation patches are present, with an attenuation of about 1 to 2 cm.

Table 14. Averaged H_s (in meter) in the nearshore region for $x > 6.0$ m. X = not tested in the experiment.

Series \ Case	1	2	3	4	5	6
100	0.2198	0.2706	0.1341	0.1328	0.0680	0.0905
150	0.2921	0.2810	0.1264	0.1745	0.0546	0.0737
200	X	X	0.1273	0.1586	0.0478	0.0652
250	X	X	0.1253	0.1586	0.0483	0.0643
300	X	X	0.1617	0.1729	0.0525	0.0693
350	X	X	0.1220	0.1563	0.0484	0.0649
Standard deviation	0.0511	0.0074	0.0147	0.0005	0.0077	0.0101

To further explore the wave damping, the cross-shore variation of H_s and $\bar{\eta}$ at the centerline of the middle islands is given in Figure 63, where the wave damping by the vegetation field is as expected in case 3 but not as significant in case 4. In the plots of $\bar{\eta}$, a peak is located at $x = 5$ m characterizing the location of the breaker zone. The general trends show an increase in wave setup as the wave approaches the shoreline. By adding the vegetation, the MWL increases offshore and decreases

Table 15. Averaged H_s (in meter) in the offshore region for $x < 6.0$ m. X = not tested in the experiment.

Series \ Case	1	2	3	4	5	6
100	0.2990	0.3966	0.2340	0.2205	0.0987	0.1593
150	0.3900	0.3989	0.2160	0.2894	0.0930	0.1463
200	X	X	0.2110	0.2672	0.0856	0.1314
250	X	X	0.2114	0.2662	0.0854	0.1299
300	X	X	0.2219	0.2746	0.0842	0.1315
350	X	X	0.2066	0.2611	0.0831	0.1274
Standard deviation	0.0643	0.0016	0.0099	0.0231	0.0062	0.0125

nearshore compared to the non-vegetated test.

c. Summary

The results from the experimental investigation into the wave activity in the wetland model show an a relatively important damping of the waves as they propagate over the mounds. This attenuation of the wave height was maximum in the deepest water depth tested with a ∼10 cm difference between the offshore region and the surfzone. The complementary effect of the vegetation was much less important, representing approximately $1/10^{th}$ of the damping provided by the presence of the mounds. The wave height elevation is persistent along the channel whereas it is attenuated downstream of the mounds.

The longshore variability of the wave height evolution has shown to depends on the island-flow relationship as defined in Section 1. Indeed, three regions have been

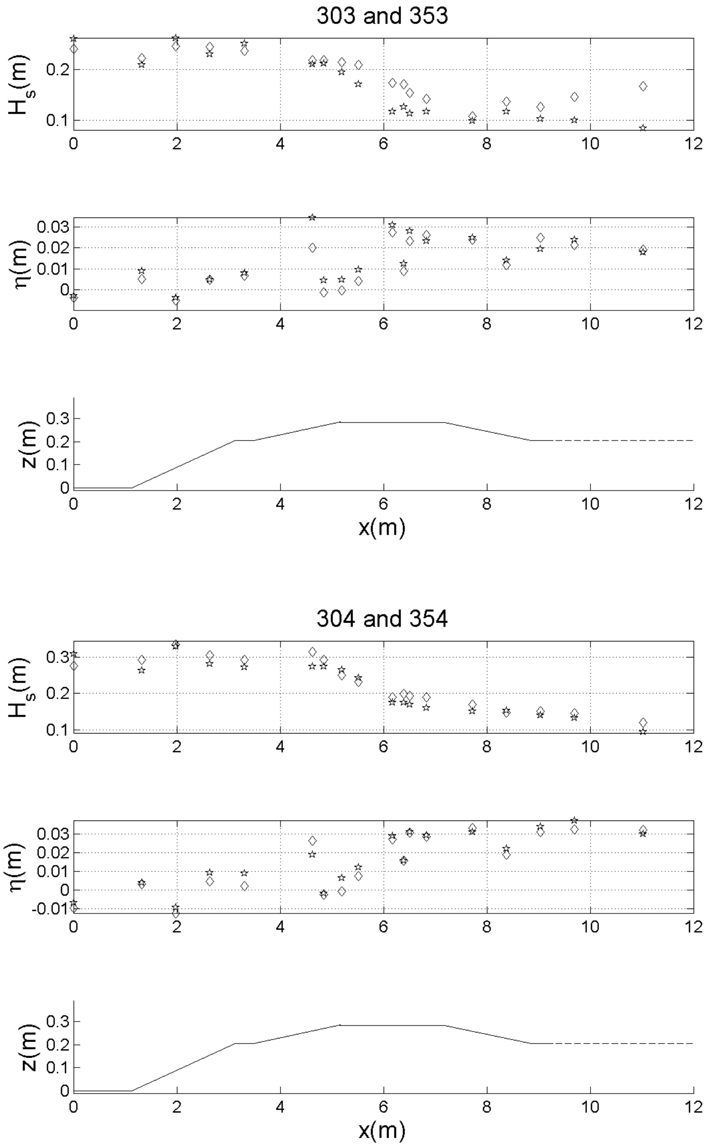

Fig. 63. Comparison between the cross-shore variation of H_s and $\bar{\eta}$ on the right mound with ($\star$) and without vegetation ($\diamond$) for Tests 303 and 353 and for Tests 304 and 354.

distinguished for $L_{seg} = 5.00$ m, in accordance with the symmetric mound-channel-mound topography of the sampled region. In contrary, for $L_{seg} \in \{3.46, 6.64\}$ m, the significant wave height remained constant in the longshore direction, except downstream of the channel as explained previously.

C. Phase Averaging Analysis

Waves traveling above the marsh segments and vegetation fields are subject to variation in bathymetry and drag forces. These parameters induce phase lags in the propagation of the wave crest compared to waves traveling on a flat bed as shown in Figure 52. In order to estimate these phase lags and the deceleration of the waves at each wave gauge location, a phase averaging analysis has been conducted (Yamagishi, Togano and Tashiro 2007).

1. Method

a. Phase Averaging Technique

To perform the phase averaging method, the wave gauge located in the offshore part of the basin measuring the input wave coming into the marsh was used as the reference signal, $s_{ref}(t)$.

For each run, the reference wave gauge was taking measurement along with the eighteen other wave gauges and the five ADVs, simultaneously. The phase angles for all reference signals $s_{ref}(t)$ were obtained by dividing each wave cycle into regular intervals. A cycle of the signal is determined by the interval between two zero-upcrossing of the detrended signal, and every signal contained at least 100 cycles. A half cycle of the reference signal is determined by the interval between the neighboring zero-upcrossing and zero-downcrossing of the reference signal. When the input wave has a period of $T = 2.0$ s, each cycle was divided into 100 regularly spaced intervals and for a wave period $T = 3.0$ s, each cycle was divided into 150 regularly spaced intervals. Figure 64 shows definition criteria for a cycle.

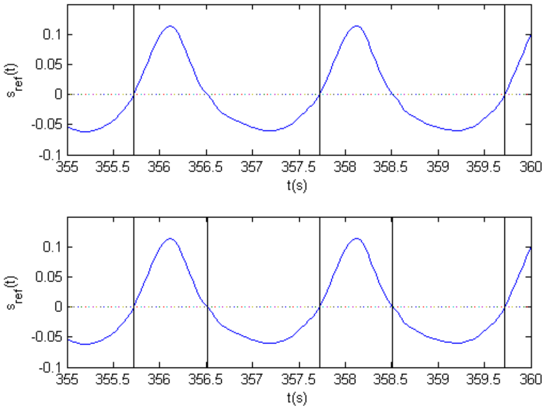

Fig. 64. Cycle and half-cycle definition for the reference signal $s_{ref}(t)$.

In order to change the variable from time, t, to phase angle, θ, the latter, is defined by the equations as follows:

$$\theta = \pi \frac{t - t_{u,i}}{t_{d,i} - tu, i} \qquad \text{if } t_{u,i} < t < t_{d,i} \tag{4.3}$$

$$\theta = \pi \frac{t - t_{d,i}}{t_{u,i+1} - td, i} + \pi \qquad \text{if } t_{d,i} < t < t_{u,i+1} \tag{4.4}$$

Here, $t_{u,i}$ is the zero-upcrossing time in which the reference signal s_{ref} satisfies the condition $s_{ref} = 0$ and $ds_{ref}/dt > 0$. $t_{d,i}$ is the zero-downcrossing time in which the reference signal s_{ref} satisfies the condition $s_{ref} = 0$ and $ds_{ref}/dt < 0$. Both $t_{u,i}$ and $t_{d,i}$ were interpolated linearly using real measured data as shown in Figure 65. The index i corresponds to the cycle number from the initial time $t = 0$ and the phase angle is ranged between $0 \leq \theta \leq 2\pi$. Hence, from equation 4.3 and 4.4, the time of the signal s_{ref} at the phase angle θ is defined as follows:

$$t = t_{u,i} + \frac{t_{d,i} - t_{u,i}}{\pi}\theta \qquad \text{if } 0 \leq \theta \leq \pi \tag{4.5}$$

$$t = t_{d,i} + \frac{t_{u,i+1} - t_{d,i}}{\pi}(\theta - \pi) \qquad \text{if } \pi \leq \theta \leq 2\pi \tag{4.6}$$

(4.6)

The interval $t_{d,i} - t_{u,i}$ represents the half cycle, and $t_{u,i+1} - t_{d,i}$ represents the next half cycle.

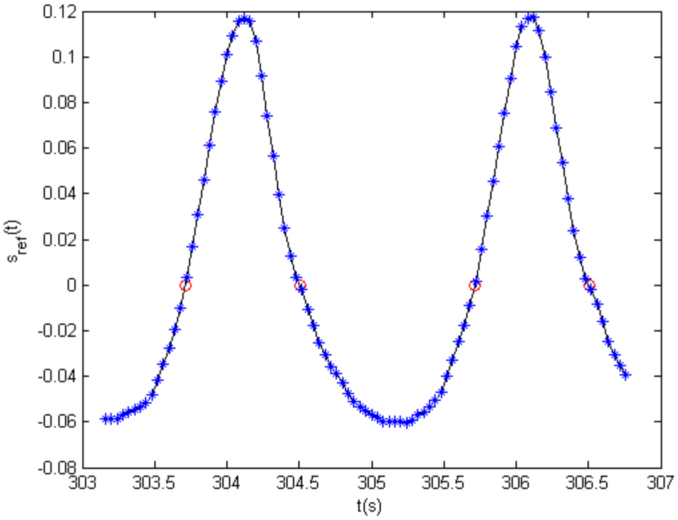

Fig. 65. Linearly interpolated $t_{u,i}$ and $t_{d,i}$ ($\circ$) from real data ($*$).

As a result, in this method, the phase-averaged signal for the reference wave gauge located at $(x, y) = (x_0, y_0)$ in the wave basin and at a given time t can be obtained as follows:

$$< s_{ref}(x_0, y_0, t) >= \frac{1}{N} \sum_{n=0}^{N} s_{ref}(x_0, y_0, t + nT) \tag{4.7}$$

Here, T is the wave period defined as $T = t_{u,i+1} - t_{u,i}$. Subsequently, from equation 4.7 the phase averaging applied to every other wave gauge at the location $(x, y) = (x_0 + \Delta x, y_0 + \Delta y)$ from the same test run at the same given time t is defined by:

$$< s(x, y, t) >= \frac{1}{N} \sum_{n=0}^{N} u(x, y, t + nT) \tag{4.8}$$

To perform this summation of cycles point by point, the data were linearly interpolated from the measured data onto a created phase angle grid ranging from 0 to 2π, so that every point of each cycle was summed up at the same phase angle from the arbitrary grid. The grid was divided into of 100 and 150 regularly spaced intervals for 2.0 s and 3.0 s wave respectively. Figure 66 shows an example of the interpolation procedure.

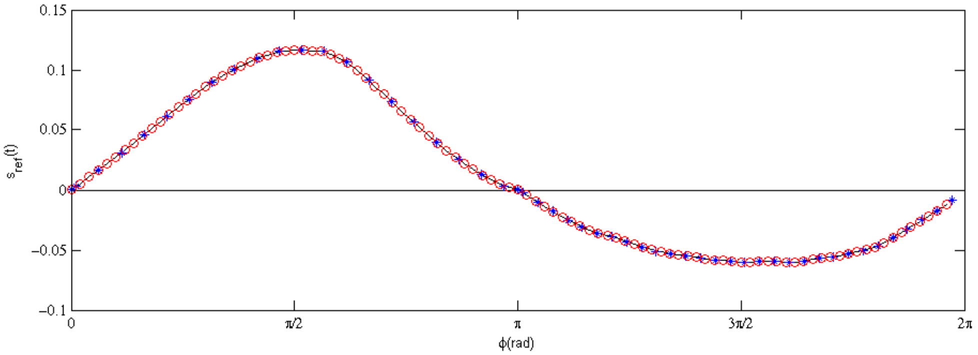

Fig. 66. Real measured point ($*$) and interpolated point ($\circ$) onto the arbitrary phase angle grid for one cycle.

Afterwards, using the located times of zero-upcrossing and zero-downcrossing in the reference wave gauge signal, every other time series from wave gauges and ADVs were divided into the same exact cycles as the reference time series. Then, the phase averaged formula 4.8 was applied to get the averaged wave cycle at each sensor.

With these results and thanks to the new time series generated of the phase averaged cycle at each sensor, contour plot movies were created. Every single frame represented the phase averages contour plots as the phase angle θ, where $\theta \in [0,2\pi[$. The output movies allowed to estimate how many waves propagates within the wetland for one cycle of the wave. Also, the phase lag between one test to another may be detected comparing two movies playing at the same frame rate. As an example, two frames are displayed in Figure 67.

In addition, it is important to notice the lower resolution on the left side of the grid which, due to the linear interpolation used, makes the wave crest disappear at about $x = 4$ m in frame 51 and at $x = 1$ m on frame 85. Also, due to the lack of resolution in between two wave gauges in the grid map, as the wave crest propagates in between two sensors, the linear interpolation used was not able to interpolate the wave crest in the middle of a couple of wave gauges. This effect could result in the disappearing and reappearing of the wave crest as the wave propagates in phase average wave movies.

Consequently, determining the phase of zero-upcrossing for each phase averaged signal allows the phase lag, $\Delta\phi$, of the wave at each wave gauge to be determined location with respect to the reference wave gauge as shown in Figure 68.

b. Wave Propagation on a Flat Bottom

In the absence of marsh segments, linear wave theory was used to compute the phase speed C of the wave (Dean and Dalrymple 1984), which was calculated by substituting

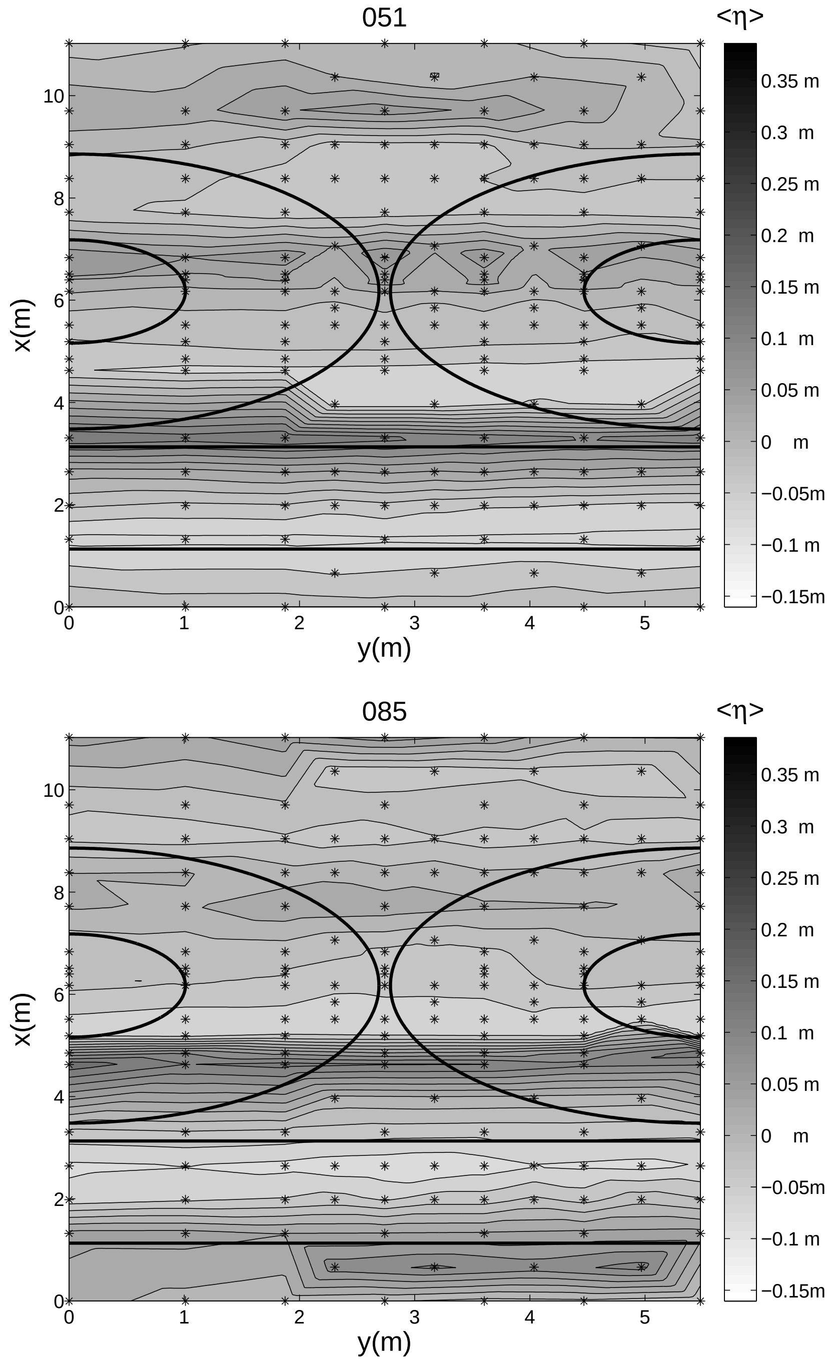

Fig. 67. Frame 51 and 85 of the wave gauges phase averaged contour plots for Test 203.

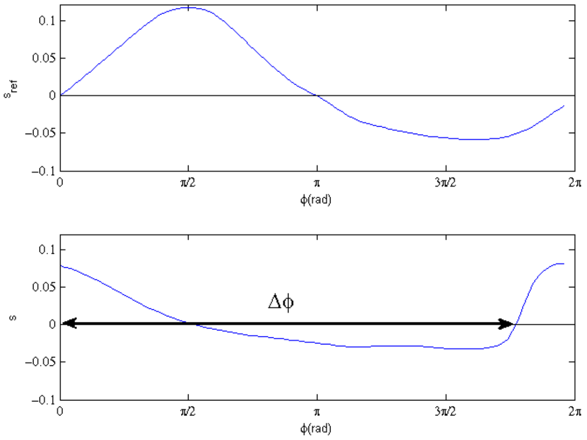

Fig. 68. Phase average of an arbitrary signal, s, with respect to the reference wave gauge s_{ref}.

the peak period and the water depth with respect to the bathymetry into the linear wave theory dispersion relationship given as:

$$\omega^2 = gk\tanh(kh) \qquad \text{where} \qquad \omega = \frac{2\pi}{T} \tag{4.9}$$

as well as using the relationship between wavelength and wavenumber k defined as:

$$k = \frac{2\pi}{L} \tag{4.10}$$

In order to determine the influence of change in bathymetry due to the presence of marsh segments on wave transformation as well as the influence of the variation in vegetated and non vegetated marsh segment spacings, the wetland configuration 1, 2 and 3 corresponding to 6.64 m, 5.00 m, and 3.46 m spacing, respectively, were considered.

The simulation of the idealized case where the wave propagates toward the shore without encountering any wetlands or any obstruction was computed using linear wave theory. Hence, the wave propagates in the deep water part of the basin and shoal onto the ramp and propagates again on the shallower flat platform. Knowing the input wave characteristics at the wavemaker and using the dispersion relationship (4.9) to compute the wave length L, the phase velocity C is given by:

$$C = \frac{L}{T} \tag{4.11}$$

The variation in phase velocity, C, was computed with respect to the cross-shore (x) bathymetry of the wave basin. The shoaling coefficient (3.6) was computed using the following equation for the group velocity, C_g:

$$C_g = nC \qquad \text{where} \qquad n = \frac{C_g}{C} = \frac{1}{2}\left(1 + \frac{2kh}{\sinh 2kh}\right) \tag{4.12}$$

Given the wave height with respect to the cross-shore bathymetry, the idealized water surface elevation is given by:

$$\eta(x,t) = \frac{H(x)}{2}\cos(k(x - C(x)t)) \tag{4.13}$$

where x is the cross-shore coordinate. Assuming that the refraction coefficient is equal to 1, η is only a function of the coordinate x and the time t and is constant in the long-shore direction. Knowing the coordinate in the cross-shore direction, every time series was computed for the 170 wave gauges to simulate the wave with no wetland and compared the difference in phase with the experimental data with the marsh segments.

c. Phase Lag

The theoretically computed time series of the simulated waves were used to have a reference wave for both the experimental tests with and without vegetation patches.

First, the phase difference between each the phase angle of the zero-upcrossing of the experimental wave and the simulated waves as shown in Equation 4.14 were computed.

$$\Phi_{exp/ref} = \Phi_{ref} - \Phi_{exp} \tag{4.14}$$

$\Phi_{exp/ref}$ refers to the phase of the experimental waves Φ_{exp} relative to the same reference waves, Φ_{ref}. A rigorous caution was applied to the determination of the zero-upcrossing for the remaining wave gauges. Indeed, remaining spikes or the formation of two wave bumps after shoaling in the shallow water case obligate sometimes redefining the zero-upcrossing phase by hand, to make sure that the right phase was acquired and saved. The values were verified one at a time and automated through MATLAB. In order to make sure that two subtracted phases from the vegetated and non-vegetated experiments belonged to the same cycle of the wave, determination of the wave cycle have been done for each computed zero-upcrossing phase. In the case where the zero-upcrossing phase of the simulated and experimental waves belong to the same cycle, Equation 4.14 was applied. If the simulated wave traveled faster than the experimental wave and started a new cycle while the experimental wave was still on the previous cycle, the following formula was applied:

$$\Phi_{exp/ref} = -(\Phi_{ref} + 2\pi - \Phi_{exp}) \tag{4.15}$$

In a similar manner, if the simulated wave travels slower than the experimental wave and starts a new cycle while the simulated wave is still on the previous cycle, then the following formula was applied:

$$\Phi_{exp/ref} = -(\Phi_{exp} + 2\pi - \Phi_{ref}) \tag{4.16}$$

Equations 4.15 and 4.16 are valid if a given wave is one cycle ahead relatively to the other one but these formula are easily adaptable to multiple cycles. Overall, two to four wave cycles were detectable while propagating in the studied region and the phase difference, $\Phi_{exp/ref}$, varied between -2 rad and +4 rad, which is less than a complete wave cycle.

As a result, a positive value of $\Phi_{exp/ref}$ implies that the experimental wave travels faster than the simulated linear wave, a negative value of $\Phi_{exp/ref}$ implies that the experimental wave travels slower than the simulated linear wave and a zero value means that the two waves are in phase at that particular location.

In the basin, the waves were mostly non-linear. Non-linear waves, such as cnoidal waves, have longer wavelength than their corresponding linear wave counterparts. Therefore, it is well admitted that non-linear waves travel with a greater phase speed than linear waves in the same wave conditions (Mei et al. 1983). As an example, Figure 69 displays a strong positive phase difference $\Phi_{exp/ref}$ in the wetland region whereas, a negative phase difference appears offshore. The phase lag increases from upstream offshore to downstream nearshore, illustrating the higher phase velocity of the irregular waves relative to the simulated linear waves.

All contour plots display the same pattern with a more or less pronounced positivity nearshore and negativity offshore. It is interesting to notice also that the vegetated case compared to the non vegetated case displays similar pattern of the phase difference spacial variability as shown in Figure 70.

A strong characteristic that appears on all tests is that the vegetated and non-vegetated experiments show similar values offshore, but in the wetland region, a stronger positivity of the phase difference is clearly noticeable over the whole area. Moreover, the variability of the phase difference is uniform in the longshore direction. This characteristic demonstrates that the waves generally propagate faster in the non-vegetated region, which is expected.

In order to compare the phase of the wave with and without vegetation in the

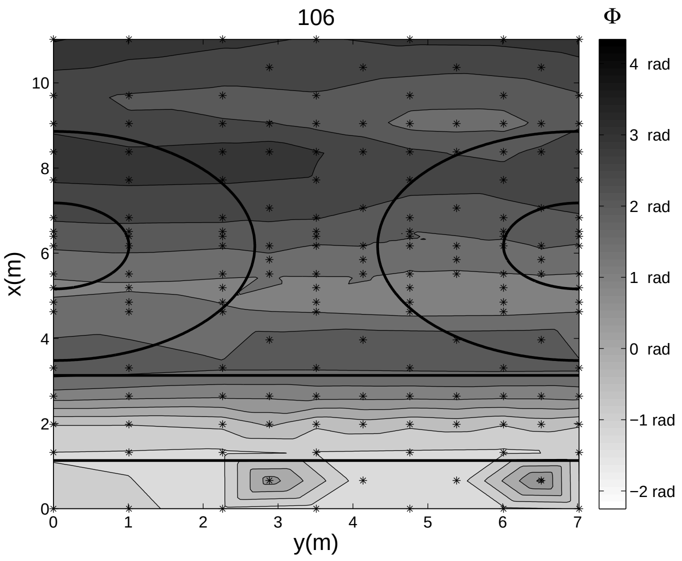

Fig. 69. Contour plot of the relative phase for Test 106.

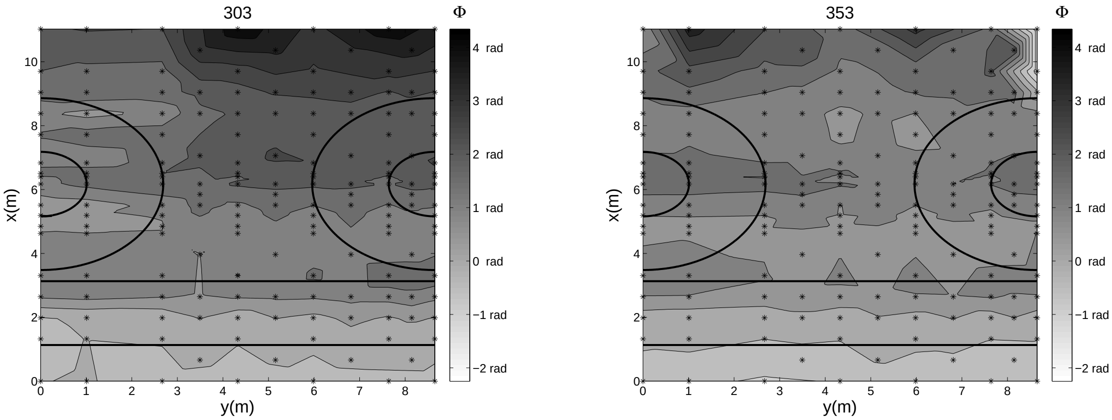

Fig. 70. Comparison of the relative phase between the vegetated case 353 and the non vegetated case 303.

experimental model, the phase lag, $\Delta\Phi$, between the waves propagating in a vegetated wetland (superscript "*veg*") with the waves propagating in a non-vegetated wetland (superscript "*noveg*") has been computed. The theoretical formula used to execute this operation is given in Equation 4.17.

$$\Delta\Phi = \Phi_{exp/ref}^{noveg} - \Phi_{exp/ref}^{veg} \tag{4.17}$$

The rock beach at the end of the wave basin generated reflected waves. This feature was the most obvious in the shallow water cases. Due to the appearance of both the input and the reflected waves in the phase averaged wave profiles, the determination of which wave oscillation corresponds to which wave was impossible, especially nearshore, as shown in Figure 71. A deeper analysis of the response of the rock beach to incoming waves is needed to solve this issue. Hence, parts of the data

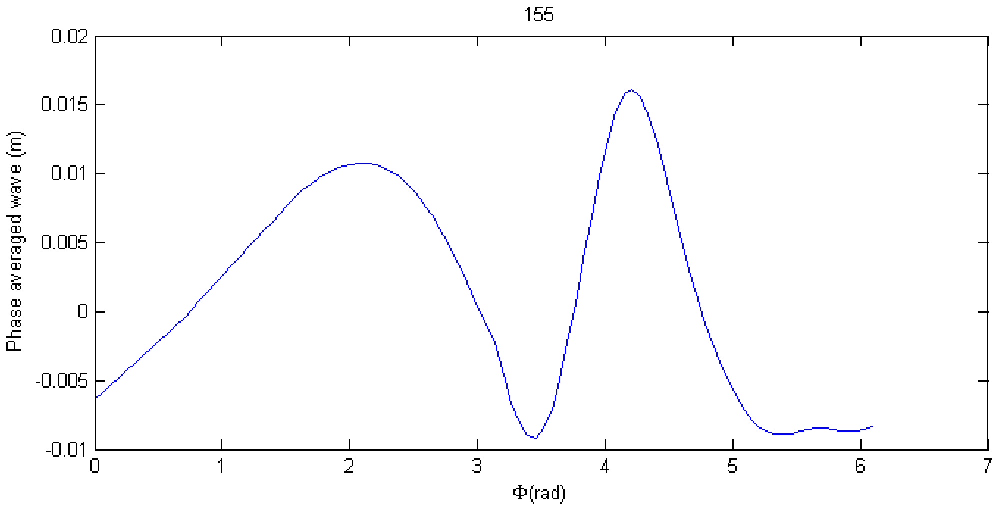

Fig. 71. Phase average of a wave gauge time series in Test 155 (gauge 3, station 1) where the input and reflected wave are apparent.

were removed from the contour maps of the phase lag as shown in Figure 78. Affected test cases are summarized in Table 16. Unfortunately, the nearshore behavior could not be analyzed for these listed tests.

The phase lag, $\Delta\Phi$, varied between -3 rad and 3 rad, which shows that the experimental wave traveling with vegetated patches and the wave traveling in a non-vegetated wetland were, at most, $\pm\pi$ out of phase with each other. A positive value of $\Delta\Phi$ implies that the experimental wave travels slower when the vegetated patches are present, a negative value of $\Delta\Phi$ implies that the experimental wave travels slower when there are no vegetated patches and a zero value means that the two waves are in phase at given locations.

Table 16. List of test cases with removed data.

Test	Number of points removed nearshore
105	29
155	37
205	29
255	40
305	29
355	47
156	13
206	10
256	10
306	10
356	25

2. Results

Most of the contour plots show a uniform phase lag with some localized areas of positive phase differences nearshore and negative phase difference offshore. The phase lag between Test 103 and Test 153 is the exception that shows a negative lag in most of the studied region as shown in Figure 72, not considering the deleted data in other tests for comparison.

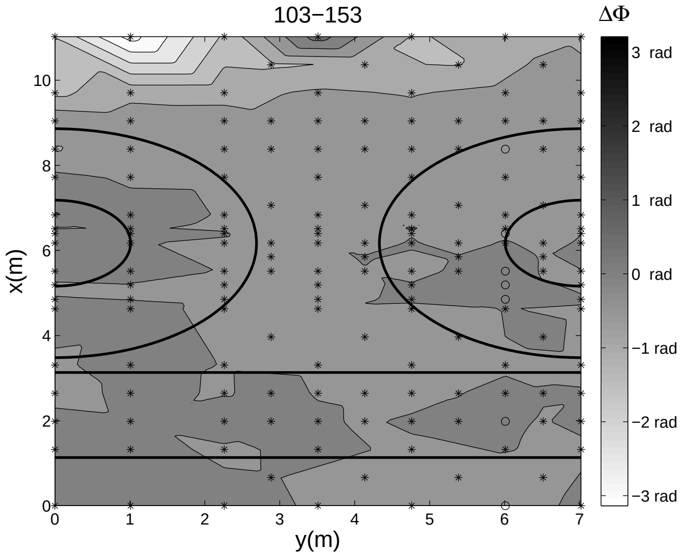

Fig. 72. Contour plot of phase lag between Tests 103 and 153.

For case 4, most of the values of $\Delta\Phi$ being very close to zero, hence, a closer look into the exact values computed and into the separated plots of vegetated and non-vegetated tests was necessary to get the behavior of the waves. Looking into the values of the phase lag $\Delta\Phi$ in Test 104-154 as displayed in Figure 73, most of the values are slightly negative nearshore implying the acceleration of the waves in

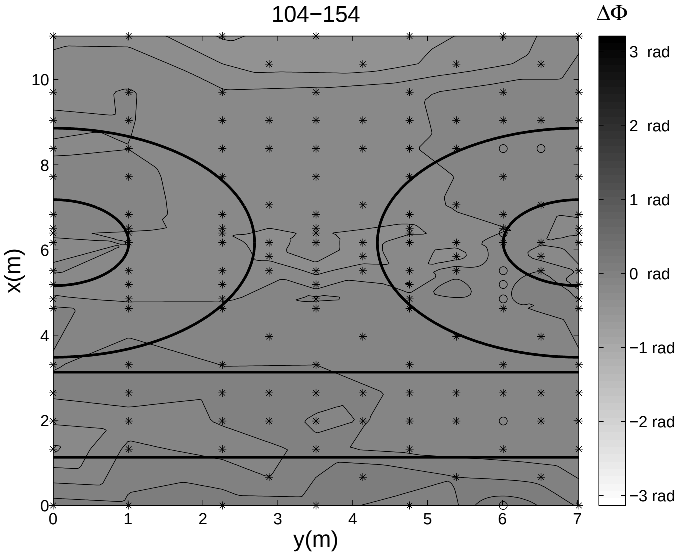

Fig. 73. Contour plot of phase lag between Tests 104 and 154.

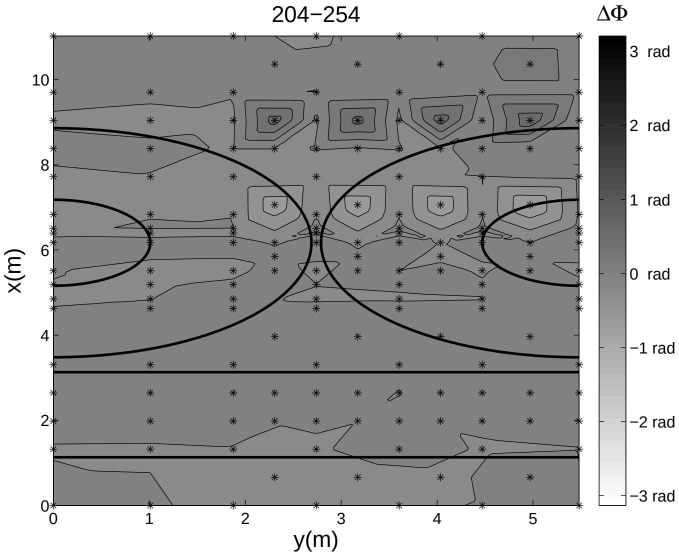

Fig. 74. Contour plot of phase lag between Tests 204 and 254.

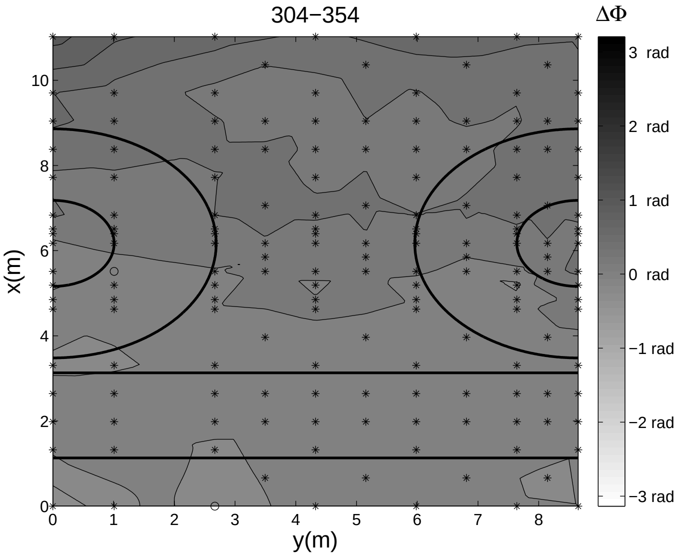

Fig. 75. Contour plot of phase lag between Tests 304 and 354.

the vegetated case. The non-intuitive behavior of these tests has been pointed out previously. In contrary, for Tests 204-254 and Tests 304-354, the positivity of the values are more obvious and the phase lag increases as the waves reach the rock beach, especially nearshore in Tests 304-354, as shown in Figure 74, and 75.

This particular example shows how the spacing of the islands correlates with the behavior of the waves. The waves are in phase offshore and on the ramp. They are slowed down and decelerate in the wetland region. However, although the waves are in phase offshore, the spacial variability of the phase difference when the waves enter the wetland region changes in a significant manner as the spacing between the islands increases as given in Figure 76, which shows the decomposition of the phases into vegetated tests and non-vegetated tests for case 4.

When the island spacing is equal to 3.46 m, a very slight difference between the vegetated case and the non-vegetated case is noticeable. The phase lag is more

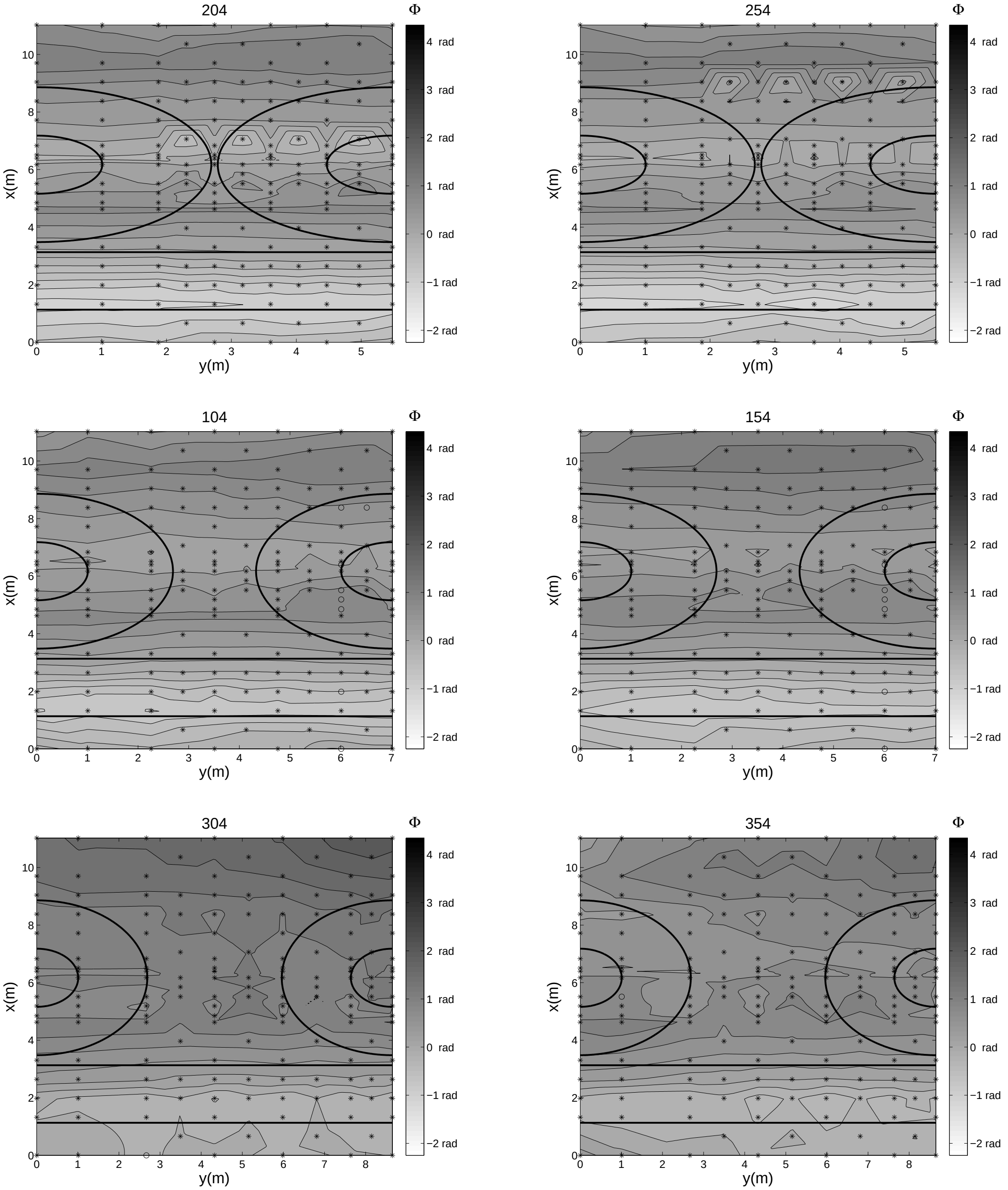

Fig. 76. Phase decomposition for case 4.

uniform in the vegetated case as shown by the decrease in the number of contour lines apparent in Figure 76 for Test 254. Another interesting feature occurs in tests 204 and 254, where the appearance of nodes happens about x = 7 m and x = 9 m, respectively.

By changing the spacing between the marsh to 5.00 m, a more positive phase lag develops in the wetland for Test 154, attesting to the acceleration of the waves in the vegetated case. At last, for a 6.64 m spacing, a greater increase in the values of the phase lag appears in Test 304 relative to Test 354. This characteristic shows deceleration of the wave in the vegetated wetland.

The shift in time of the wave response to the presence of the vegetation demonstrates the capability of the vegetated wetland in decelerating the waves for most of the wave conditions tested. Figure 77 shows the phase decomposition for case 3. Significant similarities in behavior of the waves to the island spacings with case 4 occurs at the same water depth, for a 2 s waves in case 3. The main difference results in the magnitude. Indeed, the waves seem to accelerate when the islands are vegetated compared to the two other spacings in Test 103 with respect to Test 153. The further apart the islands are, the more deceleration of the wave it creates, with vegetation, in Test 353. Most of the values of $\Delta\Phi$ are positive for the these tests. The wave is decelerated as well in Test 253 with respect to Test 203.

For a 2 s and 3 s waves, as the water depth gets very shallow (case 5 and 6, respectively), it allows the vegetation stems to be near emergent and the waves seems to be more sensitive to the change in bathymetry. Indeed, the values of the phase difference becomes greater as the water depth decreases. The maximum phase lag is about 2 rad in the wetland region for a 5 m spacing. However, for the closest and the farthest spacings, the phase lag is minimal compared to the intermediate spacing, for the same wave conditions as shown in the figure on page 131. Hence, in shallow

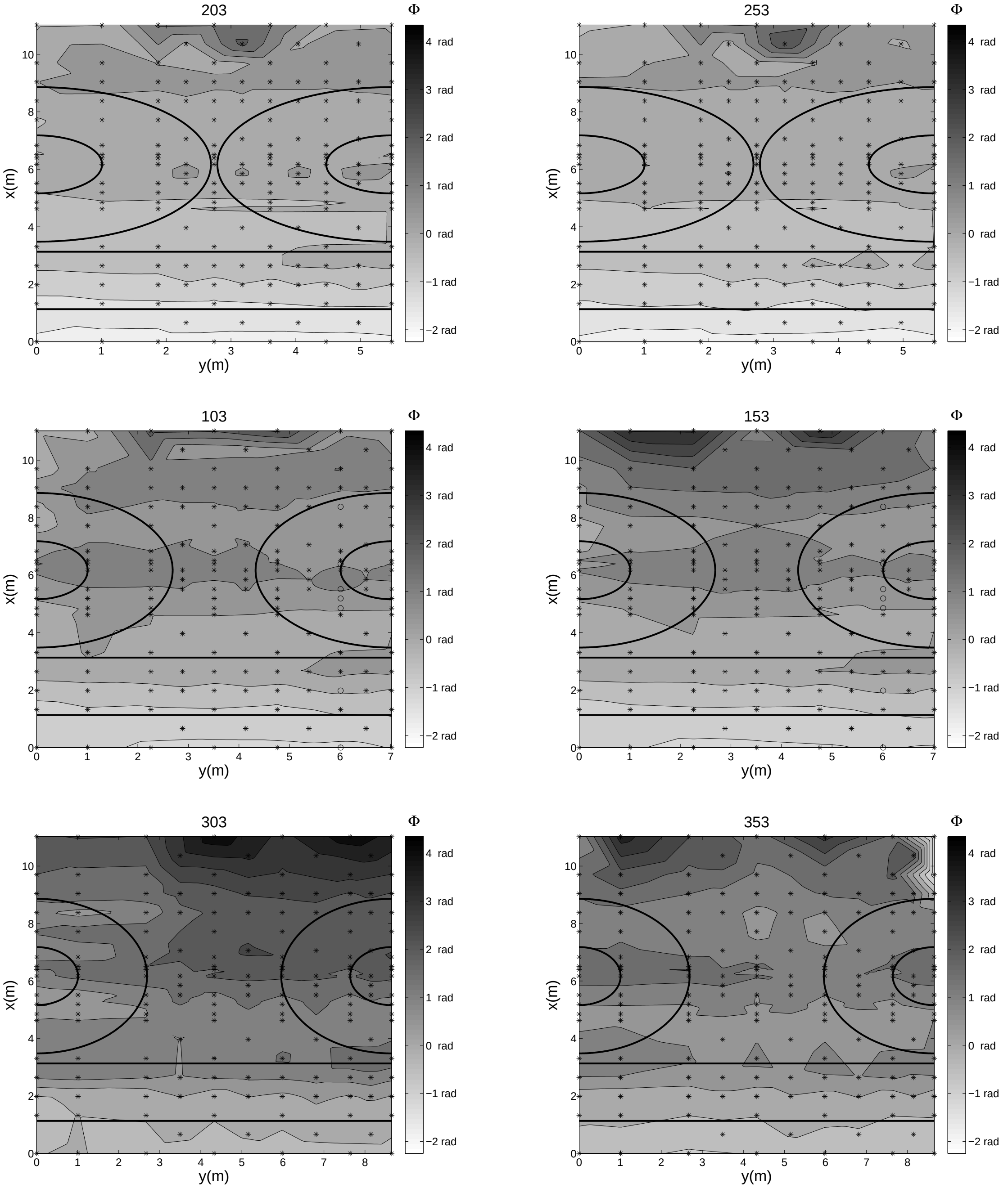

Fig. 77. Phase decomposition for case 3.

water depth, the wave shows the same feature noticed previously for the significant wave height and the mean water level, that is the phase lag becomes homogeneous when the bathymetry is more uniform and it is at its greatest value within a range of limited spacings. The blanked space nearshore corresponds to the data removed as listed in Table 16.

3. Summary

Very interesting results in the behavior of the waves nearshore have been exposed in this analysis, emphasizing in the change of water depth along with the change in topography of the wetland. Firstly, in deep water, for $L_{seg} = 5.00$ m, the wave speed decreases when the vegetation patches are present. Secondly, in intermediate deep water, the waves decelerate for $L_{seg} \in \{3.46, 6.64\}$ m, and accelerate for $L_{seg} = .00$ m, when the vegetation is added, compared to the non-vegetated case. Lastly, in shallow water, the phase speed is less when the vegetation fields are present for the three wetland configurations, and this deceleration is the most important for $L_{seg} = 5.00$ m.

In most cases, the presence of the stems plays an important role in decelerating the waves entering the surf zone.

D. Turbulence Analysis

In order to describe the turbulent velocity field from the ADVs measurements and derive the evolution of the turbulence activity properties, the analysis of the velocity field has been done. The Reynolds decomposition of the velocity field into its mean and fluctuation part has been done.

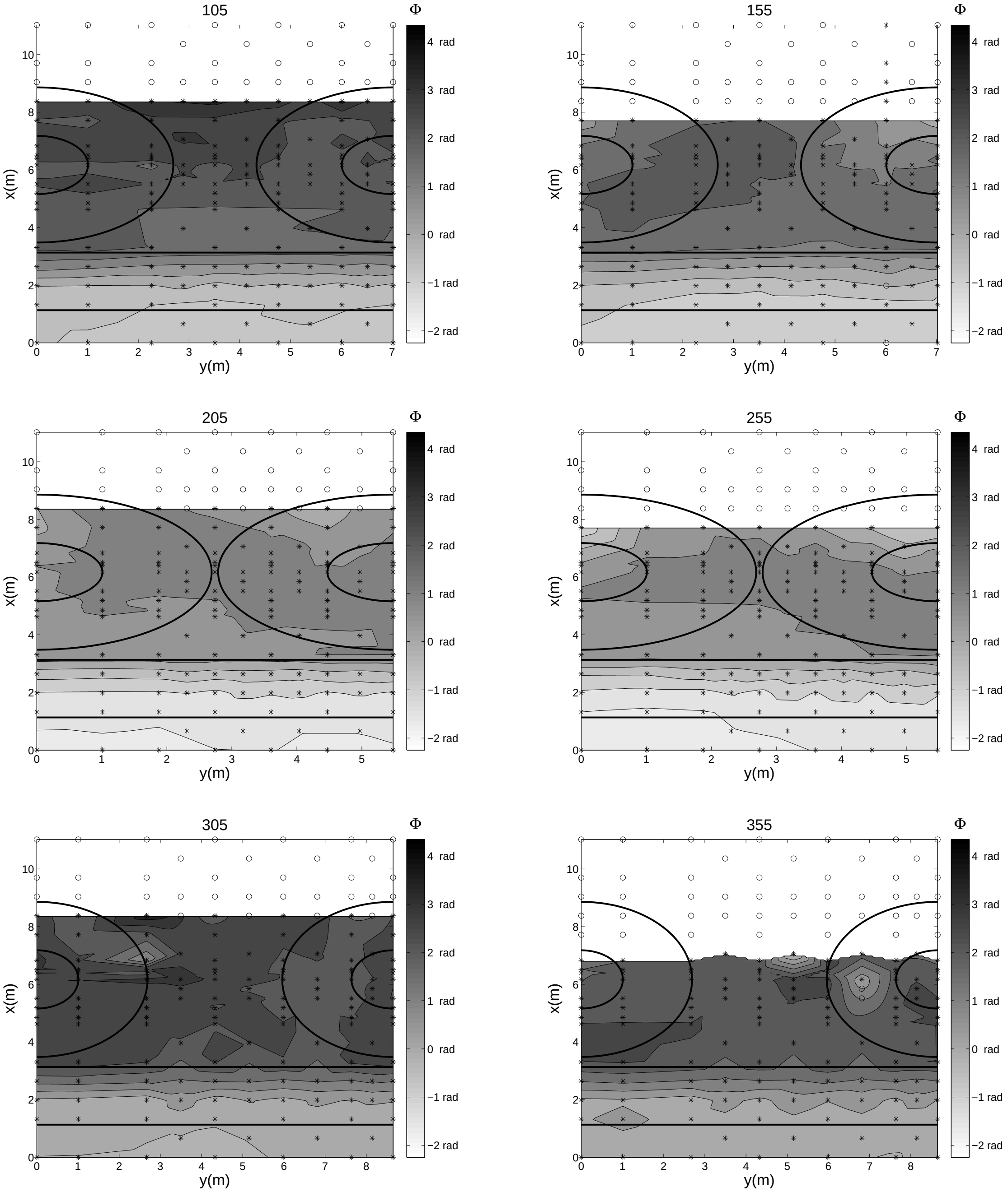

Fig. 78. Phase decomposition for case 5.

1. Method

a. Turbulence Fluctuation

The presence of the vegetation field and the particular bathymetry given by the marsh segments are likely to induce turbulent flow due to the external periodic forcing by the wavemaker. Hence, the instantaneous velocity u can be decomposed into three levels known as the triple Reynolds decomposition for a given location (x, y) and at the time t:

$$u(x, y, t) = U(x, y) + \tilde{u}(x, y, t) + u'(x, y, t) \tag{4.18}$$

where the components U, u and u' denote the time- averaged, the fluctuation with the same frequency as that of the introduced fluctuation and the fluctuation with the other frequencies, respectively. The fluctuating components u and u' are called the periodic and the turbulent component of the velocity. In addition, the instantaneous velocity is the combination of a coherent structure part where the structure by the phase-averaged component is concerned and an incoherent structure part due to the random component. From this definition, the coherent structure is hence given by:

$$< u >= U(x, y) + \tilde{u}(x, y, t) \tag{4.19}$$

Applying the method of phase averaging, described in Section C, to the data of the velocity for each component (u_x, u_y, u_z), the periodic motion of the external forcing flow has been determined. Thus, to get the turbulent component of the velocity u', the phase averaged velocity was simply subtracted from the instantaneous velocity for every single cycle as shown below:

$$u'(x, y, t) = u(x, y, t)- < u > \tag{4.20}$$

b. Turbulent Kinetic Energy

The root mean square (RMS) velocity fluctuation, known as the turbulent kinetic energy is given by the following equation:

$$k \equiv \frac{1}{2} < u'.u' >= \frac{1}{2} < u'_i u'_i > \tag{4.21}$$

The turbulent kinetic energy, defined as the mean kinetic energy per unit mass in the fluctuating velocity field, have been computed for all ADVs. Nondimensionalization was performed by dividing the turbulent kinetic energy by the mean square velocity given:

$$U^2_{rms} = \frac{1}{N}\sum_{n=0}^{N} u^2_n \qquad where \qquad u^2_n = u^2_{xn} + u^2_{y_n} + u^2_{zn} \tag{4.22}$$

2. Results

Overall, the turbulent kinetic energy seems to have a high variability in the cross-shore direction and remains more or less uniform in the longshore direction. A higher TKE is localized offshore of the marsh segments, where the head of the rip current might be located. High turbulent kinetic energy is concentrated in the breaker region and uniformly distributed in the longshore direction as shown in Figure 79. Also, the spacial distribution of the TKE seems to have a line of symmetry off to the side compared to the natural line of symmetry at the centerline of the channel in multiple tests. The measurement at the vertical centerline of the ADV grid was done by a Sontek ADV, whereas the four other ADVs were all from the brand Nortek. No major inconsistencies have been found that would suggest the erroneous data sampling of that single ADV. Generally, in series 200, when the islands are the closest to each other, more TKE is generated. However, when adding the vegetated patches in series 250, the turbulent energy seems to be dissipated by the drag force that the vegetation

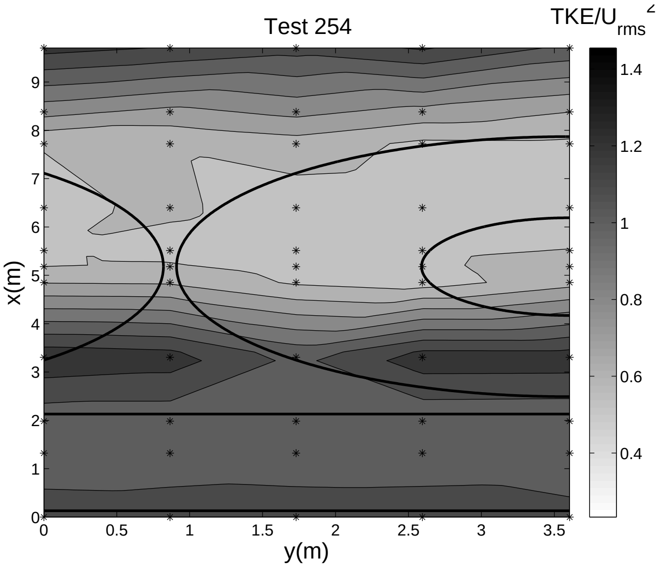

Fig. 79. Contour plot of TKE for Test 254.

stems produce on the waves as shown in Figure 80. Exception is displayed by Test 204 and 254 where the turbulent kinetic energy generated is lower offshore in the non-vegetated case.

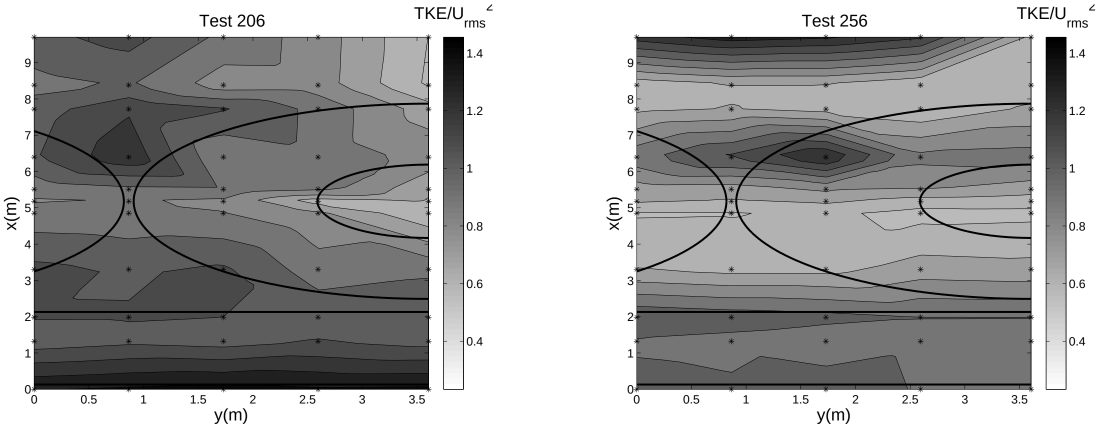

Fig. 80. Contour plot of TKE for Tests 206 and 256.

3. Summary

The turbulence activity displays high values in the channel and offshore where the rip current exit from the rip channel. The distribution of the TKE is, in most cases, symmetric with respect to the centerline of the channel.

E. Velocity Field Analysis

1. Method

a. Two-dimensional Steady Circulation

Eleven separated arrays of 5 Acoustic Doppler Velocimeters (ADV) were used to measure the generated circulation patterns ($\vec{u} = (u, v, w)$). In this study, only the horizontal components of the velocity vectors will be considered. From the phase averaging method applied to the velocity field, the phase average of the flow was derived allowing to get the averaged velocity field for a complete cycle of the waves. The current vectors were obtained at each phase of the phase averaged cycle. For a 2 s-wave, 100 frames were generated and for a 3 s-wave, 150 frames were generated, corresponding to the number of interpolated points in the phase averaging method. The making of videos using these frames allow to identified flow structures in the channel and on the islands. The time average of the mean flow has been computed in the main channel and compared to the mean flow on the mounds.

2. Results

Contour plots of the time average of the mean flows is shown in Figure 82 for Test 151. From these plots, it is obvious that the mean cross-shore velocity V is much smaller than the mean longshore velocity, U, as U seems to vary in both directions whereas V displays a more uniform spacial variability ranging within -10 and 10 cm/s. The mean velocity U covers a greater range of values with a maximum cross-shore velocity of about 40 cm/s and a minimum value of about -40 cm/s over all the tests. A common feature regarding the mean velocity U in all tests is that the sampled region seems to be separated in two zones. First, in the channel, the mean velocity is

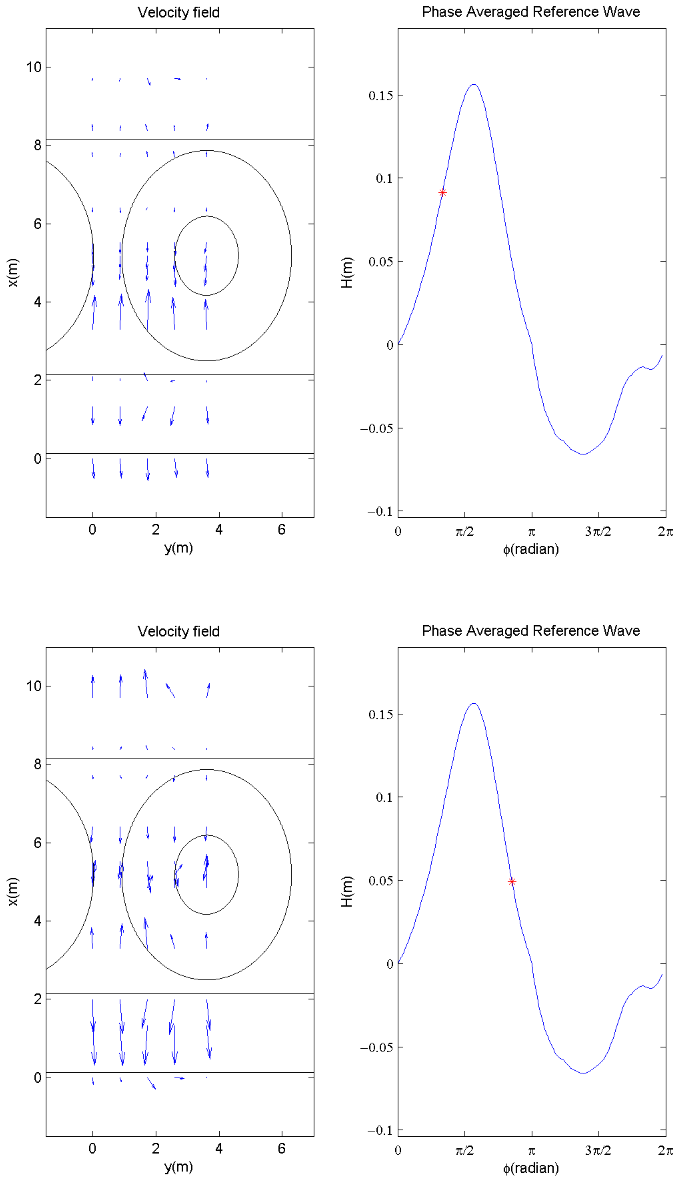

Fig. 81. Phase averages of the horizontal velocity vectors for Test 204 at two distinct phases. The red (∗) corresponds to the phase of the wave measured in radians. The top plot corresponds to frame 26 and the bottom plot corresponds to frame 65.

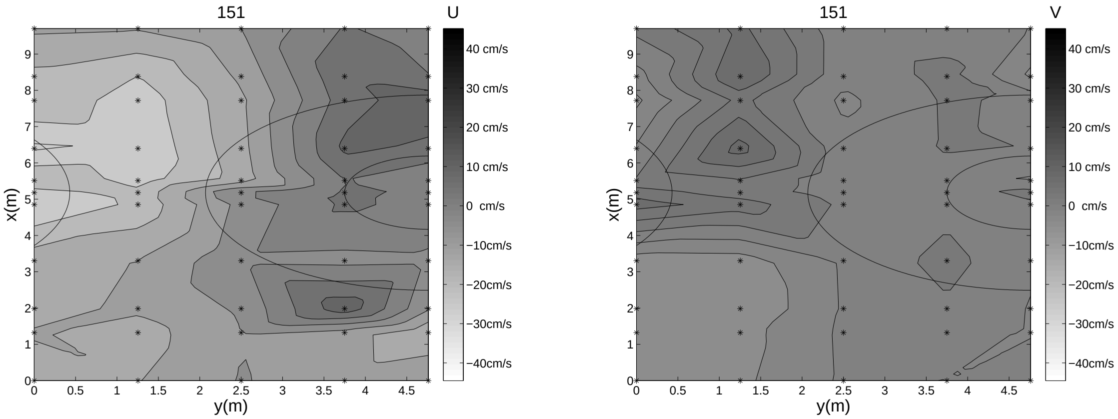

Fig. 82. Contour plots of the mean flow U and V for Test 151.

negative directed toward the offshore part of the basin and second, on the mound, the mean velocity is positive directed toward the rock beach. The highest negativity of the mean velocity is centered at the center of the channel which might be illustrating the presence of a rip strong current flow jetting out of the wetland region, offshore, is shown in Figure 82.

Regarding the variations of the velocity fields with respect to the island spacing, the larger the spacing between the islands, the wider the rip channel is as illustrated in Figure 83. The corresponding vector plots is given if Figure 83. The mean velocity downstream of the marsh is less in the presence of the vegetation patches. Indeed, the presence of the vegetation field adds drag force in the water column decelerating the flow within the vegetation and downstream, nearshore. The reader may be careful looking at the plot of Test 354 in Figure 83 and 84, where the circle markers define interpolated data creating a greater mean velocity with the presence of the vegetation. For a flat mound with no vegetation field on the top, the flow speed increases when

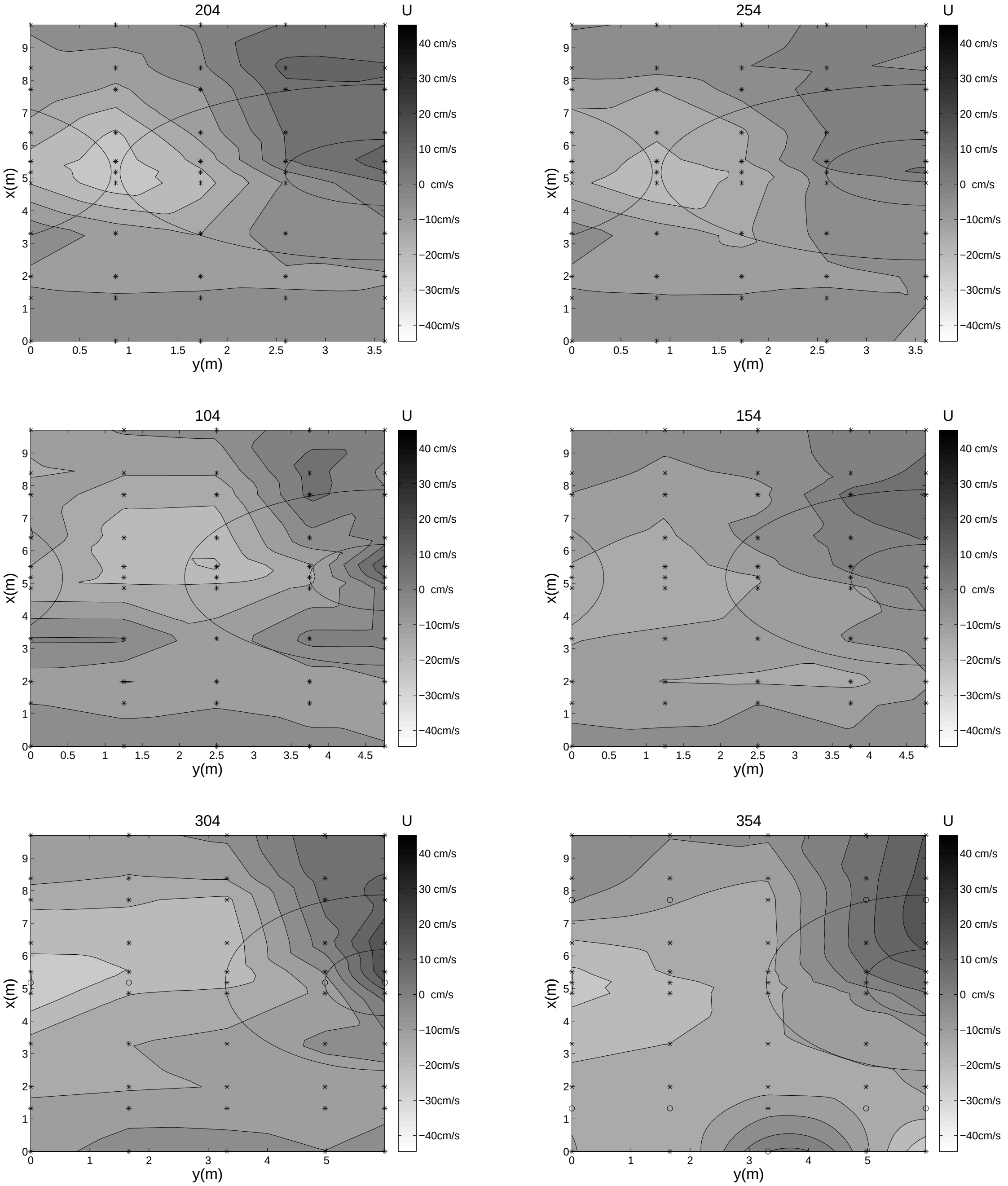

Fig. 83. Contour plots of the mean flow U for case 4.

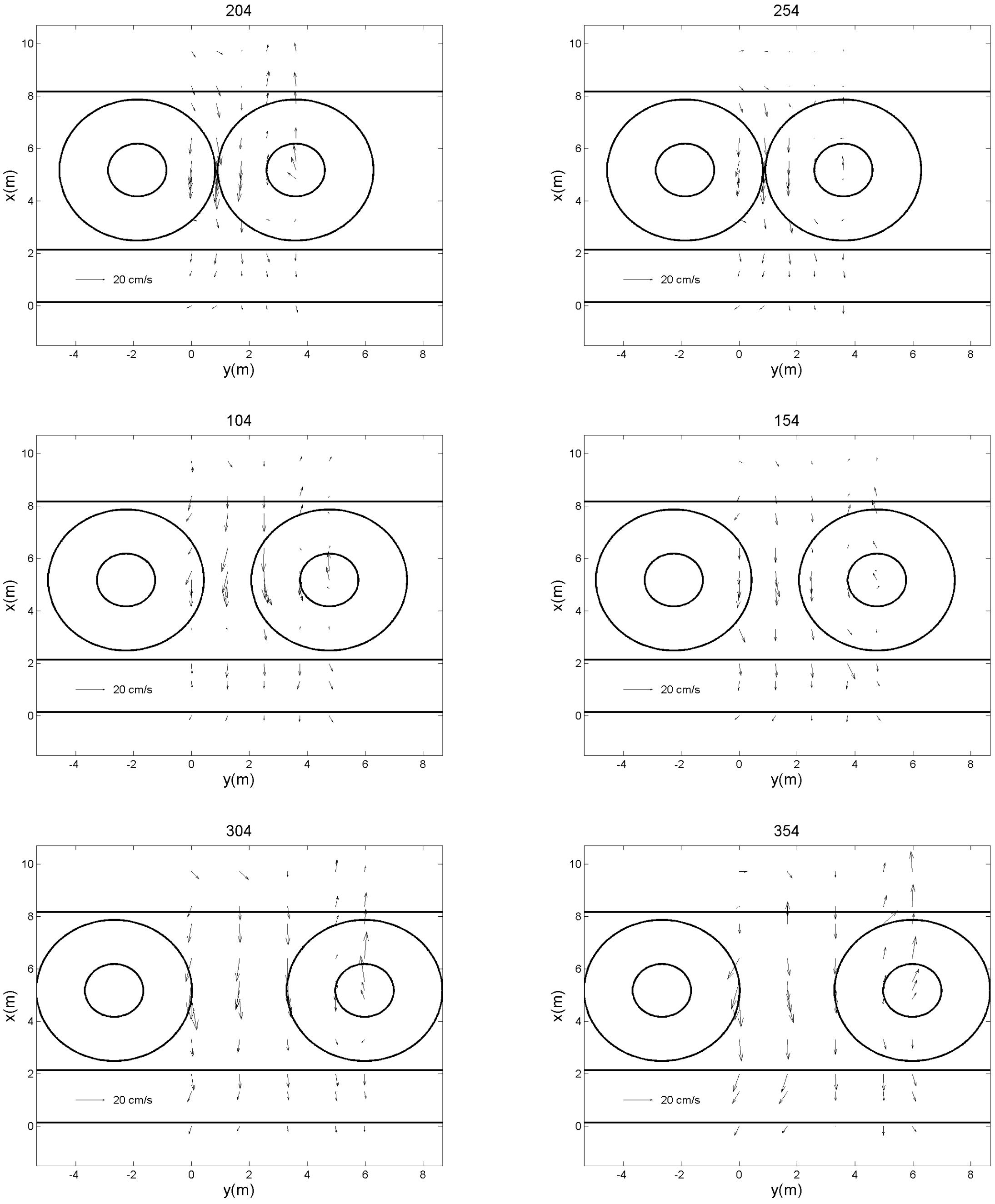

Fig. 84. Vector plots of the mean flow U for case 4.

encountering the negative slope of the back end of the mounds, as no drag force reduces the flow speed. A rip current circulation seems to develop thanks to this particular bathymetry, directing the flow to jet out in the rip channel. However, a deeper look into the longshore directed velocity is needed to figure out how the mean flow is driven toward the rip channel nearshore.

The longshore setup gradient described in Section B.1. of this chapter, induces longshore current as illustrated by the positive values of the longshore velocity in the channel for $x > 6$ m. In contrary, in that same region, the longshore velocity downstream of the mound is negative directed towards the rip channel. Hence, the induced longshore currents converge in the trough and exit offshore. At the center of the rip channel, for 3 m$< x < 6$ m, the longshore velocity weakens allowing the offshore directed current to dominate the flow speed and direction. Offshore of the channel, for $x < 3$ m, the flow seems to exit toward the left side of the channel. The mean velocity at the centerline of the mound shows different characteristics. The presence of the vegetation reduces the magnitudes of the longshore on the top of the vegetation field at shown in Test 254 compared to Test 204. Offshore, for $x < 3$ m, the direction of the velocity is the opposite of the velocity in the channel and is directed towards the right side of the channel as shown by the solid lines in Figure 85.

3. Summary

The velocity field shows the formation of a rip current system where a strong flow is offshore directed in the channel. In contrast, on the top of the mound, the mean horizontal flow is directed into the surfzone. Some vector converging into the channel are noticeable nearshore, where the rip current feeders would be located.

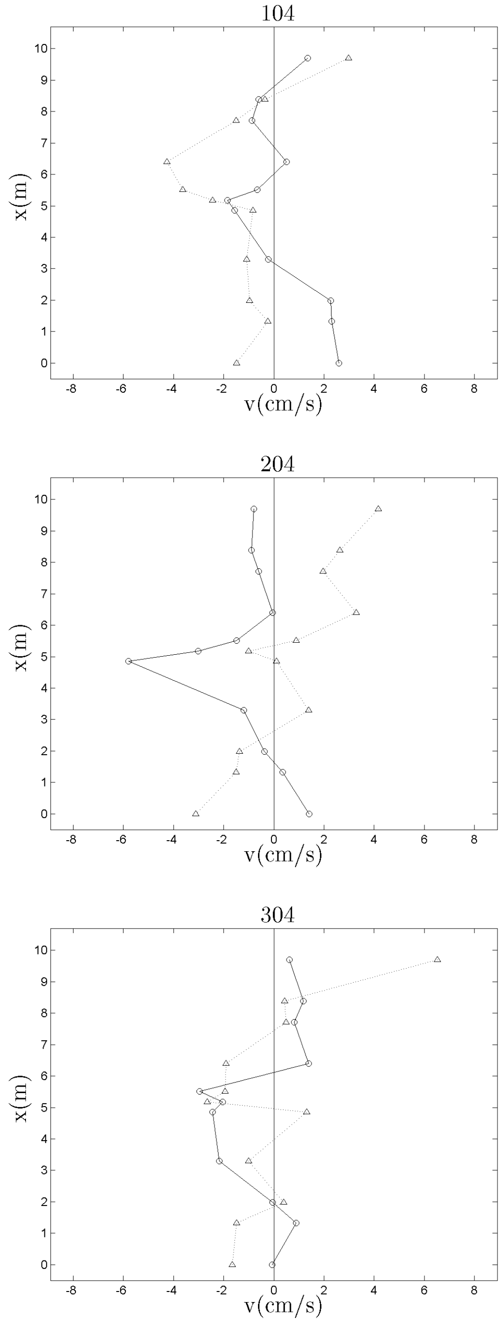

Fig. 85. Cross-shore profiles of longshore current measured in the rip channel (dotted line) and on the centerline of the middle marsh (solid line) for case 4.

F. Preliminary Conclusions

In summary, several parameters have been computed and significant plots have been generated in order to analyze the nearshore circulation in a wetland system. The wave are greatly damped by the vegetation and the presence of the mounds. For most of the tests and the influence of the marsh segment spacing shows interesting behavior as the length between two islands increases or decreases, especially for $L_{seg} = 5.00$ m where a partition of the wave field has been defined.

A relatively strong offshore directed current developed in the channel whereas a current in the opposite direction occurred on the wetland mounds. The offshore directed flow induced a deceleration in the wave propagation in the channel which was clearly noticeable on pictures and videos taken during the experiments, especially in the shallowest water depth tested. As the waves propagate within the vegetation field, the drag force applied in the water column decelerate the waves as well as shown in Figure 52.

The modeled wetland has shown good potential in decelerating and attenuating the waves. The development of a rip current system bringing the nearshore flow offshore through the marsh channel has been detected through the results obtained in the data analysis. The wave-current and the wave-vegetation interactions show an obvious deceleration of the waves in the channel in the shallow water depth tests. Further investigation is needed to verify if these wave patterns occur in deeper water depth.

CHAPTER V

CONCLUSIONS AND RECOMMENDATIONS

A. Conclusions

Series of experiments were conducted in the three-dimensional basin at the Haynes Coastal Engineering Laboratory to assess the influence of wetlands spatial variability on wave hydrodynamics. The combination of vegetated patches with typical wetland mounds was able to reproduce the wave energy dissipation by vegetation. Data from these sets of laboratory experiments on an ideal wetland topography show that the dynamics are dominated by the presence and alternation of the mounds and the rip channels nearshore. The symmetry of the experimental setup is reproduced for the different parameters analyzed, in the contour plots, with the line of symmetry located at the centerline of the channel. The different scenarios of the wave evolution relative to the marsh segment spacing induces wave setup nearshore. Contours of significant wave height demonstrate that the longshore variability of the bathymetry affects the intensity of the damping of the waves behind the islands and in the channel.

The heterogeneity of the topography demonstrated an island-flow relationship which is a function of the island spacing. Indeed, for the largest and the shortest vegetation fields spacing, 6.64 m and 3.46 m respectively, the different contour maps demonstrated a relative high uniformity in the longshore direction whereas the intermediate distance, 5.00 m, exhibits a local elevation of wave height and the contours of mean-water-level in the channel. This important fact could be part of the evidence of a rip current circulation occurring, and directing the mass of water nearshore to exit offshore. The value of the velocity components shows that the total velocity is dominated by higher a cross-shore velocity. The plots of the vector fields agree with this theory showing in most cases, a current flow directed toward the rock beach on the center island, and offshore in the channel. The turbulent kinetic energy contour plots attest of a higher turbulent activity offshore in the channel, where the rip current head should be located. Wave deceleration is detected in the presence of the marsh in most cases, inducing a greater phase lag in the presence of vegetation. The potential of wetlands in reducing storm surge damages on the coast shows promising results and further work is needed to have a complete understanding of the data collected and of the analysis done.

B. Recommendations

Recommendations for future research are focused on continuing and improving the data analysis for the important amount of data gathered during these experiments. The data interpretation will allow to confirm or rectify the developed theory throughout the accomplishment of this thesis. Ideas for future work based on the scope of this study are the following:

- Comprehend data inconsistencies.
- Perfect the data where improvement in the quality is needed.
- Analyze the flow structure displays by the vector fields.
- Evaluate the intensity of the wave attenuation by vegetation in the experiment.
- Correlate the influence of the combined effects of the vegetation field and the spacing between the marsh.
- Use these data to develop a numerical model to reproduce the wave transformation and flow dynamic in variable wetland topography.

- Investigate the potential of the implementation of wetland design in storm damage reduction.
- Estimate the feasibility in real wetland restoration projects.
- Develop a numerical model and use these data for verification.

REFERENCES

Asano, T. (2006), "Wave attenuation and sediment deposition due to coastal vegetation," *J. Global Environ. Eng.,* 11, 29–44.

Asano, T., Matsumoto, S. & Kikuchu, S. (2005), "Wave deformations in vegetation in fringed channels," *Proc., 29th International Conference of Coastal Engineering,* Lisbon, Portugal, 1, 218–229.

Dalrymple, R., Kirby, J. & Hwang, P. (1984), "Wave diffraction due to areas of energy dissipation," *J. Wtrway., Port, Coast., and Ocean Eng.,* 110(1), 67–79.

Dean, G. & Dalrymple, R. (1984), *Water wave mechanics for engineers and scientists*, World Scientific, Singapore, 2, 41–130.

D'Errico, J. (2004), "inpaint_nans.m: Interpolate NaN elements in a 2D array using non-NaN elements," *MATLAB Central File Exchange.* Available at http://www.mathworks.com/, retrieved April 19th, 2011.

Dubi, A. & Torum, A. (1995), "Wave damping by kelp vegetation," *Proc., 24th Coastal Engineering Conference,* Kobe, Japan, 142–156.

Folkard, A. (2005), "Hydrodynamics of model Posidonia Oceanica patches in shallow water," *Limnol. Oceanogr.,* 50(5), 1592–1600.

Ghisalberti, M. & Nepf, H. M. (2006), "The structure of the shear layer in flows over rigid and flexible canopies," *Environ. Fluid Mech.,* 6(3), 277–301.

Ghisalberti, M. & Nepf, H. M. (2009), "Shallow flows over a permeable medium: the hydrodynamics of submerged aquatic canopies," *Transport Porous Med.,* 78(2), 309–326.

Goring, D. & Nikora, V. (2002), "Despiking acoustic doppler velocimeter data," *J. Hydraul. Eng.,* 128(1), 117–126.

Haller, M. & Dalrymple, R. (2001), "Rip current instabilities," *J. Fluid Mech.,* 433(1), 161–192.

Haller, M. C., Dalrymple, R. A. & Svendsen, I. (1997), "Experimental modeling of a rip current system," *Proc., 3rd International Symposium on Ocean Wave Measurement and Analysis*, Virginia Beach, VA, 750–764.

Haller, M. C., Dalrymple, R. A. & Svendsen, I. (2000), "Experiments on rip currents and nearshore circulation: Data report," Center for Applied Coastal Research, University of Delaware, Newark.

Haller, M. C., Dalrymple, R. A. & Svendsen, I. (2002), "Experimental study of nearshore dynamics on a barred beach with rip channels," *J. Geophys. Res.,* 107(C6), 14–1 – 14–21.

HDR, Inc. (2009), "Recovery act: Restoring estuarine habitat in West Galveston Bay," CEPRA Project No.1483 (Document provided by the company).

Kobayashi, N., Raichle, A. W. & Asano, T. (1993), "Wave attenuation by vegetation," *J. Wtrway., Port, Coast., and Ocean Eng.,* 119(1), 30–48.

Lovas, S. & Torum, A. (2001), "Effect of the kelp *Laminaria hyperborea* upon sand dune erosion and water particle velocities," *Coastal Eng. J.,* 44, 37–63.

Lovstedt, C. (2010), "Wave damping in reed: Field measurements and mathematical modeling," *J. Hydraul. Eng.,* 136(4), 222–233.

Mei, C. C. (1983), *The applied dynamics of ocean surface waves*, World Scientific, Wiley, New York.

Mendez, F. J. & Losada, I. J. (1999), "Hydrodynamics induced by wind waves in a vegetation field," *J. Geophys. Res.,* 104(C8), 18383–18396.

Mendez, F. J. & Losada, I. J. (2003), "An empirical model to estimate the propagation of random breaking and nonbreaking waves over vegetation fields," *Coastal Eng. J.,* 51(2), 103–118.

Minello, T. J. (2000), "Temporal development of salt marsh value for nekton and epifauna: Utilization of dredged material marshes in Galveston Bay, Texas, USA," *Wetl. Ecol. Manag.,* 8, 327–341.

Nepf, H. (1999), "Drag, turbulence, and diffusion in flow through emergent vegetation," *Water Resour. Res.,* 35(2), 479–489.

Nepf, H. (2004), "Vegetated flow dynamics," *The ecogeomorphology of tidal marshes*, S. Fagherazzi, M. Marani and L. K. Blum, Washington, D.C., 137–163.

Nepf, H. & Koch, E. (1999), "Effects of emergent vegetation on lateral diffusion in wetlands," *Limnol. Oceanogr.,* 44(4), 1072–1080.

Stephenson, K., Miller, A. & Herron, N. (2003), "Texas treasures: Wetlands," Texas Parks and Wildlife Department, Texas.

White, B. L. & Nepf, H. M. (2008), "A vortex-based model of velocity and shear stress in a partially vegetated shallow channel," *Water Resour. Res.,* 44.

Yamagishi, M., Togano, T. & Tashiro, S. (2007), "Phase averaging analysis of the unsteady velocity profiles in the separation flow on the flat plate," *J. Env. Eng.,* 2(4), 667–680.

APPENDIX A

LOCATION OF WAVE GAUGES AND ADVS

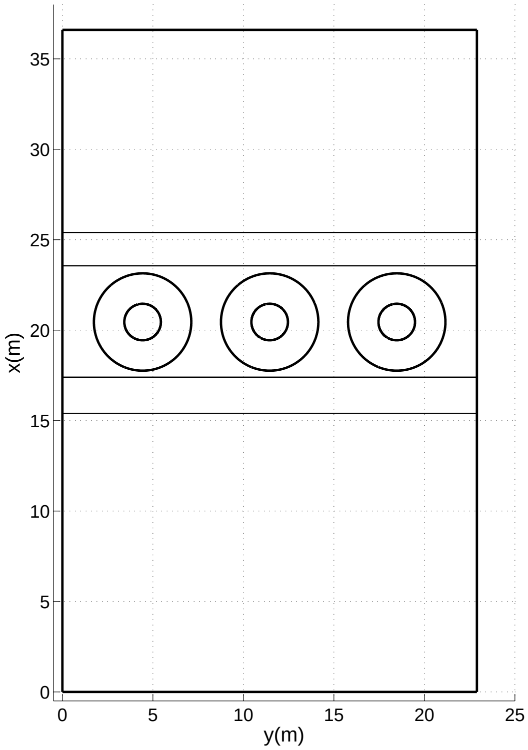

Fig. 86. Plane view of the experimental basin and reference coordinate system. The wavemaker is located at $x = 0$ m.

Table 17. Location of wave gauges during Test 100 from station 1 to 4. St. = station number, x, y are cross-shore and longshore distances in the fixed local coordinate system. All distances measured in meters.

Test 100		gauge #																	
St.		01	02	03	04	05	06	07	08	09	10	11	12	13	14	15	16	17	18
01	x:	25.3	25.3	25.3	25.3	25.3	25.3	25.3	24.6	24.6	24.6	24.6	24.0	24.0	24.0	24.0	24.0	24.0	24.0
	y:	4.4	5.4	6.7	7.9	9.2	10.4	11.5	7.3	8.6	9.8	10.9	4.4	5.4	6.7	7.9	9.2	10.4	11.5
02	x:	24.0	24.0	24.0	24.0	24.0	24.0	24.0	23.3	23.3	23.3	23.3	22.7	22.7	22.7	22.7	22.7	22.7	22.7
	y:	4.4	5.4	6.7	7.9	9.2	10.4	11.5	7.3	8.6	9.8	10.9	4.4	5.4	6.7	7.9	9.2	10.4	11.5
03	x:	23.3	23.3	23.3	23.3	23.3	23.3	23.3	22.7	22.7	22.7	22.7	22.0	22.0	22.0	22.0	22.0	22.0	22.0
	y:	4.4	5.4	6.7	7.9	9.2	10.4	11.5	7.3	8.6	9.8	10.9	4.4	5.4	6.7	7.9	9.2	10.4	11.5
04	x:	22.0	22.0	22.0	22.0	22.0	22.0	22.0	21.3	21.3	21.3	21.3	20.7	20.7	20.7	20.7	20.7	20.7	20.7
	y:	4.4	5.4	6.7	7.9	9.2	10.4	11.5	7.3	8.6	9.8	10.9	4.4	5.4	6.7	7.9	9.2	10.4	11.5

Table 18. Location of wave gauges during Test 100 from station 5 to 8. St. = station number, x, y are cross-shore and longshore distances in the fixed local coordinate system. All distances measured in meters.

Test 100		gauge #																	
St.		01	02	03	04	05	06	07	08	09	10	11	12	13	14	15	16	17	18
05	x:	21.1	21.1	21.1	21.1	21.1	21.1	21.1	20.5	20.5	20.5	20.5	19.8	19.8	19.8	19.8	19.8	19.8	19.8
	y:	4.4	5.4	6.7	7.9	9.2	10.4	11.5	7.3	8.6	9.8	10.9	4.4	5.4	6.7	7.9	9.2	10.4	11.5
06	x:	20.8	20.8	20.8	20.8	20.8	20.8	20.8	20.1	20.1	20.1	20.1	19.5	19.5	19.5	19.5	19.5	19.5	19.5
	y:	4.4	5.4	6.7	7.9	9.2	10.4	11.5	7.3	8.6	9.8	10.9	4.4	5.4	6.7	7.9	9.2	10.4	11.5
07	x:	20.5	20.5	20.5	20.5	20.5	20.5	20.5	19.8	19.8	19.8	19.8	19.1	19.1	19.1	19.1	19.1	19.1	19.1
	y:	4.4	5.4	6.7	7.9	9.2	10.4	11.5	7.3	8.6	9.8	10.9	4.4	5.4	6.7	7.9	9.2	10.4	11.5
08	x:	18.9	18.9	18.9	18.9	18.9	18.9	18.9	18.2	18.2	18.2	18.2	17.6	17.6	17.6	17.6	17.6	17.6	17.6
	y:	4.4	5.4	6.7	7.9	9.2	10.4	11.5	7.3	8.6	9.8	10.9	4.4	5.4	6.7	7.9	9.2	10.4	11.5

Table 19. Location of wave gauges during Test 100 from station 9 to 11. St. = station number, x, y are cross-shore and longshore distances in the fixed local coordinate system. All distances measured in meters.

Test 100		gauge #																	
St.		01	02	03	04	05	06	07	08	09	10	11	12	13	14	15	16	17	18
09	x:	17.6	17.6	17.6	17.6	17.6	17.6	17.6	16.9	16.9	16.9	16.9	16.3	16.3	16.3	16.3	16.3	16.3	16.3
	y:	4.4	5.4	6.7	7.9	9.2	10.4	11.5	7.3	8.6	9.8	10.9	4.4	5.4	6.7	7.9	9.2	10.4	11.5
10	x:	19.2	19.2	19.2	19.2	19.2	19.2	19.2	16.3	16.3	16.3	16.3	15.6	15.6	15.6	15.6	15.6	15.6	15.6
	y:	4.4	5.4	6.7	7.9	9.2	10.4	11.5	7.3	8.6	9.8	10.9	4.4	5.4	6.7	7.9	9.2	10.4	11.5
11	x:	15.6	15.6	15.6	15.6	15.6	15.6	15.6	14.9	14.9	14.9	14.9	14.3	14.3	14.3	14.3	14.3	14.3	14.3
	y:	4.4	5.4	6.7	7.9	9.2	10.4	11.5	7.3	8.6	9.8	10.9	4.4	5.4	6.7	7.9	9.2	10.4	11.5

Table 20. Location of wave gauges during Test 200 from station 1 to 4. St. = station number, x, y are cross-shore and longshore distances in the fixed local coordinate system. All distances measured in meters.

Test 200		gauge #																	
St.		01	02	03	04	05	06	07	08	09	10	11	12	13	14	15	16	17	18
01	x:	25.3	25.3	25.3	25.3	25.3	25.3	25.3	24.6	24.6	24.6	24.6	24.0	24.0	24.0	24.0	24.0	24.0	24.0
	y:	6.0	7.0	7.8	8.7	9.6	10.4	11.5	8.3	9.1	10.0	10.9	6.0	7.0	7.8	8.7	9.6	10.4	11.5
02	x:	24.0	24.0	24.0	24.0	24.0	24.0	24.0	23.3	23.3	23.3	23.3	22.7	22.7	22.7	22.7	22.7	22.7	22.7
	y:	6.0	7.0	7.8	8.7	9.6	10.4	11.5	8.3	9.1	10.0	10.9	6.0	7.0	7.8	8.7	9.6	10.4	11.5
03	x:	23.3	23.3	23.3	23.3	23.3	23.3	23.3	22.7	22.7	22.7	22.7	22.0	22.0	22.0	22.0	22.0	22.0	22.0
	y:	6.0	7.0	7.8	8.7	9.6	10.4	11.5	8.3	9.1	10.0	10.9	6.0	7.0	7.8	8.7	9.6	10.4	11.5
04	x:	22.0	22.0	22.0	22.0	22.0	22.0	22.0	21.3	21.3	21.3	21.3	20.7	20.7	20.7	20.7	20.7	20.7	20.7
	y:	6.0	7.0	7.8	8.7	9.6	10.4	11.5	8.3	9.1	10.0	10.9	6.0	7.0	7.8	8.7	9.6	10.4	11.5

Table 21. Location of wave gauges during Test 200 from station 5 to 8. St. = station number, x, y are cross-shore and longshore distances in the fixed local coordinate system. All distances measured in meters.

Test 200		gauge #																	
St.		01	02	03	04	05	06	07	08	09	10	11	12	13	14	15	16	17	18
05	x:	21.1	21.1	21.1	21.1	21.1	21.1	21.1	20.5	20.5	20.5	20.5	19.8	19.8	19.8	19.8	19.8	19.8	19.8
	y:	6.0	7.0	7.8	8.7	9.6	10.4	11.5	8.3	9.1	10.0	10.9	6.0	7.0	7.8	8.7	9.6	10.4	11.5
06	x:	20.8	20.8	20.8	20.8	20.8	20.8	20.8	20.1	20.1	20.1	20.1	19.5	19.5	19.5	19.5	19.5	19.5	19.5
	y:	6.0	7.0	7.8	8.7	9.6	10.4	11.5	8.3	9.1	10.0	10.9	6.0	7.0	7.8	8.7	9.6	10.4	11.5
07	x:	20.5	20.5	20.5	20.5	20.5	20.5	20.5	19.8	19.8	19.8	19.8	19.1	19.1	19.1	19.1	19.1	19.1	19.1
	y:	6.0	7.0	7.8	8.7	9.6	10.4	11.5	8.3	9.1	10.0	10.9	6.0	7.0	7.8	8.7	9.6	10.4	11.5
08	x:	18.9	18.9	18.9	18.9	18.9	18.9	18.9	18.2	18.2	18.2	18.2	17.6	17.6	17.6	17.6	17.6	17.6	17.6
	y:	6.0	7.0	7.8	8.7	9.6	10.4	11.5	8.3	9.1	10.0	10.9	6.0	7.0	7.8	8.7	9.6	10.4	11.5

Table 22. Location of wave gauges during Test 200 from station 9 to 11. St. = station number, x, y are cross-shore and longshore distances in the fixed local coordinate system. All distances measured in meters.

Test 200		gauge #																	
St.		01	02	03	04	05	06	07	08	09	10	11	12	13	14	15	16	17	18
09	x:	17.6	17.6	17.6	17.6	17.6	17.6	17.6	16.9	16.9	16.9	16.9	16.3	16.3	16.3	16.3	16.3	16.3	16.3
	y:	6.0	7.0	7.8	8.7	9.6	10.4	11.5	8.3	9.1	10.0	10.9	6.0	7.0	7.8	8.7	9.6	10.4	11.5
10	x:	19.2	19.2	19.2	19.2	19.2	19.2	19.2	16.3	16.3	16.3	16.3	15.6	15.6	15.6	15.6	15.6	15.6	15.6
	y:	6.0	7.0	7.8	8.7	9.6	10.4	11.5	8.3	9.1	10.0	10.9	6.0	7.0	7.8	8.7	9.6	10.4	11.5
11	x:	15.6	15.6	15.6	15.6	15.6	15.6	15.6	14.9	14.9	14.9	14.9	14.3	14.3	14.3	14.3	14.3	14.3	14.3
	y:	6.0	7.0	7.8	8.7	9.6	10.4	11.5	8.3	9.1	10.0	10.9	6.0	7.0	7.8	8.7	9.6	10.4	11.5

Table 23. Location of wave gauges during Test 300 from station 1 to 4. St. = station number, x, y are cross-shore and longshore distances in the fixed local coordinate system. All distances measured in meters.

Test 300		gauge #																	
St.		01	02	03	04	05	06	07	08	09	10	11	12	13	14	15	16	17	18
01	x:	25.3	25.3	25.3	25.3	25.3	25.3	25.3	24.6	24.6	24.6	24.6	24.0	24.0	24.0	24.0	24.0	24.0	24.0
	y:	2.8	3.8	5.5	7.1	8.8	10.4	11.5	6.3	7.8	9.6	10.9	2.8	3.8	5.5	7.1	8.8	10.4	11.5
02	x:	24.0	24.0	24.0	24.0	24.0	24.0	24.0	23.3	23.3	23.3	23.3	22.7	22.7	22.7	22.7	22.7	22.7	22.7
	y:	2.8	3.8	5.5	7.1	8.8	10.4	11.5	6.3	7.8	9.6	10.9	2.8	3.8	5.5	7.1	8.8	10.4	11.5
03	x:	23.3	23.3	23.3	23.3	23.3	23.3	23.3	22.7	22.7	22.7	22.7	22.0	22.0	22.0	22.0	22.0	22.0	22.0
	y:	2.8	3.8	5.5	7.1	8.8	10.4	11.5	6.3	7.8	9.6	10.9	2.8	3.8	5.5	7.1	8.8	10.4	11.5
04	x:	22.0	22.0	22.0	22.0	22.0	22.0	22.0	21.3	21.3	21.3	21.3	20.7	20.7	20.7	20.7	20.7	20.7	20.7
	y:	2.8	3.8	5.5	7.1	8.8	10.4	11.5	6.3	7.8	9.6	10.9	2.8	3.8	5.5	7.1	8.8	10.4	11.5

Table 24. Location of wave gauges during Test 300 from station 5 to 8. St. = station number, x, y are cross-shore and longshore distances in the fixed local coordinate system. All distances measured in meters.

Test 300		gauge #																	
St.		01	02	03	04	05	06	07	08	09	10	11	12	13	14	15	16	17	18
05	x:	21.1	21.1	21.1	21.1	21.1	21.1	21.1	20.5	20.5	20.5	20.5	19.8	19.8	19.8	19.8	19.8	19.8	19.8
	y:	2.8	3.8	5.5	7.1	8.8	10.4	11.5	6.3	7.8	9.6	10.9	2.8	3.8	5.5	7.1	8.8	10.4	11.5
06	x:	20.8	20.8	20.8	20.8	20.8	20.8	20.8	20.1	20.1	20.1	20.1	19.5	19.5	19.5	19.5	19.5	19.5	19.5
	y:	2.8	3.8	5.5	7.1	8.8	10.4	11.5	6.3	7.8	9.6	10.9	2.8	3.8	5.5	7.1	8.8	10.4	11.5
07	x:	20.5	20.5	20.5	20.5	20.5	20.5	20.5	19.8	19.8	19.8	19.8	19.1	19.1	19.1	19.1	19.1	19.1	19.1
	y:	2.8	3.8	5.5	7.1	8.8	10.4	11.5	6.3	7.8	9.6	10.9	2.8	3.8	5.5	7.1	8.8	10.4	11.5
08	x:	18.9	18.9	18.9	18.9	18.9	18.9	18.9	18.2	18.2	18.2	18.2	17.6	17.6	17.6	17.6	17.6	17.6	17.6
	y:	2.8	3.8	5.5	7.1	8.8	10.4	11.5	6.3	7.8	9.6	10.9	2.8	3.8	5.5	7.1	8.8	10.4	11.5

Table 25. Location of wave gauges during Test 300 from station 9 to 11. St. = station number, x, y are cross-shore and longshore distances in the fixed local coordinate system. All distances measured in meters.

Test 300		gauge #																	
St.		01	02	03	04	05	06	07	08	09	10	11	12	13	14	15	16	17	18
09	x:	17.6	17.6	17.6	17.6	17.6	17.6	17.6	16.9	16.9	16.9	16.9	16.3	16.3	16.3	16.3	16.3	16.3	16.3
	y:	2.8	3.8	5.5	7.1	8.8	10.4	11.5	6.3	7.8	9.6	10.9	2.8	3.8	5.5	7.1	8.8	10.4	11.5
10	x:	19.2	19.2	19.2	19.2	19.2	19.2	19.2	16.3	16.3	16.3	16.3	15.6	15.6	15.6	15.6	15.6	15.6	15.6
	y:	2.8	3.8	5.5	7.1	8.8	10.4	11.5	6.3	7.8	9.6	10.9	2.8	3.8	5.5	7.1	8.8	10.4	11.5
11	x:	15.6	15.6	15.6	15.6	15.6	15.6	15.6	14.9	14.9	14.9	14.9	14.3	14.3	14.3	14.3	14.3	14.3	14.3
	y:	2.8	3.8	5.5	7.1	8.8	10.4	11.5	6.3	7.8	9.6	10.9	2.8	3.8	5.5	7.1	8.8	10.4	11.5

APPENDIX B

LIST OF DISCARDED WAVE GAUGE AND ADVS TIME SERIES

Table 26. List and classification of discarded time series for Test 101. Npts = number of points in the truncated time series. O = Over-spiked, L = Lost, S = Shifted.

Test 101		gauge #																	
Station	Npts	01	02	03	04	05	06	07	08	09	10	11	12	13	14	15	16	17	18
01	8750	-	-	-	-	-	-	-	-	-	-	-	-	-	-	-	-	-	-
02	8750	-	-	-	-	-	-	-	-	-	-	-	-	-	-	-	-	-	-
03	8750	-	-	-	-	-	-	-	-	-	-	-	-	-	-	-	-	-	-
04	8750	-	-	-	-	-	-	-	-	-	-	-	-	-	-	-	-	-	-
05	8750	-	-	-	-	-	-	-	-	-	-	-	-	-	-	-	-	-	-
06	8750	-	-	-	-	-	-	-	-	-	-	-	-	-	-	-	-	-	-
07	8750	-	-	S	-	-	-	-	-	-	-	-	-	-	-	-	-	-	-
08	8750	-	-	-	-	-	-	-	-	-	-	-	-	-	L	-	-	-	-
09	8750	-	-	-	-	-	-	-	-	-	-	-	-	-	-	-	-	-	-
10	8750	-	-	-	-	-	-	-	-	-	-	-	-	-	-	-	-	O	-
11	8750	-	-	-	-	-	-	-	-	-	-	-	-	-	-	-	-	O	-

Table 27. List and classification of discarded time series for Test 102. Npts = number of points in the truncated time series. O = Over-spiked, L = Lost, S = Shifted.

Test 102		gauge #																	
Station	Npts	01	02	03	04	05	06	07	08	09	10	11	12	13	14	15	16	17	18
01	7500	-	-	-	-	-	-	-	-	-	-	-	-	-	-	-	-	-	-
02	7500	-	-	-	-	-	-	-	-	-	-	-	-	-	-	-	-	-	-
03	7500	-	-	-	-	-	-	-	-	-	-	-	-	-	-	-	-	-	-
04	7500	-	-	-	-	-	-	-	S	S	-	-	-	-	-	-	-	-	-
05	7500	-	-	S	-	-	-	-	-	-	-	-	-	-	-	-	-	-	-
06	7500	-	-	S	-	-	S	-	-	-	S	-	-	-	-	-	-	-	-
07	7500	-	-	S	-	-	-	-	-	-	-	-	-	-	-	-	-	S	-
08	7500	-	-	-	-	-	-	-	-	-	-	-	-	-	-	-	-	O	-
09	7500	-	-	-	-	-	-	-	-	-	-	-	-	-	-	-	-	O	-
10	7500	-	-	-	-	-	-	-	-	-	-	-	-	-	-	-	-	O	-
11	7500	-	-	-	-	-	-	-	-	-	-	-	-	-	-	-	-	O	-

Table 28. List and classification of discarded time series for Test 103. Npts = number of points in the truncated time series. O = Over-spiked, L = Lost, S = Shifted.

Test 103		gauge #																	
Station	Npts	01	02	03	04	05	06	07	08	09	10	11	12	13	14	15	16	17	18
01	7500	-	-	-	-	-	-	-	-	-	-	-	-	-	-	-	-	O	-
02	7500	-	-	-	-	-	-	-	-	-	-	-	-	-	-	-	-	O	-
03	7500	-	-	-	-	-	-	-	-	-	-	-	-	-	-	-	-	O	-
04	7500	-	-	-	-	-	-	-	-	-	-	-	-	-	-	-	-	O	-
05	7500	-	-	-	-	-	-	-	-	-	-	-	-	-	-	-	-	O	-
06	7500	-	-	-	-	-	-	-	-	-	-	-	-	-	-	-	-	O	-
07	7500	-	-	-	-	-	-	-	-	-	-	-	-	-	-	-	-	O	-
08	7500	-	-	-	-	-	-	-	-	-	-	-	-	-	-	-	-	O	-
09	7500	-	-	-	-	-	-	-	-	-	-	-	-	-	-	-	-	O	-
10	7500	-	-	-	-	-	-	-	-	-	-	-	-	-	-	-	-	O	-
11	7500	-	-	-	-	-	-	-	-	-	-	-	-	-	-	-	-	O	-

Table 29. List and classification of discarded time series for Test 104. Npts = number of points in the truncated time series. O = Over-spiked, L = Lost, S = Shifted.

Test 104		gauge #																	
Station	Npts	01	02	03	04	05	06	07	08	09	10	11	12	13	14	15	16	17	18
01	8750	-	-	-	-	-	-	-	-	-	-	-	-	-	-	-	-	O	-
02	8750	-	-	-	-	-	-	-	-	-	-	-	-	-	-	-	-	O	-
03	8750	-	-	-	-	-	-	-	S	-	-	-	-	-	-	-	-	O	-
04	8750	-	-	-	-	-	-	-	-	-	-	-	-	-	-	-	-	O	-
05	8750	-	-	-	-	-	-	-	-	-	-	-	-	-	-	-	-	O	-
06	8750	-	-	-	-	-	-	-	-	-	-	-	-	-	-	-	-	O	-
07	8750	-	-	-	-	-	-	-	-	-	-	-	-	-	-	-	-	O	-
08	8750	-	-	-	-	-	-	-	-	-	-	-	-	-	-	-	-	O	-
09	8750	-	-	-	-	-	-	-	-	-	-	-	-	-	-	-	-	O	-
10	8750	-	-	-	-	-	-	-	-	-	-	-	-	-	-	-	-	O	-
11	8750	-	-	-	-	-	-	-	-	-	-	-	-	-	-	-	-	O	-

Table 30. List and classification of discarded time series for Test 105. Npts = number of points in the truncated time series. O = Over-spiked, L = Lost, S = Shifted.

Test 105		gauge #																	
Station	Npts	01	02	03	04	05	06	07	08	09	10	11	12	13	14	15	16	17	18
01	7500	-	-	-	-	-	-	-	-	-	-	-	-	-	-	-	-	-	-
02	7500	-	-	-	-	-	-	-	-	-	-	-	-	-	-	-	-	-	-
03	7500	-	-	-	-	-	-	-	-	-	-	-	-	-	-	-	-	-	-
04	7500	-	-	-	-	-	-	-	-	-	-	-	-	-	-	-	-	-	-
05	7500	-	-	-	-	-	-	-	-	-	-	-	-	-	-	-	-	-	-
06	7500	-	-	-	-	-	-	-	-	-	-	-	-	-	-	-	-	-	-
07	7500	-	-	-	-	-	-	-	-	-	-	-	-	-	-	-	-	-	-
08	7500	-	-	-	-	-	-	-	-	-	-	-	-	-	-	-	-	-	-
09	7500	-	-	-	-	-	-	-	-	-	-	-	-	-	-	-	-	-	-
10	7500	-	-	-	-	-	-	-	-	-	-	-	-	-	-	-	-	-	-
11	7500	-	-	-	-	-	-	-	-	-	-	-	-	-	-	-	-	-	-

Table 31. List and classification of discarded time series for Test 106. Npts = number of points in the truncated time series. O = Over-spiked, L = Lost, S = Shifted.

Test 106		gauge #																	
Station	Npts	01	02	03	04	05	06	07	08	09	10	11	12	13	14	15	16	17	18
01	7500	-	-	-	-	-	-	-	-	-	-	-	-	-	-	-	-	O	-
02	7500	-	-	-	-	-	-	-	-	-	-	-	-	-	-	-	-	-	-
03	7500	-	-	-	-	-	-	-	-	-	-	-	-	-	-	-	-	-	-
04	7500	-	-	-	-	-	-	-	-	-	-	-	-	-	-	-	-	-	-
05	7500	-	-	-	-	-	-	-	-	-	-	-	-	-	-	-	-	-	-
06	7500	-	-	-	-	-	-	-	-	-	-	-	-	-	-	-	-	-	-
07	7500	-	-	-	-	-	-	-	-	-	-	-	-	-	-	-	-	-	-
08	7500	-	-	-	-	-	-	-	-	-	-	-	-	-	-	-	-	-	-
09	7500	-	-	-	-	-	-	-	-	-	-	-	-	-	-	-	-	-	-
10	7500	-	-	-	-	-	-	-	-	-	-	-	-	-	-	-	-	-	-
11	7500	-	-	-	-	-	-	-	-	-	-	-	-	-	-	-	-	-	-

Table 32. List and classification of discarded time series for Test 151. Npts = number of points in the truncated time series. O = Over-spiked, L = Lost, S = Shifted.

Test 151		gauge #																	
Station	Npts	01	02	03	04	05	06	07	08	09	10	11	12	13	14	15	16	17	18
01	7500	-	-	-	S	-	-	-	-	-	-	-	-	-	-	-	-	L	-
02	7500	-	-	-	-	-	-	-	-	-	-	-	-	-	-	-	-	O	-
03	7500	-	-	-	-	-	-	-	-	-	-	-	-	-	-	O	-	O	-
04	7500	-	-	S	-	-	-	-	-	-	-	-	-	-	-	-	-	O	-
05	7500	-	-	-	-	-	-	-	-	-	-	-	-	-	-	-	-	O	-
06	7500	-	-	-	-	-	-	-	-	-	-	-	-	-	-	-	-	O	-
07	7500	-	-	S	-	-	-	-	-	-	-	-	-	-	-	-	-	O	-
08	7500	-	-	-	-	-	-	-	-	-	-	-	-	-	-	-	-	O	-
09	7500	-	-	-	-	-	-	-	-	-	-	-	-	-	-	-	-	O	-
10	7500	-	-	-	-	-	-	-	-	-	-	-	-	-	-	-	-	O	-
11	7500	-	-	-	-	-	-	-	-	-	-	-	-	-	-	-	-	O	-

Table 33. List and classification of discarded time series for Test 152. Npts = number of points in the truncated time series. O = Over-spiked, L = Lost, S = Shifted.

Test 152		gauge #																	
Station	Npts	01	02	03	04	05	06	07	08	09	10	11	12	13	14	15	16	17	18
01	7500	-	-	-	-	-	-	-	-	-	-	-	-	-	-	-	O	-	-
02	7500	-	-	-	-	-	-	-	-	-	-	-	-	-	-	-	-	O	-
03	7500	-	-	-	-	-	-	-	-	-	-	-	-	-	-	-	-	O	-
04	7500	-	-	-	-	-	-	-	-	-	-	-	-	-	-	-	-	O	-
05	7500	-	-	-	-	-	-	-	-	-	-	-	-	-	O	O	-	O	-
06	7500	-	-	-	-	-	-	-	-	-	-	-	-	O	O	-	O	-	-
07	7500	-	-	-	-	-	-	-	-	-	-	-	-	-	O	O	-	O	-
08	7500	-	-	-	-	-	-	-	-	-	-	-	-	-	-	-	-	O	-
09	7500	-	-	-	-	-	-	-	-	-	-	-	-	-	-	-	-	O	-
10	7500	-	-	-	-	-	-	-	-	-	-	-	-	-	-	-	-	O	-
11	7500	-	-	-	-	-	-	-	-	-	-	-	-	-	-	-	-	O	-

Table 34. List and classification of discarded time series for Test 153. Npts = number of points in the truncated time series. O = Over-spiked, L = Lost, S = Shifted.

Test 153		gauge #																	
Station	Npts	01	02	03	04	05	06	07	08	09	10	11	12	13	14	15	16	17	18
01	8250	-	-	-	-	-	-	-	-	-	-	-	-	-	-	-	-	O	-
02	8250	-	-	-	-	-	-	-	-	-	-	-	-	-	-	-	-	O	-
03	8250	-	-	-	-	-	-	-	-	-	-	-	-	-	-	-	-	O	-
04	8250	-	-	-	-	-	-	-	-	-	-	-	-	-	-	-	-	O	-
05	8250	-	-	-	-	-	-	-	-	-	-	-	-	-	-	-	-	O	-
06	8250	-	-	-	-	-	-	-	-	-	-	-	-	-	-	-	-	O	-
07	8250	-	-	-	-	-	-	-	-	-	-	-	-	-	-	-	-	O	-
08	8250	-	-	-	-	-	-	-	-	-	-	-	-	-	-	-	-	O	-
09	8250	-	-	-	-	-	-	-	-	-	-	-	-	-	-	-	-	O	-
10	8250	-	-	-	-	-	-	-	-	-	-	-	-	-	-	-	-	O	-
11	8250	-	-	-	-	-	-	-	-	-	-	-	-	-	-	-	-	O	-

Table 35. List and classification of discarded time series for Test 154. Npts = number of points in the truncated time series. O = Over-spiked, L = Lost, S = Shifted.

Test 154		gauge #																	
Station	Npts	01	02	03	04	05	06	07	08	09	10	11	12	13	14	15	16	17	18
01	7500	-	-	-	-	-	-	-	-	-	-	-	-	-	-	-	-	O	-
02	7500	-	-	-	-	-	-	-	-	-	-	-	-	-	-	-	-	O	-
03	7500	-	-	-	-	-	-	-	-	-	-	-	-	-	-	-	-	O	-
04	7500	-	-	-	-	-	-	-	-	-	-	-	-	-	-	-	-	O	-
05	7500	-	-	-	-	-	-	-	-	-	-	-	-	-	-	-	-	O	-
06	7500	-	-	-	-	-	-	-	-	-	-	-	-	-	-	-	-	O	-
07	7500	-	-	-	-	-	-	-	-	-	-	-	-	-	-	-	-	O	-
08	7500	-	-	-	-	-	-	-	-	-	-	-	-	-	-	-	-	O	-
09	7500	-	-	-	-	-	-	-	-	-	-	-	-	-	-	-	-	O	-
10	7500	-	-	-	-	-	-	-	-	-	-	-	-	-	-	-	-	O	-
11	7500	-	-	-	-	-	-	-	-	-	-	-	-	-	-	-	-	O	-

Table 36. List and classification of discarded time series for Test 155. Npts = number of points in the truncated time series. O = Over-spiked, L = Lost, S = Shifted.

Test 155		gauge #																	
Station	Npts	01	02	03	04	05	06	07	08	09	10	11	12	13	14	15	16	17	18
01	7500	-	-	-	-	-	-	-	-	-	-	-	-	-	-	-	-	-	-
02	7500	-	-	-	-	-	-	-	-	-	-	-	-	-	-	-	-	-	-
03	7500	-	-	-	-	-	-	-	-	-	-	-	-	-	-	-	-	-	-
04	7500	-	-	-	-	-	-	-	-	-	-	-	-	-	-	-	-	-	-
05	7500	-	-	-	-	-	-	-	-	-	-	-	-	-	-	-	-	-	-
06	7500	-	-	-	-	-	-	-	-	-	-	-	-	-	-	-	-	-	-
07	7500	-	-	-	-	-	-	-	-	-	-	-	-	-	-	-	-	-	-
08	7500	-	-	-	-	-	-	-	-	-	-	-	-	-	-	-	-	O	-
09	7500	-	-	-	-	-	-	-	-	-	-	-	-	-	-	-	-	O	-
10	7500	-	-	-	-	-	-	-	-	-	-	-	-	-	-	-	-	-	-
11	7500	-	-	-	-	-	-	-	-	-	-	-	-	-	-	-	-	O	-

Table 37. List and classification of discarded time series for Test 156. Npts = number of points in the truncated time series. O = Over-spiked, L = Lost, S = Shifted.

Test 156		gauge #																	
Station	Npts	01	02	03	04	05	06	07	08	09	10	11	12	13	14	15	16	17	18
01	7500	-	-	-	-	-	-	-	-	-	-	-	-	-	-	-	-	-	-
02	7500	-	-	-	-	-	-	-	-	-	-	-	-	-	-	-	O	-	-
03	7500	-	-	-	-	-	-	-	-	-	-	-	-	-	-	-	-	-	-
04	7500	-	-	-	-	-	-	-	-	-	-	-	-	-	-	-	-	-	-
05	7500	-	-	-	-	-	-	-	-	-	-	-	-	-	-	-	-	-	-
06	7500	-	-	-	-	-	-	-	-	-	-	-	-	-	-	-	-	O	-
07	7500	-	-	-	-	-	-	-	-	-	-	-	-	-	-	-	-	-	-
08	7500	-	-	-	-	-	-	-	-	-	-	-	-	-	-	-	-	O	-
09	7500	-	-	-	-	-	-	-	-	-	-	-	-	-	-	-	-	O	-
10	7500	-	-	-	-	-	-	-	-	-	-	-	-	-	-	-	-	O	-
11	7500	-	-	-	-	-	-	-	-	-	-	-	-	-	-	-	-	O	-

Table 38. List and classification of discarded time series for Test 203. Npts = number of points in the truncated time series. O = Over-spiked, L = Lost, S = Shifted.

Test 203		gauge #																	
Station	Npts	01	02	03	04	05	06	07	08	09	10	11	12	13	14	15	16	17	18
01	7500	-	-	-	-	-	-	-	-	-	-	-	-	-	-	-	-	-	-
02	7500	-	-	-	-	-	-	-	-	-	-	-	-	-	-	-	-	-	-
03	7500	-	-	-	-	-	-	-	-	-	-	-	-	-	-	-	-	-	-
04	7500	-	-	-	-	-	-	-	-	-	-	-	-	-	-	-	-	-	-
05	7500	-	-	-	-	-	-	-	-	-	-	-	-	-	-	-	-	-	-
06	7500	-	-	-	-	-	-	-	-	-	-	-	-	-	-	-	-	-	-
07	7500	-	-	-	-	-	-	-	-	-	-	-	-	-	-	-	-	-	-
08	7500	-	-	-	-	-	-	-	-	-	-	-	-	-	-	-	-	-	-
09	7500	-	-	-	-	-	-	-	-	-	-	-	-	-	-	-	-	-	-
10	7500	-	-	-	-	-	-	-	-	-	-	-	-	-	-	-	-	-	-
11	7500	-	-	-	-	-	-	-	-	-	-	-	-	-	-	-	-	-	-

Table 39. List and classification of discarded time series for Test 204. Npts = number of points in the truncated time series. O = Over-spiked, L = Lost, S = Shifted.

Test 204		gauge #																	
Station	Npts	01	02	03	04	05	06	07	08	09	10	11	12	13	14	15	16	17	18
01	7500	-	-	-	-	-	-	-	-	-	-	-	-	-	-	-	-	-	-
02	7500	-	-	-	-	-	-	-	-	-	-	-	-	-	-	-	-	-	-
03	7500	-	-	-	-	-	-	-	-	-	-	-	-	-	-	-	-	-	-
04	7500	-	-	-	-	-	-	-	-	-	-	-	-	-	-	-	-	-	-
05	7500	-	-	-	-	-	-	-	-	-	-	-	-	-	-	-	-	-	-
06	7500	-	-	-	-	-	-	-	-	-	-	-	-	-	-	-	-	-	-
07	7500	-	-	-	-	-	-	-	-	-	-	-	-	-	-	-	-	-	-
08	7500	-	-	-	-	-	-	-	-	-	-	-	-	-	-	-	-	-	-
09	7500	-	-	-	-	-	-	-	-	-	-	-	-	-	-	-	-	-	-
10	7500	-	-	-	-	-	-	-	-	-	-	-	-	-	-	-	-	-	-
11	7500	-	-	-	-	-	-	-	-	-	-	-	-	-	-	-	-	-	-

Table 40. List and classification of discarded time series for Test 205. Npts = number of points in the truncated time series. O = Over-spiked, L = Lost, S = Shifted.

Test 205		gauge #																	
Station	Npts	01	02	03	04	05	06	07	08	09	10	11	12	13	14	15	16	17	18
01	7500	-	-	-	-	-	-	-	-	-	-	-	-	-	-	-	-	-	-
02	7500	-	-	-	-	-	-	-	-	-	-	-	-	-	-	-	-	-	-
03	7500	-	-	-	-	-	-	-	-	-	-	-	-	-	-	-	-	-	-
04	7500	-	-	-	-	-	-	-	-	-	-	-	-	-	-	-	-	-	-
05	7500	-	-	-	-	-	-	-	-	-	-	-	-	-	-	-	-	-	-
06	7500	-	-	-	-	-	-	-	-	-	-	-	-	-	-	-	-	-	-
07	7500	-	-	-	-	-	-	-	-	-	-	-	-	-	-	-	-	-	-
08	7500	-	-	-	-	-	-	-	-	-	-	-	-	-	-	-	-	-	-
09	7500	-	-	-	-	-	-	-	-	-	-	-	-	-	-	-	-	-	-
10	7500	-	-	-	-	-	-	-	-	-	-	-	-	-	-	-	-	-	-
11	7500	-	-	-	-	-	-	-	-	-	-	-	-	-	-	-	-	-	-

Table 41. List and classification of discarded time series for Test 206. Npts = number of points in the truncated time series. O = Over-spiked, L = Lost, S = Shifted.

Test 206		gauge #																	
Station	Npts	01	02	03	04	05	06	07	08	09	10	11	12	13	14	15	16	17	18
01	7250	-	-	-	-	-	-	-	-	-	-	-	-	-	-	-	-	-	-
02	7250	-	-	-	-	-	-	-	-	-	-	-	-	-	-	-	-	-	-
03	7250	-	-	-	-	-	-	-	-	-	-	-	-	-	-	-	-	-	-
04	7250	-	-	-	-	-	-	-	-	-	-	-	-	-	-	-	-	-	-
05	7250	-	-	-	-	-	-	-	-	-	-	-	-	-	-	-	-	-	-
06	7250	-	-	-	-	-	-	-	-	-	-	-	-	-	-	-	-	-	-
07	7250	-	-	-	-	-	-	-	-	-	-	-	-	-	-	-	-	-	-
08	7250	-	-	-	-	-	-	-	-	-	-	-	-	-	-	-	-	-	-
09	7250	-	-	-	-	-	-	-	-	-	-	-	-	-	-	-	-	-	-
10	7250	-	-	-	-	-	-	-	-	-	-	-	-	-	-	-	-	-	-
11	7250	-	-	-	-	-	-	-	-	-	-	-	-	-	-	-	-	-	-

Table 42. List and classification of discarded time series for Test 253. Npts = number of points in the truncated time series. O = Over-spiked, L = Lost, S = Shifted.

Test 253		gauge #																	
Station	Npts	01	02	03	04	05	06	07	08	09	10	11	12	13	14	15	16	17	18
01	7500	-	-	-	-	-	-	-	-	-	-	-	-	-	-	-	-	-	-
02	7500	-	-	-	-	-	-	-	-	-	-	-	-	-	-	-	-	-	-
03	7500	-	-	-	-	-	-	-	-	-	-	-	-	-	-	-	-	-	-
04	7500	-	-	-	-	-	-	-	-	-	-	-	-	-	-	-	-	-	-
05	7500	-	-	-	-	-	-	-	-	-	-	-	-	-	-	-	-	-	-
06	7500	-	-	-	-	-	-	-	-	-	-	-	-	-	-	-	-	-	-
07	7500	-	-	-	-	-	-	-	-	-	-	-	-	-	-	-	-	-	-
08	7500	-	-	-	-	-	-	-	-	-	-	-	-	-	-	-	-	-	-
09	7500	-	-	-	-	-	-	-	-	-	-	-	-	-	-	-	-	-	-
10	7500	-	-	-	-	-	-	-	-	-	-	-	-	-	-	-	-	-	-
11	7500	-	-	-	-	-	-	-	-	-	-	-	-	-	-	-	-	-	-

Table 43. List and classification of discarded time series for Test 254. Npts = number of points in the truncated time series. O = Over-spiked, L = Lost, S = Shifted.

Test 254		gauge #																	
Station	Npts	01	02	03	04	05	06	07	08	09	10	11	12	13	14	15	16	17	18
01	7500	-	-	-	-	-	-	-	-	-	-	-	-	-	-	-	-	-	-
02	7500	-	-	-	-	-	-	-	-	-	-	-	-	-	-	-	-	-	-
03	7500	-	-	-	-	-	-	-	-	-	-	-	-	-	-	-	-	-	-
04	7500	-	-	-	-	-	-	-	-	-	-	-	-	-	-	-	-	-	-
05	7500	-	-	-	-	-	-	-	-	-	-	-	-	-	-	-	-	-	-
06	7500	-	-	-	-	-	-	-	-	-	-	-	-	-	-	-	-	-	-
07	7500	-	-	-	-	-	-	-	-	-	-	-	-	-	-	-	-	-	-
08	7500	-	-	-	-	-	-	-	-	-	-	-	-	-	-	-	-	-	-
09	7500	-	-	-	-	-	-	-	-	-	-	-	-	-	-	-	-	-	-
10	7500	-	-	-	-	-	-	-	-	-	-	-	-	-	-	-	-	-	-
11	7500	-	-	-	-	S	-	-	-	-	-	-	-	-	-	-	-	-	-

Table 44. List and classification of discarded time series for Test 255. Npts = number of points in the truncated time series. O = Over-spiked, L = Lost, S = Shifted.

Test 255		gauge #																	
Station	Npts	01	02	03	04	05	06	07	08	09	10	11	12	13	14	15	16	17	18
01	7500	-	-	-	-	-	-	-	-	-	-	-	-	-	-	-	-	-	-
02	7500	-	-	-	-	-	-	-	-	-	-	-	-	-	-	-	-	-	-
03	-	L	L	L	L	L	L	L	L	L	L	L	L	L	L	L	L	L	L
04	7500	-	-	-	-	-	-	-	-	-	-	-	-	-	-	-	-	-	-
05	7500	-	-	-	-	-	-	-	-	-	-	-	-	-	-	-	-	-	-
06	7500	-	-	-	-	-	-	-	-	-	-	-	-	-	-	-	-	-	-
07	7500	-	-	-	-	-	-	-	-	-	-	-	-	-	-	-	-	-	-
08	7500	-	-	-	-	-	-	-	-	-	-	-	-	-	-	-	-	-	-
09	7500	-	-	-	-	-	-	-	-	-	-	-	-	-	-	-	-	-	-
10	7500	-	-	-	-	-	-	-	-	-	-	-	-	-	-	-	-	-	-
11	7500	-	-	-	-	-	-	-	-	-	-	-	-	-	-	-	-	-	-

Table 45. List and classification of discarded time series for Test 256. Npts = number of points in the truncated time series. O = Over-spiked, L = Lost, S = Shifted.

Test 256		gauge #																	
Station	Npts	01	02	03	04	05	06	07	08	09	10	11	12	13	14	15	16	17	18
01	7500	-	-	-	-	-	-	-	-	-	-	-	-	-	-	-	-	-	-
02	7500	-	-	-	-	-	-	-	-	-	-	-	-	-	-	-	L	-	-
03	7500	-	-	-	-	-	-	-	-	-	-	-	-	-	-	-	-	-	-
04	7500	-	-	-	-	-	-	-	-	-	-	-	-	-	-	-	-	-	-
05	7500	-	-	-	-	-	-	-	-	-	-	-	-	-	-	-	-	-	-
06	7500	-	-	-	-	-	-	-	-	-	-	-	-	-	-	-	-	-	-
07	7500	-	-	-	-	-	-	-	-	-	-	-	-	-	-	-	-	-	-
08	7500	-	-	-	-	-	-	-	-	-	-	-	-	-	-	-	-	-	-
09	7500	-	-	-	-	-	-	-	-	-	-	-	-	-	-	-	-	-	-
10	7500	-	-	-	-	-	-	-	-	-	-	-	-	-	-	-	-	-	-
11	7500	-	-	-	-	-	-	-	-	-	-	-	-	-	-	-	-	-	-

Table 46. List and classification of discarded time series for Test 303. Npts = number of points in the truncated time series. O = Over-spiked, L = Lost, S = Shifted.

Test 303		gauge #																	
Station	Npts	01	02	03	04	05	06	07	08	09	10	11	12	13	14	15	16	17	18
01	7500	-	-	-	-	-	-	-	-	-	-	-	-	-	-	-	-	-	-
02	7500	-	-	-	-	-	-	-	-	-	-	-	-	-	-	-	-	-	-
03	7500	-	-	-	-	-	-	-	-	-	-	-	-	-	-	-	-	-	-
04	7500	-	-	-	-	-	-	-	-	-	-	-	-	-	-	-	-	-	-
05	7500	-	-	-	-	-	-	-	-	-	-	-	-	-	-	-	-	-	-
06	7500	-	-	-	-	-	-	-	-	-	-	-	-	-	-	-	-	-	-
07	7500	-	-	-	-	-	-	-	-	-	-	-	-	-	-	-	-	-	-
08	7500	-	-	-	-	-	-	-	-	-	-	-	-	-	-	-	-	-	-
09	7500	-	-	-	-	-	-	-	-	-	-	-	-	-	-	-	-	-	-
10	7500	-	-	-	-	-	-	-	-	-	-	-	-	-	-	-	-	-	-
11	7500	-	-	-	-	-	-	-	-	-	-	-	-	-	-	-	-	-	-

Table 47. List and classification of discarded time series for Test 304. Npts = number of points in the truncated time series. O = Over-spiked, L = Lost, S = Shifted.

Test 304		gauge #																	
Station	Npts	01	02	03	04	05	06	07	08	09	10	11	12	13	14	15	16	17	18
01	7500	-	-	-	-	-	-	-	-	-	-	-	-	-	-	-	-	-	-
02	7500	-	-	-	-	-	-	-	-	-	-	-	-	-	-	-	-	-	-
03	7500	-	-	-	-	-	-	-	-	-	-	-	-	-	-	-	-	-	-
04	7500	-	-	-	-	-	-	-	-	-	-	-	-	-	-	-	-	-	-
05	7500	-	-	-	-	-	-	-	-	-	-	-	-	-	-	-	-	-	-
06	7500	-	-	-	-	-	-	-	-	-	-	-	-	-	-	-	-	-	-
07	7500	-	-	-	-	-	-	-	-	-	-	-	-	-	-	-	-	-	-
08	7500	-	-	-	-	-	-	-	-	-	-	-	-	-	-	-	-	-	-
09	7500	-	-	-	-	-	-	-	-	-	-	-	-	-	-	-	-	-	-
10	7500	-	-	-	-	-	-	-	-	-	-	-	-	-	O	-	-	-	-
11	7500	-	-	-	-	-	-	-	-	-	-	-	-	-	O	-	-	-	-

Table 48. List and classification of discarded time series for Test 305. Npts = number of points in the truncated time series. O = Over-spiked, L = Lost, S = Shifted.

Test 305		gauge #																	
Station	Npts	01	02	03	04	05	06	07	08	09	10	11	12	13	14	15	16	17	18
01	7500	-	-	-	-	-	-	-	-	-	-	-	-	-	-	-	-	-	-
02	7500	-	-	-	-	-	-	-	-	-	-	-	-	-	-	-	-	-	-
03	-	L	L	L	L	L	L	L	L	L	L	L	L	L	L	L	L	L	L
04	7500	-	-	-	-	-	-	-	-	-	-	-	-	-	-	-	-	-	-
05	7500	-	-	-	-	-	-	-	-	-	-	-	-	-	-	-	-	-	-
06	7500	-	-	-	-	-	-	-	-	-	-	-	-	-	-	-	-	-	-
07	7500	-	-	-	-	-	-	-	-	-	-	-	-	-	-	-	-	-	-
08	7500	-	-	-	-	-	-	-	-	-	-	-	-	-	-	-	-	-	-
09	7500	-	-	-	-	-	-	-	-	-	-	-	-	-	-	-	-	-	-
10	7500	-	-	-	-	-	-	-	-	-	-	-	-	-	-	-	-	-	-
11	7500	-	-	-	-	-	-	-	-	-	-	-	-	-	-	-	-	-	-

Table 49. List and classification of discarded time series for Test 306. Npts = number of points in the truncated time series. O = Over-spiked, L = Lost, S = Shifted.

Test 306		gauge #																	
Station	Npts	01	02	03	04	05	06	07	08	09	10	11	12	13	14	15	16	17	18
01	7500	-	-	-	-	-	-	-	-	-	-	-	-	-	-	-	-	-	-
02	7500	-	-	-	-	-	-	-	-	-	-	-	-	-	-	-	-	-	-
03	7500	-	-	-	-	-	-	-	-	-	-	-	-	-	-	-	-	-	-
04	7500	-	-	-	-	-	-	-	-	-	-	-	-	-	-	-	-	-	-
05	7500	-	-	-	-	-	-	-	-	-	-	-	-	-	-	-	-	-	-
06	7500	-	-	-	-	-	-	-	-	-	-	-	-	-	-	-	-	-	-
07	7500	-	-	-	-	-	-	-	-	-	-	-	-	-	-	-	-	-	-
08	7500	-	-	-	-	-	-	-	-	-	-	-	-	-	-	-	-	-	-
09	7500	-	-	-	-	-	-	-	-	-	-	-	-	-	-	-	-	-	-
10	7500	-	-	-	-	-	-	-	-	-	-	-	-	-	-	-	-	-	-
11	7500	-	-	-	-	-	-	-	-	-	-	-	-	-	-	-	-	-	-

Table 50. List and classification of discarded time series for Test 353. Npts = number of points in the truncated time series. O = Over-spiked, L = Lost, S = Shifted.

Test 353		gauge #																	
Station	Npts	01	02	03	04	05	06	07	08	09	10	11	12	13	14	15	16	17	18
01	7500	-	-	-	-	-	-	-	-	-	-	-	-	-	-	-	-	-	-
02	7500	-	-	-	-	-	-	-	-	-	-	-	-	-	-	-	-	-	-
03	7500	-	-	-	-	-	-	-	-	-	-	-	-	-	-	-	-	-	-
04	7500	-	-	-	-	-	-	-	-	-	-	-	-	-	-	-	-	-	-
05	7500	-	-	-	-	-	-	-	-	-	-	-	-	-	-	-	-	-	-
06	7500	-	-	-	-	-	-	-	-	-	-	-	-	-	-	-	-	-	-
07	7500	-	-	-	-	-	-	-	-	-	-	-	-	-	-	-	-	-	-
08	7500	-	-	-	-	-	-	-	-	-	-	-	-	-	-	-	-	-	-
09	7500	-	-	-	-	-	-	-	-	-	-	-	-	-	-	-	-	-	-
10	7500	-	-	-	-	-	-	-	-	-	-	-	-	-	-	-	-	-	-
11	7500	-	-	-	-	-	-	-	-	-	-	-	-	-	-	-	-	-	-

Table 51. List and classification of discarded time series for Test 354. Npts = number of points in the truncated time series. O = Over-spiked, L = Lost, S = Shifted.

Test 354		gauge #																	
Station	Npts	01	02	03	04	05	06	07	08	09	10	11	12	13	14	15	16	17	18
01	7500	-	-	-	-	-	-	-	-	-	-	-	-	-	-	-	-	-	-
02	7500	-	-	-	-	-	-	-	-	-	-	-	-	-	-	-	-	-	-
03	7500	-	-	-	-	-	-	-	-	-	-	-	-	-	-	-	-	-	-
04	7500	-	-	-	-	-	-	-	-	-	-	-	-	-	-	-	-	-	-
05	7500	-	-	-	-	-	-	-	-	-	-	-	-	L	-	-	-	-	-
06	7500	-	-	-	-	-	-	-	-	-	-	-	-	-	-	-	-	-	-
07	7500	-	-	-	-	-	-	-	-	-	-	-	-	-	-	-	-	-	-
08	7500	-	-	-	-	-	-	-	-	-	-	-	-	-	-	-	-	-	-
09	7500	-	-	-	-	-	-	-	-	-	-	-	-	-	-	-	-	-	-
10	7500	-	-	-	-	-	-	-	-	-	-	-	-	-	-	-	-	-	-
11	7500	-	-	-	-	-	-	-	-	-	-	-	-	-	-	-	-	-	-

Table 52. List and classification of discarded time series for Test 355. Npts = number of points in the truncated time series. O = Over-spiked, L = Lost, S = Shifted.

Test 355		gauge #																	
Station	Npts	01	02	03	04	05	06	07	08	09	10	11	12	13	14	15	16	17	18
01	7500	-	-	-	-	-	-	-	-	-	-	-	-	-	-	-	-	-	-
02	7500	-	-	-	-	-	-	-	-	-	-	-	-	-	-	-	-	-	-
03	7500	-	-	-	-	-	-	-	-	-	-	-	-	-	-	-	-	O	-
04	7500	-	-	-	-	-	-	-	-	-	-	-	-	-	-	-	-	-	-
05	7500	-	-	-	-	-	-	-	-	-	-	-	-	-	-	-	-	-	-
06	7500	-	-	-	-	-	-	-	-	-	-	-	-	-	-	-	-	-	-
07	7500	-	-	-	-	-	-	-	-	-	-	-	-	-	-	-	-	-	-
08	7500	-	-	-	-	-	-	-	-	-	-	-	-	-	-	-	-	-	-
09	7500	-	-	-	-	-	-	-	-	-	-	-	-	-	-	-	-	-	-
10	7500	-	-	-	-	-	-	-	-	-	-	-	-	-	-	-	-	-	-
11	7500	-	-	-	-	-	-	-	-	-	-	-	-	-	-	-	-	-	-

Table 53. List and classification of discarded time series for Test 356. Npts = number of points in the truncated time series. O = Over-spiked, L = Lost, S = Shifted.

Test 356		gauge #																	
Station	Npts	01	02	03	04	05	06	07	08	09	10	11	12	13	14	15	16	17	18
01	7500	-	-	-	-	-	-	-	-	-	-	-	-	-	-	-	-	-	-
02	7500	-	-	-	-	-	-	-	-	-	-	-	-	-	-	-	-	-	-
03	7500	-	-	-	-	-	-	-	-	-	-	-	-	-	-	-	-	-	-
04	7500	-	-	-	-	-	-	-	-	-	-	-	-	-	-	-	-	-	-
05	7500	-	-	-	-	-	-	-	-	-	-	-	-	-	-	-	-	-	-
06	7500	-	-	-	-	-	-	-	-	-	-	-	-	-	-	-	-	-	-
07	7500	-	-	-	-	-	-	-	-	-	-	-	-	-	-	-	-	-	-
08	7500	-	-	-	-	-	-	-	-	-	-	-	-	-	-	-	-	-	-
09	7500	-	-	-	-	-	-	-	-	-	-	-	-	-	-	-	-	-	-
10	7500	-	-	-	-	-	-	-	-	-	-	-	-	-	-	-	-	-	-
11	7500	-	-	-	-	-	-	-	-	-	-	-	-	-	-	-	-	-	-

APPENDIX C

LOCATION OF ADVS

Table 54. Location of ADVs during Test 100. x, y are cross-shore and longshore distances in the fixed local coordinate system. All distances measured in meters.

Test 100		ADV #				
Station		A	B	E	D	C
01	(x, y):	(25.0, 6.7)	(25.0, 7.9)	(25.0, 9.2)	(25.0, 10.4)	(25.0, 11.5)
02	(x, y):	(23.7, 6.7)	(23.7, 7.9)	(23.7, 9.2)	(23.7, 10.4)	(23.7, 11.5)
03	(x, y):	(23.0, 6.7)	(23.0, 7.9)	(23.0, 9.2)	(23.0, 10.4)	(23.0, 11.5)
04	(x, y):	(21.7, 6.7)	(21.7, 7.9)	(21.7, 9.2)	(21.7, 10.4)	(21.7, 11.5)
05	(x, y):	(20.8, 6.7)	(20.8, 7.9)	(20.8, 9.2)	(20.8, 10.4)	(20.8, 11.5)
06	(x, y):	(20.5, 6.7)	(20.5, 7.9)	(20.5, 9.2)	(20.5, 10.4)	(20.5, 11.5)
07	(x, y):	(20.1, 6.7)	(20.1, 7.9)	(20.1, 9.2)	(20.1, 10.4)	(20.1, 11.5)
08	(x, y):	(18.6, 6.7)	(18.6, 7.9)	(18.6, 9.2)	(18.6, 10.4)	(18.6, 11.5)
09	(x, y):	(17.3, 6.7)	(17.3, 7.9)	(17.3, 9.2)	(17.3, 10.4)	(17.3, 11.5)
10	(x, y):	(16.6, 6.7)	(16.6, 7.9)	(16.6, 9.2)	(16.6, 10.4)	(16.6, 11.5)
11	(x, y):	(15.3, 6.7)	(15.3, 7.9)	(15.3, 9.2)	(15.3, 10.4)	(15.3, 11.5)

Table 55. Location of ADVs during Test 200. x, y are cross-shore and longshore distances in the fixed local coordinate system. All distances measured in meters.

Test 200		ADV #				
Station		A	B	E	D	C
01	(x, y):	(25.0, 7.9)	(25.0, 8.7)	(25.0, 9.6)	(25.0, 10.4)	(25.0, 11.5)
02	(x, y):	(23.7, 7.9)	(23.7, 8.7)	(23.7, 9.6)	(23.7, 10.4)	(23.7, 11.5)
03	(x, y):	(23.0, 7.9)	(23.0, 8.7)	(23.0, 9.6)	(23.0, 10.4)	(23.0, 11.5)
04	(x, y):	(21.7, 7.9)	(21.7, 8.7)	(21.7, 9.6)	(21.7, 10.4)	(21.7, 11.5)
05	(x, y):	(20.8, 7.9)	(20.8, 8.7)	(20.8, 9.6)	(20.8, 10.4)	(20.8, 11.5)
06	(x, y):	(20.5, 7.9)	(20.5, 8.7)	(20.5, 9.6)	(20.5, 10.4)	(20.5, 11.5)
07	(x, y):	(20.1, 7.9)	(20.1, 8.7)	(20.1, 9.6)	(20.1, 10.4)	(20.1, 11.5)
08	(x, y):	(18.6, 7.9)	(18.6, 8.7)	(18.6, 9.6)	(18.6, 10.4)	(18.6, 11.5)
09	(x, y):	(17.3, 7.9)	(17.3, 8.7)	(17.3, 9.6)	(17.3, 10.4)	(17.3, 11.5)
10	(x, y):	(16.6, 7.9)	(16.6, 8.7)	(16.6, 9.6)	(16.6, 10.4)	(16.6, 11.5)
11	(x, y):	(15.3, 7.9)	(15.3, 8.7)	(15.3, 9.6)	(15.3, 10.4)	(15.3, 11.5)

Table 56. Location of ADVs during Test 300. x, y are cross-shore and longshore distances in the fixed local coordinate system. All distances measured in meters.

Test 300		ADV #				
Station		A	B	E	D	C
01	(x, y):	(25.0, 5.5)	(25.0, 7.1)	(25.0, 8.8)	(25.0, 10.4)	(25.0, 11.5)
02	(x, y):	(23.7, 5.5)	(23.7, 7.1)	(23.7, 8.8)	(23.7, 10.4)	(23.7, 11.5)
03	(x, y):	(23.0, 5.5)	(23.0, 7.1)	(23.0, 8.8)	(23.0, 10.4)	(23.0, 11.5)
04	(x, y):	(21.7, 5.5)	(21.7, 7.1)	(21.7, 8.8)	(21.7, 10.4)	(21.7, 11.5)
05	(x, y):	(20.8, 5.5)	(20.8, 7.1)	(20.8, 8.8)	(20.8, 10.4)	(20.8, 11.5)
06	(x, y):	(20.5, 5.5)	(20.5, 7.1)	(20.5, 8.8)	(20.5, 10.4)	(20.5, 11.5)
07	(x, y):	(20.1, 5.5)	(20.1, 7.1)	(20.1, 8.8)	(20.1, 10.4)	(20.1, 11.5)
08	(x, y):	(18.6, 5.5)	(18.6, 7.1)	(18.6, 8.8)	(18.6, 10.4)	(18.6, 11.5)
09	(x, y):	(17.3, 5.5)	(17.3, 7.1)	(17.3, 8.8)	(17.3, 10.4)	(17.3, 11.5)
10	(x, y):	(16.6, 5.5)	(16.6, 7.1)	(16.6, 8.8)	(16.6, 10.4)	(16.6, 11.5)
11	(x, y):	(15.3, 5.5)	(15.3, 7.1)	(15.3, 8.8)	(15.3, 10.4)	(15.3, 11.5)

APPENDIX D

LIST OF DISCARDED ADV TIME SERIES

Table 57. List and classification of discarded time series for Test 101. Npts = number of points in the truncated time series. L = Lost, NR = Not Recorded.

Test 101		ADV #				
Station	Npts	A	B	E	D	C
01	8750	-	-	-	-	-
02	8750	-	-	-	-	-
03	8750	-	-	-	-	-
04	8750	-	-	-	-	-
05	8750	-	-	-	-	-
06	8750	-	-	-	-	-
07	8750	-	-	-	-	-
08	8750	-	-	-	-	-
09	8750	-	-	-	-	-
10	8750	-	-	-	-	-
11	8750	-	-	-	-	-

Table 58. List and classification of discarded time series for Test 102. Npts = number of points in the truncated time series. L = Lost, NR = Not Recorded.

Test 102		ADV #				
Station	Npts	A	B	E	D	C
01	7500	-	-	-	-	-
02	7500	-	-	-	-	-
03	7500	-	-	-	-	-
04	7500	-	-	-	-	-
05	7500	-	-	-	-	-
06	7500	-	-	-	-	-
07	7500	-	-	-	-	-
08	7500	-	-	-	-	-
09	7500	-	-	-	-	-
10	7500	-	-	-	-	-
11	7500	-	-	-	-	-

Table 59. List and classification of discarded time series for Test 103. Npts = number of points in the truncated time series. L = Lost, NR = Not Recorded.

Test 103		ADV #				
Station	Npts	A	B	E	D	C
01	7500	-	-	-	-	-
02	7500	-	-	-	-	-
03	7500	-	-	-	-	-
04	7500	-	-	-	-	-
05	7500	-	-	-	-	-
06	7500	-	-	-	-	-
07	7500	-	-	-	-	-
08	7500	-	-	-	-	-
09	7500	-	-	-	-	-
10	7500	-	-	-	-	-
11	7500	-	-	-	-	-

Table 60. List and classification of discarded time series for Test 104. Npts = number of points in the truncated time series. L = Lost, NR = Not Recorded.

Test 104		ADV #				
Station	Npts	A	B	E	D	C
01	8750	-	-	-	-	-
02	8750	-	-	-	-	-
03	8750	-	-	-	-	-
04	8750	-	-	-	-	-
05	8750	-	-	-	-	-
06	8750	-	-	-	-	-
07	8750	-	-	-	-	-
08	8750	-	-	-	-	-
09	8750	-	-	-	-	-
10	8750	-	-	-	-	-
11	8750	-	-	-	-	-

Table 61. List and classification of discarded time series for Test 105. Npts = number of points in the truncated time series. L = Lost, NR = Not Recorded.

Test 105		ADV #				
Station	Npts	A	B	E	D	C
01	7500	-	-	-	-	-
02	7500	-	-	-	-	-
03	7500	-	-	-	-	-
04	7500	-	-	-	-	-
05	7500	-	-	-	-	-
06	7500	-	-	-	-	-
07	7500	-	-	-	-	-
08	7500	-	-	-	-	-
09	7500	-	-	-	-	-
10	7500	-	-	-	-	-
11	7500	-	-	-	-	-

Table 62. List and classification of discarded time series for Test 106. Npts = number of points in the truncated time series. L = Lost, NR = Not Recorded.

Test 106		ADV #				
Station	Npts	A	B	E	D	C
01	7500	-	-	-	-	-
02	7500	-	-	-	-	-
03	7500	-	-	-	-	-
04	7500	-	-	-	-	-
05	7500	-	-	-	-	-
06	7500	-	-	-	-	-
07	7500	-	-	-	-	-
08	7500	-	-	-	-	-
09	7500	-	-	-	-	-
10	7500	-	-	-	-	-
11	7500	-	-	-	-	-

Table 63. List and classification of discarded time series for Test 151. Npts = number of points in the truncated time series. L = Lost, NR = Not Recorded.

Test 151		ADV #				
Station	Npts	A	B	E	D	C
01	7500	-	-	-	-	-
02	7500	-	-	-	-	-
03	7500	-	-	-	-	-
04	7500	-	-	-	-	-
05	7500	-	-	-	-	-
06	7500	-	-	-	-	-
07	7500	-	-	-	-	-
08	7500	-	-	-	-	-
09	7500	-	-	-	-	-
10	7500	-	-	-	-	-
11	7500	-	-	-	-	-

Table 64. List and classification of discarded time series for Test 152. Npts = number of points in the truncated time series. L = Lost, NR = Not Recorded.

Test 152		ADV #				
Station	Npts	A	B	E	D	C
01	7500	-	-	L	-	-
02	7500	-	-	-	-	-
03	7500	-	-	-	-	-
04	7500	-	-	-	-	-
05	7500	-	-	-	-	-
06	7500	-	-	-	-	-
07	7500	-	-	-	-	-
08	7500	L	L	-	L	L
09	7500	-	-	-	-	-
10	7500	-	-	-	-	-
11	7500	-	-	-	-	-

Table 65. List and classification of discarded time series for Test 153. Npts = number of points in the truncated time series. L = Lost, NR = Not Recorded.

Test 153		ADV #				
Station	Npts	A	B	E	D	C
01	8250	-	-	-	-	-
02	8250	-	-	-	-	-
03	8250	-	-	-	-	-
04	8250	-	-	-	-	-
05	8250	-	-	-	-	-
06	8250	-	-	-	-	-
07	8250	-	-	-	-	-
08	8250	-	-	-	-	-
09	8250	-	-	-	-	-
10	8250	-	-	-	-	-
11	8250	-	-	-	-	-

Table 66. List and classification of discarded time series for Test 154. Npts = number of points in the truncated time series. L = Lost, NR = Not Recorded.

Test 154		ADV #				
Station	Npts	A	B	E	D	C
01	7500	-	-	-	-	-
02	7500	-	-	-	-	-
03	7500	-	-	-	-	-
04	7500	-	-	-	-	-
05	7500	-	-	-	-	-
06	7500	-	-	-	-	-
07	7500	-	-	-	-	-
08	7500	-	-	-	-	-
09	7500	-	-	-	-	-
10	7500	-	-	-	-	-
11	7500	-	-	-	-	-

Table 67. List and classification of discarded time series for Test 155. Npts = number of points in the truncated time series. L = Lost, NR = Not Recorded.

Test 155		ADV #				
Station	Npts	A	B	E	D	C
01	7500	-	-	-	-	-
02	7500	-	-	-	-	-
03	7500	-	-	-	-	-
04	7500	-	-	-	-	-
05	7500	-	-	-	-	-
06	7500	-	-	-	-	-
07	7500	-	-	-	-	-
08	7500	-	-	-	-	-
09	7500	-	-	-	-	-
10	7500	-	-	-	-	-
11	7500	-	-	-	-	-

Table 68. List and classification of discarded time series for Test 156. Npts = number of points in the truncated time series. L = Lost, NR = Not Recorded.

Test 156		ADV #				
Station	Npts	A	B	E	D	C
01	7500	-	-	-	-	-
02	7500	-	-	-	-	-
03	7500	-	-	-	-	-
04	7500	-	-	-	-	-
05	7500	-	-	-	-	-
06	7500	-	-	-	-	-
07	7500	-	-	-	-	-
08	7500	-	-	-	-	-
09	7500	-	-	-	-	-
10	7500	-	-	-	-	-
11	7500	-	-	-	-	-

Table 69. List and classification of discarded time series for Test 203. Npts = number of points in the truncated time series. L = Lost, NR = Not Recorded.

Test 203		ADV #				
Station	Npts	A	B	E	D	C
01	7500	-	-	-	-	-
02	7500	-	-	-	-	-
03	7500	-	-	-	-	-
04	7500	-	-	-	-	-
05	7500	-	-	-	-	-
06	7500	-	-	-	-	-
07	7500	-	-	-	-	-
08	7500	-	-	-	-	-
09	7500	-	-	-	-	-
10	7500	-	-	-	-	-
11	7500	-	-	-	-	-

Table 70. List and classification of discarded time series for Test 204. Npts = number of points in the truncated time series. L = Lost, NR = Not Recorded.

Test 204		ADV #				
Station	Npts	A	B	E	D	C
01	7500	-	-	-	-	-
02	7500	-	-	-	-	-
03	7500	-	-	-	-	-
04	7500	-	-	-	-	-
05	7500	-	-	-	-	-
06	7500	-	-	-	-	-
07	7500	-	-	-	-	-
08	7500	-	-	-	-	-
09	7500	-	-	-	-	-
10	7500	-	-	-	-	-
11	7500	-	-	-	-	-

Table 71. List and classification of discarded time series for Test 205. Npts = number of points in the truncated time series. L = Lost, NR = Not Recorded.

Test 205		ADV #				
Station	Npts	A	B	E	D	C
01	7500	-	-	L	-	-
02	7500	-	-	-	-	-
03	7500	-	-	-	-	-
04	7500	-	-	-	-	-
05	7500	-	-	-	-	-
06	7500	-	-	-	-	-
07	7500	-	-	-	-	-
08	7500	-	-	-	-	-
09	7500	-	-	-	-	-
10	7500	-	-	-	-	-
11	7500	-	-	-	-	-

Table 72. List and classification of discarded time series for Test 206. Npts = number of points in the truncated time series. L = Lost, NR = Not Recorded.

Test 206		ADV #				
Station	Npts	A	B	E	D	C
01	7250	-	-	-	-	-
02	7250	-	-	-	-	-
03	7250	-	-	-	-	-
04	7250	-	-	-	-	-
05	7250	-	-	-	-	-
06	7250	-	-	-	-	-
07	7250	-	-	-	-	-
08	7250	-	-	-	-	-
09	7250	-	-	-	-	-
10	7250	-	-	-	-	-
11	7250	-	-	-	-	-

Table 73. List and classification of discarded time series for Test 253. Npts = number of points in the truncated time series. L = Lost, NR = Not Recorded.

Test 253		ADV #				
Station	Npts	A	B	E	D	C
01	7500	-	-	-	-	-
02	7500	-	-	-	-	-
03	7500	-	-	-	-	-
04	7500	-	-	-	-	-
05	7500	-	-	-	-	-
06	7500	-	-	-	-	-
07	7500	-	-	-	-	-
08	7500	-	-	-	-	-
09	7500	-	-	-	-	-
10	7500	-	-	-	-	-
11	7500	L	L	-	L	L

Table 74. List and classification of discarded time series for Test 254. Npts = number of points in the truncated time series. L = Lost, NR = Not Recorded.

Test 254		ADV #				
Station	Npts	A	B	E	D	C
01	7500	-	-	-	-	-
02	7500	-	-	-	-	-
03	7500	-	-	-	-	-
04	7500	-	-	-	-	-
05	7500	-	-	-	-	-
06	7500	-	-	-	-	-
07	7500	-	-	-	-	-
08	7500	-	-	-	-	-
09	7500	-	-	-	-	-
10	7500	-	-	-	-	-
11	7500	-	-	-	-	-

Table 75. List and classification of discarded time series for Test 255. Npts = number of points in the truncated time series. L = Lost, NR = Not Recorded.

Test 255		ADV #				
Station	Npts	A	B	E	D	C
01	7500	-	-	-	-	-
02	7500	L	L	-	L	L
03	7500	-	-	-	-	-
04	7500	-	-	-	-	-
05	7500	-	-	-	-	-
06	7500	-	-	-	-	-
07	7500	-	-	-	-	-
08	7500	-	-	-	-	-
09	7500	-	-	-	-	-
10	7500	-	-	-	-	-
11	7500	-	-	-	-	-

Table 76. List and classification of discarded time series for Test 256. Npts = number of points in the truncated time series. L = Lost, NR = Not Recorded.

Test 256		ADV #				
Station	Npts	A	B	E	D	C
01	7500	-	-	-	-	-
02	7500	-	-	-	-	-
03	7500	-	-	-	-	-
04	7500	-	-	-	-	-
05	7500	-	-	-	-	-
06	7500	-	-	-	-	-
07	7500	-	-	-	-	-
08	7500	-	-	-	-	-
09	7500	-	-	-	-	-
10	7500	-	-	-	-	-
11	7500	-	-	-	-	-

Table 77. List and classification of discarded time series for Test 303. Npts = number of points in the truncated time series. L = Lost, NR = Not Recorded.

Test 303		ADV #				
Station	Npts	A	B	E	D	C
01	7500	-	-	-	-	-
02	7500	-	-	-	-	-
03	7500	-	-	-	-	-
04	7500	-	-	-	-	-
05	7500	-	-	-	-	-
06	7500	L	L	-	L	L
07	7500	-	-	-	-	-
08	7500	-	-	-	-	-
09	7500	-	-	-	-	-
10	7500	L	L	-	L	L
11	7500	-	-	-	-	-

Table 78. List and classification of discarded time series for Test 304. Npts = number of points in the truncated time series. L = Lost, NR = Not Recorded.

Test 304		ADV #				
Station	Npts	A	B	E	D	C
01	7500	-	-	-	-	-
02	7500	-	-	-	-	-
03	7500	-	-	-	-	-
04	7500	-	-	-	-	-
05	7500	-	-	-	-	-
06	7500	L	L	-	L	L
07	7500	-	-	-	-	-
08	7500	-	-	-	-	-
09	7500	-	-	-	-	-
10	7500	-	-	-	-	-
11	7500	-	-	-	-	-

Table 79. List and classification of discarded time series for Test 305. Npts = number of points in the truncated time series. L = Lost, NR = Not Recorded.

Test 305		ADV #				
Station	Npts	A	B	E	D	C
01	7500	-	-	-	-	-
02	7500	-	-	-	-	-
03	7500	L	L	-	L	L
04	7500	-	-	-	-	-
05	7500	-	-	-	-	-
06	7500	-	-	-	-	-
07	7500	-	-	-	-	-
08	7500	-	-	-	-	-
09	7500	-	-	-	-	-
10	7500	-	-	-	-	-
11	7500	-	-	-	-	-

Table 80. List and classification of discarded time series for Test 306. Npts = number of points in the truncated time series. L = Lost, NR = Not Recorded.

Test 306		ADV #				
Station	Npts	A	B	E	D	C
01	7500	-	-	-	-	-
02	7500	-	-	-	-	-
03	7500	-	-	-	-	-
04	7500	-	-	-	-	-
05	7500	-	-	-	-	-
06	7500	-	-	-	-	-
07	7500	-	-	-	-	-
08	7500	-	-	-	-	-
09	7500	-	-	-	-	-
10	7500	-	-	-	-	-
11	7500	-	-	-	-	-

Table 81. List and classification of discarded time series for Test 353. Npts = number of points in the truncated time series. L = Lost, NR = Not Recorded.

Test 353		ADV #				
Station	Npts	A	B	E	D	C
01	7500	-	-	-	-	-
02	7500	-	-	-	-	-
03	7500	L	L	-	L	L
04	7500	-	-	-	-	-
05	7500	-	-	-	-	-
06	7500	L	L	-	L	L
07	7500	-	-	-	-	-
08	7500	-	-	-	-	-
09	7500	-	-	-	-	-
10	7500	-	-	-	-	-
11	7500	-	-	NR	-	-

Table 82. List and classification of discarded time series for Test 354. Npts = number of points in the truncated time series. L = Lost, NR = Not Recorded.

Test 354		ADV #				
Station	Npts	A	B	E	D	C
01	7500	-	-	-	-	-
02	7500	-	-	-	-	-
03	7500	L	L	-	L	L
04	7500	-	-	-	-	-
05	7500	-	-	-	-	-
06	7500	-	-	-	-	-
07	7500	-	-	-	-	-
08	7500	-	-	-	-	-
09	7500	-	-	-	-	-
10	7500	L	L	-	L	L
11	7500	-	-	NR	-	-

Table 83. List and classification of discarded time series for Test 355. Npts = number of points in the truncated time series. L = Lost, NR = Not Recorded.

Test 355		ADV #				
Station	Npts	A	B	E	D	C
01	7500	-	-	NR	-	-
02	7500	-	-	NR	-	-
03	7500	-	-	NR	-	-
04	7500	-	-	NR	-	-
05	7500	-	-	NR	-	-
06	7500	-	-	NR	-	-
07	7500	-	-	NR	-	-
08	7500	-	-	NR	-	-
09	7500	-	-	NR	-	-
10	7500	-	-	NR	-	-
11	7500	-	-	NR	-	-

Table 84. List and classification of discarded time series for Test 356. Npts = number of points in the truncated time series. L = Lost, NR = Not Recorded.

Test 356		ADV #				
Station	Npts	A	B	E	D	C
01	7500	-	-	NR	-	-
02	7500	-	-	NR	-	-
03	7500	-	-	NR	-	-
04	7500	-	-	NR	-	-
05	7500	-	-	NR	-	-
06	7500	-	-	NR	-	-
07	7500	-	-	NR	-	-
08	7500	-	-	NR	-	-
09	7500	-	-	NR	-	-
10	7500	-	-	NR	-	-
11	7500	-	-	NR	-	-

APPENDIX E

SUMMARY OF STATIONS LAYOUT

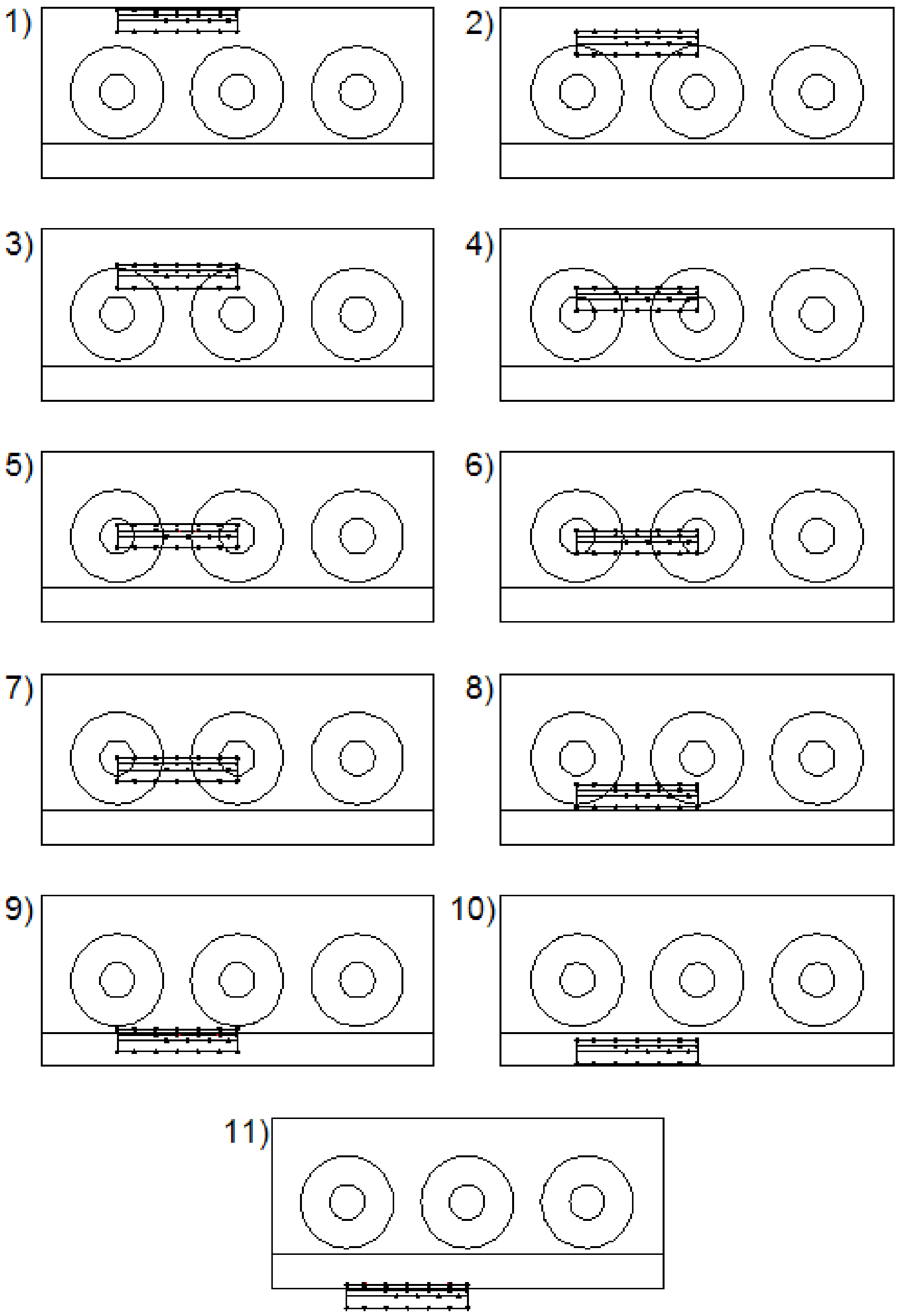

Fig. 87. Layout of the different bridge positions from station 1 to 11 for a 5.00 m spacing between the vegetation fields.

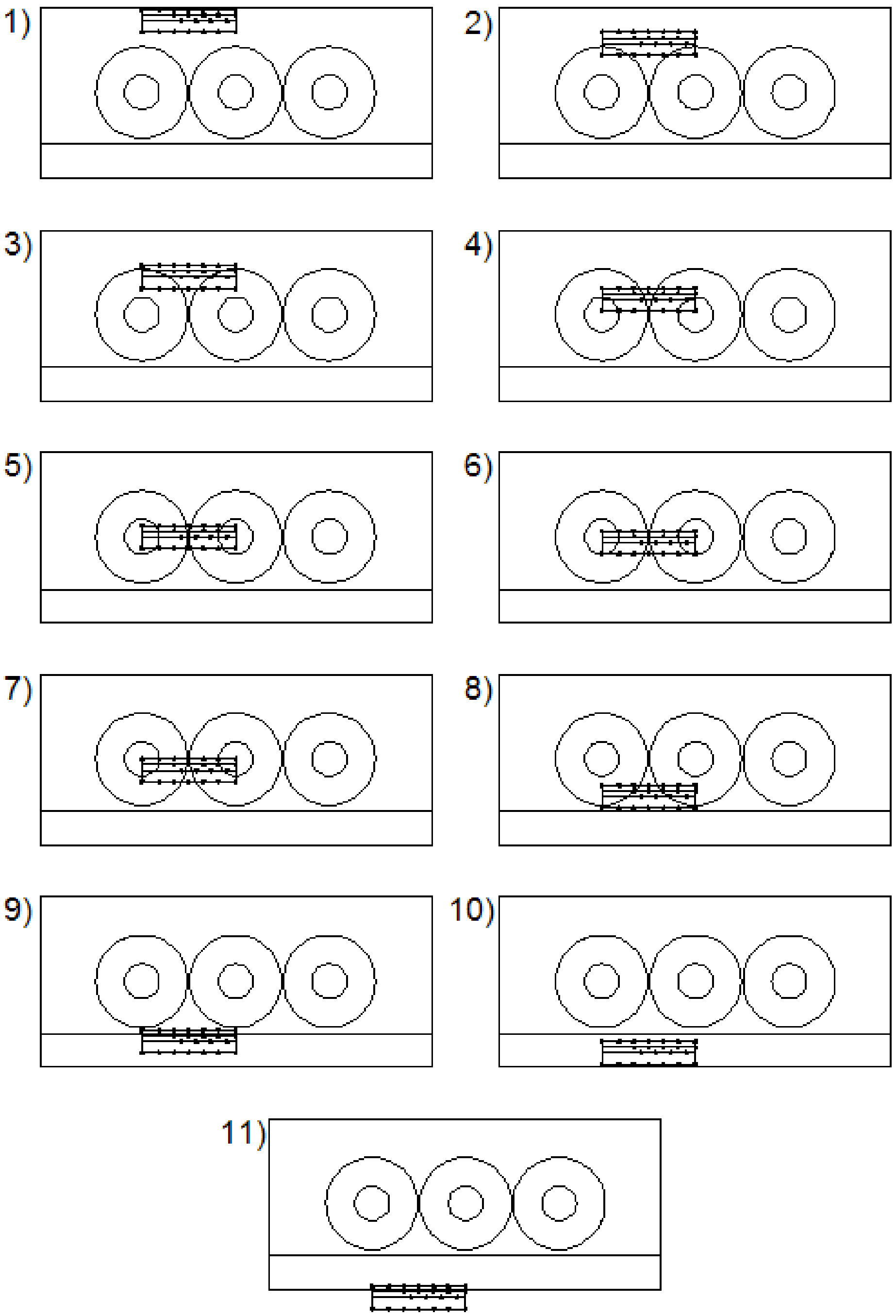

Fig. 88. Layout of the different bridge positions from station 1 to 11 for a 3.46 m spacing between the vegetation fields.

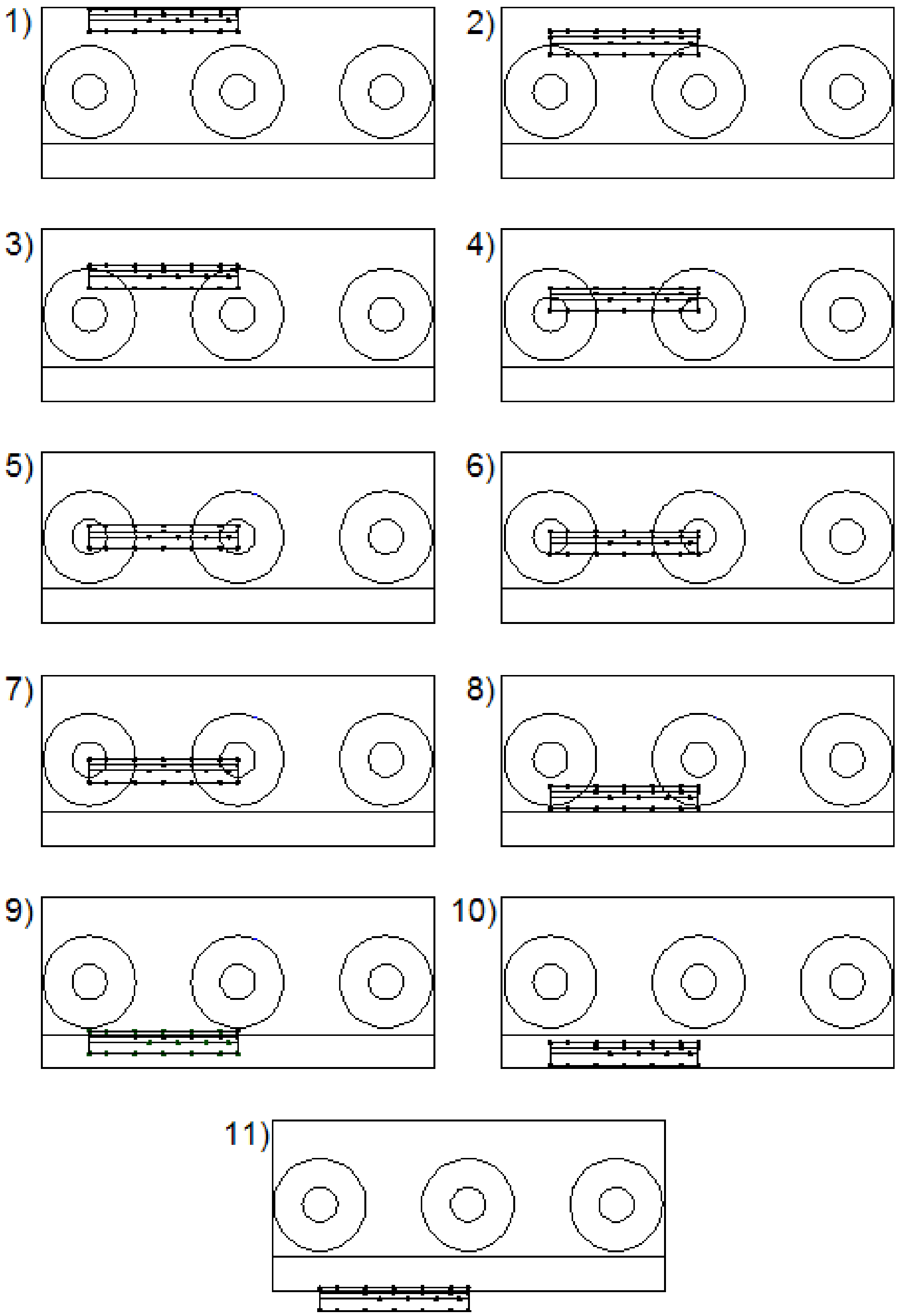

Fig. 89. Layout of the different bridge positions from station 1 to 11 for a 6.64 m spacing between the vegetation fields.

VITA

Name: Melanie Khanh Phuong TRUONG

Email Address: mel.kp.truong@gmail.com

Education: B.S. in Physics and Engineering Sciences
Lycee Chaptal, Paris, FRANCE (2007)
M.S., Civil Engineering
Ecole Speciale des Travaux Publics, Paris, FRANCE (2011)
M.S., Ocean Engineering
Texas A&M University, College Station, TX, USA (2011)

Mailing Address: Dr. Scott A. Socolofsky
Coastal and Ocean Engineering Division
Department of Civil Engineering
Texas A&M University
3136 TAMU
College Station, TX 77843-3136